International Journal of
Molecular Sciences

MDPI

Review

Radiopharmaceuticals for PET and SPECT Imaging: A Literature Review over the Last Decade

George Crișan [1,2], Nastasia Sanda Moldovean-Cioroianu [1], Diana-Gabriela Timaru [1], Gabriel Andrieș [2], Călin Căinap [3] and Vasile Chiș [1,4,*]

1 Faculty of Physics, Babeş-Bolyai University, Str. M. Kogălniceanu 1, 400084 Cluj-Napoca, Romania; george.crsn@gmail.com (G.C.); sanda.moldovean@ubbcluj.ro (N.S.M.-C.); diana.timaru@stud.ubbcluj.ro (D.-G.T.)
2 Department of Nuclear Medicine, County Clinical Hospital, Clinicilor 3-5, 400006 Cluj-Napoca, Romania; gabriel.andries@umfcluj.ro
3 The Oncology Institute "Prof. Dr. Ion Chiricuță", Republicii 34-36, 400015 Cluj-Napoca, Romania; calincainap@yahoo.co.uk
4 Institute for Research, Development and Innovation in Applied Natural Sciences, Babeș-Bolyai University, Str. Fântânele 30, 400327 Cluj-Napoca, Romania
* Correspondence: vasile.chis@ubbcluj.ro

Abstract: Positron emission tomography (PET) uses radioactive tracers and enables the functional imaging of several metabolic processes, blood flow measurements, regional chemical composition, and/or chemical absorption. Depending on the targeted processes within the living organism, different tracers are used for various medical conditions, such as cancer, particular brain pathologies, cardiac events, and bone lesions, where the most commonly used tracers are radiolabeled with 18F (e.g., [^{18}F]-FDG and NA [^{18}F]). Oxygen-15 isotope is mostly involved in blood flow measurements, whereas a wide array of ^{11}C-based compounds have also been developed for neuronal disorders according to the affected neuroreceptors, prostate cancer, and lung carcinomas. In contrast, the single-photon emission computed tomography (SPECT) technique uses gamma-emitting radioisotopes and can be used to diagnose strokes, seizures, bone illnesses, and infections by gauging the blood flow and radio distribution within tissues and organs. The radioisotopes typically used in SPECT imaging are iodine-123, technetium-99m, xenon-133, thallium-201, and indium-111. This systematic review article aims to clarify and disseminate the available scientific literature focused on PET/SPECT radiotracers and to provide an overview of the conducted research within the past decade, with an additional focus on the novel radiopharmaceuticals developed for medical imaging.

Keywords: PET; SPECT; radiopharmaceuticals; tracers; molecular imaging; review

check for updates

Citation: Crișan, G.; Moldovean-Cioroianu, N.S.; Timaru, D.-G.; Andrieș, G.; Căinap, C.; Chiș, V. Radiopharmaceuticals for PET and SPECT Imaging: A Literature Review over the Last Decade. *Int. J. Mol. Sci.* **2022**, *23*, 5023. https://doi.org/10.3390/ijms23095023

Academic Editor: Giorgio Treglia

Received: 3 April 2022
Accepted: 28 April 2022
Published: 30 April 2022

Publisher's Note: MDPI stays neutral with regard to jurisdictional claims in published maps and institutional affiliations.

Copyright: © 2022 by the authors. Licensee MDPI, Basel, Switzerland. This article is an open access article distributed under the terms and conditions of the Creative Commons Attribution (CC BY) license (https://creativecommons.org/licenses/by/4.0/).

1. Introduction

Over the last decade, the initial focus on medical imaging based on detection and diagnosis has reoriented towards prognosis, tissue characterization, and prediction of treatment efficacy. To this extent, functional imaging, such as positron emission tomography (PET) and single-photon emission computed tomography (SPECT), has become essential in the clinical decision-making process in various fields of medicine. Moreover, hybrid imaging, combining SPECT and PET with computed tomography (CT) or magnetic resonance imaging (MRI), has increased the diagnostic accuracy of both PET and SPECT by the benefit of the morphological information obtained by the CT and MRI scans and the implementation of attenuation correction. PET represents a quantitative imaging tool that appears to surpass the SPECT technique. However, the answer to the highly debated question of which modality will monopolize the nuclear imaging technologies remains unsettled. Traditionally, when compared with SPECT, PET technology provides better image resolution, less attenuation (due to higher photon energy) and scatter artifacts, and,

MIM Software Inc. v. Progenics Pharmaceuticals, Inc.
IPR2025-00630
Progenics EX2017

consequently, superior diagnostic capabilities. Two of the most important advantages of PET over the SPECT modality are represented by PET's higher sensitivity and more robust and flexible tracers, making PET a versatile and powerful tool for clinical and research applications. These advantages, however, come with a high cost burden that limits the availability of PET imaging. Most positron-emitting radioisotopes have short half-lives and require in-house cyclotron production. Therein lies the main advantage of SPECT. Radiopharmaceuticals used for SPECT imaging are cheaper and easy to distribute, and in particular conditions, they present more specific targeting abilities of the biologically active molecules due to the longer half-life of single-photon emitters, allowing for an accurate description of the biological processes at equilibrium in vivo (within several hours, or even days, after the radiolabeled compound's administration). It is worth noting that the development of the radiopharmaceutical compounds related to distinctive diagnostic and therapeutic targets [1], and therefore used in both imaging modalities, goes hand in hand with the acquisition systems' development [2].

Figure 1 shows the number of scientific publications over the last 10 years related to radiotracers for PET/CT and SPECT/CT techniques. A clearly increasing trend of publications is observed for both cases, yet with a number of SPECT papers, on average, about seven times smaller.

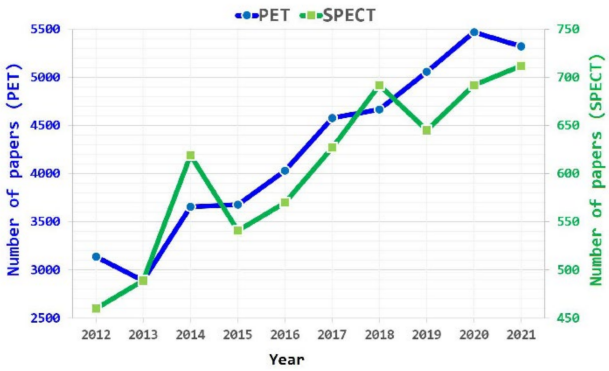

Figure 1. Number of scientific papers related to PET (left axis) and SPECT (right axis) radiopharmaceuticals over the past 10 years.

PET represents the functional imaging technique widely used nowadays for clinical diagnosis of a large variety of diseases, and employs short half-life positron-emitting isotopes, such as carbon-11 (^{11}C; t 1/2 = 20.4 min) and fluorine-18 (^{18}F; t 1/2 = 109.7 min), for in vivo measurement of biological processes. The technique is also heavily used as a research tool in preclinical studies using animals and for the detection of specific molecules within the human body. In the 1960s, radiopharmaceuticals were already attributed as drugs designed for in vivo diagnosis and treatment applications. A radiopharmaceutical compound consists of: (1) a molecular structure identified as a vehicle molecule and (2) a positron-emitting radionuclide. The radioisotope is attached to the vehicle molecule, also known as ligand, and then injected into the body as a radioactive tracer [3].

Commonly, the vehicle molecules are responsible for the chemical and biochemical reactions within the body; therefore, the connections between vehicle structures and radionuclides are stabilized using chemical linkers. The ligands must present high selectivity and specificity towards their targets. These target sites can be either transporters, enzymes, selected receptors, or antigens. Moreover, the targets can be part of metabolic alterations, tissue hypo-oxygenation, or changes in gene and/or protein expression. However, in pathological conditions, the target's function might be significantly altered, further affecting the biological interactions between the vehicle part and its target, particularly in tumors, where the receptors, transporters, and enzymes' expression pathways are heavily affected [3,4].

The PET technique is based on the detection of emitted radioactivity levels of the tracer, normally administrated through an intravenous injection. The radiation doses are compa-

MIM Software Inc. v. Progenics Pharmaceuticals, Inc.
IPR2025-00630
Progenics EX2017

rable to those used in computed tomography (CT) scans [3]. The measurement of glucose consumption rates within different parts of the body is the most common use of PET imaging based on the accumulation of the radiolabeled glucose analogue 18-fluorodeoxyglucose (FDG). Considering that glucose metabolizes at faster rates in malignant tumors when compared with benign ones, this technique is widely used for whole-body scans in order to stage the cancer [4]. Further applications of PET scans include blood flow and oxygen consumption in the brain; tracking of specific neurotransmitters, such as dopamine in Parkinson's disease; or, in cardiology, evaluation of myocardial viability [3].

A PET radionuclide selection should be considered based on several crucial aspects regarding, first of all, the radionuclide availability, then its physical characteristics, and its radiochemical and radiopharmacological issues [3,4]. With respect to radiochemical considerations, since their primary chemical form is not predisposed to direct labeling reactions, an initial activation step is required for reactive chemical modifications.

A wide array of PET radiopharmaceuticals have been tested and evaluated in clinical trials, targeting a large spectrum of diseases. While all these PET compounds present different compositions in terms of their vehicle molecules (or ligands), they all must follow the same requirements—as imaging agents—with high specificity, high binding affinity, low toxicity, stability (e.g., against different enzymes in plasma), rapid clearance from nontargeted tissue, accessibility at low costs, and permission for clinical usage [4]. The selection or development of a radiopharmaceutical has to meet certain criteria in order to be adequate for an exact biological targeting or disease. Specifically, the radionuclide must have a reasonable half-life, depending on the desired use. In addition, characteristics such as size or charge of the molecule, its specific activity, lipophilicity, stability, and the metabolism of the radiolabeled compounds are directly correlated to the specificity of each biological target. Thus, through quality control tests, aspects concerning the physicochemical, radiochemical, or biological properties are also required [5].

As previously mentioned, alongside the half-life of the radionuclide, the size and mass also play an important role in eliminating the radiopharmaceutical out of the in vivo system. The size of the molecule ensures a better clearance from circulation and has an impact over the in vivo distribution patterns of the radiopharmaceutical. For instance, larger molecules have longer localization time when compared with small molecules, and they cannot be filtered by the kidneys [6]. Additionally, the charges also influence their solubility in different solvents. Noncharged molecules are prone to be more soluble in lipids and organic solvents, whereas radiopharmaceuticals with greater charges present better solubility in aqueous solution.

The radiolabeled compound preparation should be considered in an aqueous solution with a pH as close as possible to the pH of blood. In addition, the ionic strength and osmolality should also be compatible with blood. Their solubility is influenced by their sizes, masses, charges, shapes, and a fundamental physicochemical property, their lipophilicity. Last but not least, lipophilicity has a significant impact on the absorption, distribution, and elimination of drug molecules. For example, neutral lipophilic molecules are usually the only ones able to penetrate the blood–brain barrier (BBB) [7].

Almost all drugs are able, to a certain extent, to bind to blood components. Protein binding depends on the nature of the protein, the concentration of the anions, the charge of the radiopharmaceutical compound, and the pH. Increased lipophilicity encourages nonspecific binding to albumin and other plasma proteins [8]. Metals have a high affinity for proteins, and that leads to a high possibility of ion exchange between a metal complex and a protein. Therefore, the protein binding properties should also be thoroughly studied before clinical use.

In terms of stability, the physicochemical parameters, such as temperature, pH, and light, must be carefully established for the radiopharmaceutical preparation and storage. With regard to the compound's metabolism, if the radiopharmaceutical compound can be metabolically decomposed, its biodistribution becomes affected because of the mixture of the intact agents and metabolic fragments from the decomposed radiolabeled molecule.

MIM Software Inc. v. Progenics Pharmaceuticals, Inc.
IPR2025-00630
Progenics EX2017

The blood metabolism might also alter the delivery of the radiopharmaceutical to the target site. Moreover, the metabolic compounds might get stuck at the target site, and therefore, the relative concentration of the intact radiolabeled molecules, as well as the relative concentration of the metabolic products, must be carefully measured in order to obtain meaningful results [5].

Finally, depending on the concentration of target molecules, a radiopharmaceutical compound must exhibit a proper specific activity (SA). SA is a measure of the number of radioactive probe molecules that are bound to the targeted system. Possible ways of increasing the SA include the purification of the radiopharmaceutical after radiolabeling or the reduction of the quantity of precursor for radiolabeling [5].

On the other hand, SPECT and planar scintigraphy account for almost 80% of all nuclear medicine scans performed worldwide [9]. SPECT radiopharmaceuticals have similar design considerations as described for PET but are based on gamma-emitting radioisotopes, such as ^{99m}Tc, ^{123}I, ^{131}I, ^{111}In, ^{67}Ga, ^{201}Tl, ^{81m}Kr, ^{133}Xe. While PET has the advantage of higher resolution and sensitivity, SPECT is more accessible and cheaper. PET/CT hybrid imaging accounted for the main limitation of PET, namely, uptake localization. With the adoption of PET/CT imaging in clinical practice, focus has shifted to developing novel PET radiopharmaceuticals. However, as mentioned in recent reviews [9,10], SPECT still plays an important role in nuclear medicine imaging. A wide variety of radiopharmaceuticals are available for SPECT imaging techniques that are integrated into the clinical decision-making process, such as [^{99m}Tc]-sestamibi and [^{99m}Tc]-tetrofosmin for the diagnosis of cardiac ischemia or [^{99m}Tc]-labeled diphosphonates for identifying bone metastasis in breast or prostate cancer.

In recent years, developments in SPECT imaging systems based on new solid-state cadmium telluride and zinc telluride (CZT) crystals and collimator design led to an increase in resolution and sensitivity. Furthermore, advances in radiometal-based radiopharmaceuticals for PET, specifically the successful development of [^{68}Ga]-PSMA-11, can be translated to SPECT radiometals, such as technetium [10]. These considerations have rekindled interest in designing novel SPECT radiopharmaceuticals.

As with all medical applications that use ionizing radiation, the benefit of PET and SPECT procedures must be evaluated considering the risks to patient. Dose optimization takes into consideration the administration of the amount of radioactivity that provides images of sufficient quality so as to achieve the relevant clinical information while maintaining the lowest possible radiation dose to the patient. There are different aspects that must be taken into account when deciding the administered dose, such as individual patient physiology and anatomy or the design of the imaging equipment used for the procedure [11]. Average effective doses for nuclear medicine procedures range from 0.3 to 20 mSv with SPECT having generally lower effective doses than PET mainly due to the physical characteristics of the radioisotopes used. For example, the average effective dose for a [^{99m}Tc(I)]-sestamibi cardiac rest–stress test (2-day protocol) with an administered activity of 1500 MBq is 12.8 mSv, while for a cardiac [^{18}F]-FDG PET scan with an administered activity of 740 MBq, the average effective dose is 14.1 mSv [12]. Hybrid systems increase the radiation exposure by the addition of a CT scan. The additional radiation dose depends on whether the CT scan is used for attenuation correction, localization, or diagnostic acquisitions [13].

The present review paper provides an overview of current and novel PET/SPECT radiopharmaceuticals used in the past 10 years for medical and preclinical applications. The article comprises PET and SPECT radiotracers used in clinical/preclinical oncology for central nervous system imaging, cardiovascular events, bacteria imaging, inflammation and infections, and nonspecific interactions. Imaging using PET/SPECT agents for other diseases were also considered.

MIM Software Inc. v. Progenics Pharmaceuticals, Inc.
IPR2025-00630
Progenics EX2017

2. Results

2.1. PET Radiopharmaceuticals

2.1.1. PET Radiopharmaceuticals in Oncology

[^{18}F]-Labeled Compounds

Since ^{18}F is more stable as a radioisotope, its labeling has been the most widely used option in the manufacture of PET radiopharmaceuticals. Nevertheless, due to the higher electronegativity of the F atom (4.0) compared with the H atom (2.1), ^{18}F labeling exhibits a great impact on the vehicle molecule physicochemical properties. Moreover, the C-F bonds are more stable (in vivo) and stronger than the C–H bonds. Therefore, the inclusion of F in the biological molecule structures implies an extension of their half-lives within the organism, affecting the molecules' metabolization, biodistribution, and protein-binding kinetics [4].

The gold standard PET radiopharmaceutical, the [^{18}F]-fluorodeoxyglucose ([^{18}F]-FDG) compound, is being taken up by the cancerous cells relying on the enhanced metabolic and glycolytic rates within the intracellular matrix [14]. However, in 2015, a meta-analysis study conducted by Deng et al. concluded that ^{18}F-FDG uptake in cancer patients shows just a moderate correlation to cancerous cell proliferation [15], as its uptake has also been observed in other infectious and/or inflammatory diseases. The "molecule of the 20th century" was conceptualized in the early 1970s, synthesized in 1978, and initially applied in neuroimaging [4].

As a short overview, with [^{18}F]-radionuclide's half-life of 109.7 min, ^{18}F-labeled PET compounds (Table S1) are used in prostate cancer, breast and gynecologic cancers, lung cancers, glioblastoma, hepatocellular carcinoma (HCC), solid malignancies, head and neck cancers, colorectal and pancreatic cancers, and abnormal mass tissues known as neoplasms [4].

Radiolabeled amino acid (AA) PET radiopharmaceuticals are based on endogenous molecules (originate within the body), and are widely used in oncology imaging [16], particularly in glioma imaging due to a lower background uptake (in the brain) when compared with ^{18}F-FDG [17].

Examples of ^{18}F-labeled AAs include L-6-[^{18}F]-fluoro-3,4-dihydroxyphenylalanine ([^{18}F]-FDOPA), 2-[^{18}F]-fluoroethyl-tyrosine ([^{18}F]-FET), 4-fluoroglutamine ([^{18}F]-FGln), (4*S*)-4-(3-[^{18}F]-fluoropropyl)-L-glutamic acid ([^{18}F]-FSPG), trans-1-amino-3-18F-fluorocyclobutanecarboxylic acid ([^{18}F]-FACPC), and anti-1-amino-3-[^{18}F]-fluorocyclobutane-1-carboxylic acid ([^{18}F]-FACBC). Liu et al. reported several ^{18}F-labeled AAs developed by replacing the carboxylate group (–COO−) with a radiolabeled isosteric trifluoroborate (BF3−) group [18]. Moreover, Britton and coworkers endorsed a method to produce ^{18}F-labeled AAs that can track glioblastoma and prostate adenocarcinoma xenografts (e.g., [^{18}F]-fluorothymidine ([^{18}F]-FLT)), through electrophilic radiofluorination of inactivated C–H bonds in hydrophobic amino acids [19,20]. The [^{18}F]-FLT compound enters cancer cells through specific nucleoside transporters and, once inside the cell, is being phosphorylated by thymidine kinase-1 and ultimately confined within the cell. Furthermore, it is widely used to predict chemotherapy/radiotherapy responses for patients diagnosed with lung, breast, and prostate cancers [4].

Among other standard [^{18}F]-labeled radiotracers presented in Table S1, dozens of [^{18}F]-estrogen analogue compounds have been prescribed. The [^{18}F]-fluoroestradiol ([^{18}F]-F-FES) and [^{18}F]-fluorodihydrotestosterone ([^{18}F]-FDHT) are an example of steroid derivatives able to target androgen and estrogen receptors, respectively [21].

Solid malignancies are accumulated abnormal masses of tissue that may be benign (not cancerous) or malignant (cancerous tissue). The malignant phenotypes can be correlated with sarcomas, carcinomas, and/or lymphomas. In this context, several PET radiotracers used in clinical imaging of solid malignancies were reported in the last decade, such as [^{18}F]-EF5, [^{18}F]-FMISO, [^{18}F]-FAZA, [^{18}F]-HX4, [^{18}F]-FETNIM, and [^{18}F]-FDG [22–29].

MIM Software Inc. v. Progenics Pharmaceuticals, Inc.
IPR2025-00630
Progenics EX2017

These radiopharmaceuticals are small molecules used in lung cancer and for the investigation of the hypoxic sites. The modification in hypoxia permits a better local control and post-treatment prognosis [30].

A salt vector type of tracers (e.g., [^{18}F]-NaF [31] and [^{18}F]-F-choline [32] is used for the detection of metastatic bone stages of diseases (osseous lesions), and for early detection of the biochemical recurrence in prostate cancer, where ^{18}F-choline shows elevated diagnostic accuracy, among others (e.g., [^{18}F]-fluciclovine and [^{18}F]-PSMA) [32].

The use of dynamic galactose-analogue 2-[^{18}F]-fluoro-2-deoxy-d-galactose ([^{18}F]-FDGal) PET, fused with CT scans, requires arterial blood sampling from the radial artery and enables the noninvasive in vivo measurement of metabolic function [33]. However, Horsager et al. demonstrated that metabolic liver function (with or without liver disease) can be measured using [^{18}F]-FDGal PET/CT but without arterial blood sampling. The method involved extracting an image-derived noninvasive input function from a volume of interest [34]. For the detection of extrahepatic HCC metastases, the use of ^{18}F-FDGal PET/CT was found to be significantly superior to both standard clinical PET scans with contrast-enhanced CT and [^{18}F]-FDG. Moreover, in the same study conducted by Bak-Fredslund et al., it was observed that [^{18}F]-FDGal PET/CT is able to detect (previously) unknown extrahepatic metastases in HCC patients [35].

It is well known that [^{18}F]-FDG is the most commonly used PET tracer in oncologic diseases; however, in more complex anatomical regions, [^{18}F]-FDG presents a few limitations due to its physiological uptake in normal conditions, leading to challenging image interpretation. The small sizes of the anatomical components at the head and neck region and the inflammatory processes that occur in head and neck squamous cell carcinoma (HNSCCs) patients might be a cause of misleading PET results [36], such as increased [^{18}F]-FDG uptake due to inflammatory cells' activation [37]. In contrast, Helsen et al. evaluated the diagnostic performance of FDG-PET/CT after radiotherapy treatment in patients with HNSCCs, and concluded that [^{18}F]-FDG can detect residual disease 11–12 weeks after therapy. However, they also suggest an optimal re-evaluation of 10–12 months post-treatment in order to detect possible late recurrences [38].

In 2020, a clinical trial report conducted by Schöder et al. aimed to determine the feasibility of the [^{18}F]-PARPi tracer in PET scans for patients diagnosed with head and neck cancer. [^{18}F]-PARPi was seen to be well tolerated by patients without imposing any safety concerns, and was able to detect not only the primary lesions but also the metastatic spots with a higher retention in tumor cells, when compared with healthy ones [39]. Taking into consideration that PARP proteins are overexpressed in malignant structures at the oral and oropharyngeal level, the molecular imaging of PARP is possible with only little unspecific uptake in normal tissue [40,41], and therefore, the [^{18}F]-PARPi tracer serves as a clinical tool for oropharyngeal cancer patients [42]. Moreover, it is important to note that this tracer is able to cross the blood–brain barrier, presenting high uptake levels in brain cancers [43].

Since the biggest challenge in targeting cancer is directly correlated with the ligands' ability to specifically recognize the cancer cells, bombesin (BN) receptors have shown to increase on-site delivery mechanisms and present a promising approach for tumor targeting [44,45]. With this in mind, due to their overexpression in different type of cancers, [^{18}F]-BAY 864367 is a peptide-receptor-based radiolabeled ligand with elevated affinities for BN receptors in patients with prostate cancer [46]. However, further clinical trials are required for bombesin receptors to be considered as a potential tool for diagnosis and/or therapy [47].

[^{11}C]-Labeled Compounds

The ^{11}C radionuclide emits with a maximum energy of 960 keV and has a half-life of only 20.4 min. The substitution of the carbon with a positron-emitting isotope in biological structures makes possible the development of specific labeled compounds, enforcing identical biochemical and pharmacological/pharmacokinetic properties to those of the natural molecules [48,49]. The short radioactive half-life of ^{11}C involves that the radiopharmaceu-

MIM Software Inc. v. Progenics Pharmaceuticals, Inc.
IPR2025-00630
Progenics EX2017

ticals labeled with this radionuclide do not require substantial radiation exposure, and allows the conduct of multiple studies for a short time interval and in the same individual. In addition, despite the fact that carbon-11 has a short half-life, it is also long enough for synthesis and purification. However, due to its radioactive decay, the radiosynthesis time should be kept as short as possible [50]. In terms of their dynamical properties, the biophysical characteristics of ^{11}C-labeled compounds, such as raclopride, FLB, and SCH, are also described within the literature [51].

The manufacture of ^{11}C-labeled compounds (Table S1) requires the availability of a cyclotron facility near the hospital where the study is to be performed, since it must be developed on-site at the time of use [48,52]. Carbon-11 decays to stable boron-11 mostly by positron emission (99.79%) and, to a lower extent, by electron capture (0.21%) [48]. According to Dahl et al., a radiotracer with a molar activity greater than 40 GBq/µmol is acceptable for most PET experiments [52]. Carbon-11 can be produced with a high molar activity in the range of 40–750 GBq/µmol at the end of synthesis [53]. [^{11}C]-carbon dioxide, [^{11}C]-methane, and [^{11}C]-fluoroform are examples of secondary [^{11}C]-synthons that have been recently developed from the primary cyclotron-produced [^{11}C]-precursors [54–58].

Regarding the [^{11}C]-radiopharmaceuticals' classification based on their vectors, the standard [^{11}C]-choline tracer is known to be taken up by cancer cells during proliferation in patients diagnosed with prostate cancer [4,59]. Since acetate is an essential substrate in cell energy and is quickly metabolized into acetyl-CoA in human cells, another salt vector-based compound is [^{11}C]-acetate [60] widely used for general cancers [4,60]. The tracer was employed in urological malignancies, renal cell carcinoma, and bladder cancer. Moreover, several studies reported that [^{11}C]-acetate PET has also been considered and used in other types of malignancies [61], such as lung carcinomas and brain tumors, and that this tracer is able to detect rare tumors (e.g., multicentric angiomyolipoma of the kidney, thymoma, and cerebellopontine angle schwannoma) [60].

In the context of prostate cancer, [^{11}C]-acetate cannot accurately distinguish between benign prostatic hyperplasia and prostate cancer, presenting comparable uptake in both conditions [62]. Another study conducted by Jambor et al. showed high sensitivity (of 88%) but low specificity (41%) of the tracer uptake in 36 patients with untreated and nonmetastatic prostate cancer [63]. In contrast, other studies [64] reported higher uptake affinities of [^{11}C]-acetate in tumor cells than in normal prostate tissue. However, potential false-positive uptakes might also account for the inflammatory effects within the cancer cells. In 2012, Schöder et al. supported these findings due to the large number of false-positive lymph nodes observed in their study, generated by chronic granulomatous disease (CGD) [65]. For the assessment of pelvic lymph nodes' involvement [66–69], several studies reported either acceptable sensitivity (68%) and specificity (78%) of [^{11}C]-acetate uptake [66] or lower patient-based sensitivity of only 38% for lymph node detection [67]. Intriguingly, other two studies reported [^{11}C]-acetate as a suitable predictor of lymph nodes' involvement [68] and a pelvic lymph node's detection with higher sensitivity (90%) and specificity (67%) [69]. As a predictive biomarker, [^{11}C]-acetate uptake was associated with higher prostate-specific antigen velocities [70]. Last but not least, a study conducted by Spick et al. showed comparable conventional bone scans and [^{11}C]-acetate PET on patient-based analysis, suggesting that PET imaging using this tracer can accurately assess distant (bone) metastatic involvements [71].

Another small-molecule-based radiotracer, known as [^{11}C]-erlotinib, is heavily used nowadays in PET scans for lung carcinomas and colorectal cancer [4]. In 2016, Bahce et al. studied the effects of erlotinib (the medication used to treat non-small-cell lung and pancreatic cancers) treatment on [^{11}C]-erlotinib uptake in lung cancer patients [72]. Five years later, Petrulli and coworkers showed that, among subjects with non-small-cell lung cancer (NSCLC) and various epidermal growth factor receptor mutations, the kinetic properties of the tracer varied substantially. In addition, they also implemented a novel scanning protocol that highlighted the pronounced heterogeneity of (non-small) CLC and its impact on [^{11}C]-erlotinib [73]. In this context, a study conducted by Yaqub et al.

MIM Software Inc. v. Progenics Pharmaceuticals, Inc.
IPR2025-00630
Progenics EX2017

aimed to find the most advantageous pharmacokinetic model for [^{11}C]-erlotinib uptake's quantification in patients diagnosed with NSCLC [74].

[^{124}I]-Labeled Compounds

^{124}I-labeled compounds (Table S1) are used for both imaging and therapy, as well as for ^{131}I dosimetry, due to the long half-life (of 4.18 days) and physical properties of the positron-emitting isotope of iodine [75]. I-124 is also an engaging radionuclide for mAbs development as potential immuno-PET imaging pharmaceuticals [76] and well-established methodologies for radioiodination [77,78]. In patients diagnosed with thyroid and parathyroid cancer, ^{124}I can be labeled against mAbs, peptides, small molecules or proteins for tumor imaging [79–81], or single molecules such as metaiodobenzylguanidine (MIBG), amino acids, and fatty acids for heart and brain disorders' investigations, including studies on neurotransmitter receptors and photodynamic therapy [82].

Moreover, iodine radioisotopes have also been widely used as theranostic agents in thyroid cancer [83]. Although there are a total of 37 known iodine isotopes that undergo radioactive decay, the conventional iodine radionuclides used for preclinical and clinical applications are ^{123}I, ^{124}I, ^{125}I, and ^{131}I.

Several ^{124}I-label-based small molecules have been developed by nucleophilic and electrophilic substitution reactions and, afterwards, tested for various targets. For instance, a few pharmaceuticals are based on small molecule, such as ^{124}I-MIBG for adrenergic activity; ^{124}I-IAZA and ^{124}I-IAZG as hypoxia agents; ^{124}I-dRFIB, ^{124}I-IUdR, and ^{124}I-CDK4/6 inhibitors of cell proliferation; ^{124}I-hypericin targeting protein kinase C; and ^{124}I-FIAU against herpes virus thymidine kinase [84]. ^{124}I-IPPM compounds target opioid receptors, and ^{124}I-IPQA engages EGFR kinase activity and ^{124}I-labeled-6-anilino-quinazoline derivatives' irreversible bind to EGFR. In addition, ^{124}I-purpurinimide derivatives are also used as tumor imaging agents [75,84].

A large array of ^{124}I-labeled compounds based on antibodies, nanobodies, antibody fragments, and proteins have been intensively used for molecular imaging of thyroid cancer, breast cancer, colorectal cancer, renal cell carcinoma, ovarian cancer, neuroblastoma, and so forth. In addition, immuno-PET imaging tracers have been considered for the detection of tumors (over)expressing human EGFR. As an example, ^{124}I-labeled ICR12—a rat mAb recognizing the external domain of the human c-Erb B2 protooncogene—was evaluated in patients diagnosed with breast cancer, while another study was focused on two ^{124}I-labeled mAbs (MX35 and MH99) evaluated in rats with subcutaneous human (SK-OV-7 and SK-OV-3) ovarian cancer xenografts [75], where, as a result, small (about 7 mm) ovarian cancer nodules were identified using PET imaging.

For the development of anti-HER2 targeting pharmaceuticals, a ^{124}I-labeled trastuzumab compound and a small (7 kDa) scaffold protein were evaluated and compared. As a result, the total uptake of trastuzumab in tumors was higher when compared with the uptake of ^{124}I-labeled scaffold protein, despite the fact that tumor-to-organ ratios were significantly higher for ^{124}I-labeled 7 kDa scaffold protein due to its higher and faster clearance from blood and normal tissues [75].

Moreover, micro-PET imaging and biodistribution studies of ^{124}I-trastuzumab were considered in order to examine the compound's specificity in HER2-positive and HER2-negative mouse models, and as a result, the authors observed elevated tumor uptake levels of ^{124}I-trastuzumab when compared with ^{124}I-IgG1 in HER2-positive mouse models. In addition, for patients diagnosed with gastric cancer (in metastatic stages), PET/CT images confirmed higher uptake specificity levels of ^{124}I-trastuzumab than the uptake levels of [^{18}F]-FDG [85].

In 2021, Kumar et al. reported in their review paper that for targeting the CD20 antigen in mice models and CD20 expressing murine lymphoma, cys-diabody (cDb) and cys-mini body (cMb) based on rituximab and obinutuzumab (GA101) were radiolabeled with ^{124}I. The use of GA101-based imaging pharmaceuticals, such as ^{124}I-GAcDb and ^{124}I-GacMb,

MIM Software Inc. v. Progenics Pharmaceuticals, Inc.
IPR2025-00630
Progenics EX2017

resulted in higher-contrast immuno-PET images of B-cell lymphoma, when compared with the rituximab-based tracers [75,86].

Other studies have reported novel heavy-chain antibodies (HCAbs) labeled with ^{124}I [87] and the development of humanized IgG mAb labeled with ^{124}I isotopes [88] for targeting cell death ligand-1 (hPD-L1), known to activate specific (T) cells associated with multiple malignancies. Moreover, fully human ^{124}I-labeled IgG monoclonal antibodies have also been tested and used as theranostic agents [89–91]. For targeting, biodistribution and safety assessments of ^{124}I-labeled compounds, Zanzonico et al. evaluated and characterized (using quantitative PET) the ^{124}I-huA33 specific tumor targeting in patients diagnosed with colorectal cancer [92].

In clear cell renal cell carcinoma (ccRCC); carcinomas of the uterine cervix, kidney, esophagus, lung, breast, colon, and brain; and hypoxic solid tumors, the transmembrane carbonic anhydrase IX protein is being overexpressed due to hypoxic conditions of the cancerous microenvironment; therefore, the protein is considered a reliable biomarker of hypoxia [75]. Within this framework, ^{89}Zr-labeled cG250 (girentuximab) compounds (as an alternative to ^{124}I) were evaluated in ccRCC xenograft models in mice. These studies concluded that, compared with ^{124}I–labeled cG250, ^{89}Zr-labeled cG250 showed higher uptake, greater retention, and superior PET image quality due to its elevated trapping rates inside the tumor cells [93,94]. However, the cG250 compounds have been labeled with a variety of radionuclides (such as ^{124}I, ^{111}In, ^{89}Zr, ^{131}I, ^{90}Y, and ^{177}Lu), and are lately most extensively investigated as CA-IX (targeting *Carbonic anhydrase*) theranostic pharmaceuticals [95–98].

In addition, for prostate cancer patients, the well-known and highly debated prostate-specific membrane antigen (PSMA) is already overexpressed in the early stages of the disease [99]. A few studies have reported that ^{124}I-capromab compounds suggested relatively lower tumor uptake, with an even lower uptake of ^{111}In-capromab in LNCaP xenografts [100]. However, in 2019, Frigerio et al. demonstrated that the uptake of the ^{124}I-labeled anti-PSMA single-chain variable fragment (scFv) is very high and specific for PSMA-positive cells [101]. Between 2013 and 2016, a humanized mAb (J591) that binds to the extracellular domain of PSMA was considered and investigated for both imaging and therapy purposes [102–106]. As a result, it has been shown that ^{124}I- and ^{89}Zr-labeled J591 compounds exhibit comparable internalization rates in preclinical prostate models [106], further implying that prostate cancer theranostics using ^{177}Lu- and ^{124}I- or ^{89}Zr-labeled J591 are not only feasible, but might also involve superior targeting rates of bone lesions relative to conventional imaging modalities [75].

In another study conducted by Knowles et al., the ^{124}I- and ^{89}Zr-labeled prostate stem cell antigen (anti-PSCA) A11 minibodies were evaluated and compared for quantitative immuno-PET imaging of prostate cancer. Here, the nonresidualizing ^{124}I-labeled minibody presented lower tumor uptake than the residualizing ^{89}Zr-labeled minibody, although the ^{124}I-labeled tracer reached higher imaging contrast due to lower nonspecific uptakes and greater tumor-to-soft-tissue ratios [107]. The same authors compared the ^{124}I-labeled A11 minibody imaging with [^{18}F]-fluoride bone scans in order to analyze the disease's progression and response to therapy, and observed that ^{124}I-labeled A11 minibody presented higher sensitivity and specificity, contrasting the [^{18}F]-fluoride bone scans in detecting the xenografts at all time points [108].

In 2018, Tsai et al. and Zettlitz et al. confirmed, using dual-modality immuno-PET/fluorescence imaging, that the labeled ^{124}I-A11 cMb-Cy5.5 presented specific targeting to both 22Rv1-PSCA and PC3-PSCA xenografts in mice, and that the fluorescence imaging signal was strong from both 22Rv1-PSCA and PC3-PSCA tumors, when compared with non-PSCA-expressing tumors [109]. Similarly, the dual probe A2 cys-diabody (A2cDb)-IR800, also targeting PSCA, labeled with ^{124}I (124I-A2cDb-IR800) ensued high-contrast immuno-PET images [110].

MIM Software Inc. v. Progenics Pharmaceuticals, Inc.
IPR2025-00630
Progenics EX2017

Last but not least, a few studies have demonstrated that the ^{124}I-codrituzumab compound, an antibody targeting glypican 3 (a cell-surface glycoprotein overexpressed in cancerous tissue), is able to detect tumor localization in most patients with HCC [75,111].

[^{89}Zr]-Labeled Compounds

Due to the fact that ^{89}Zr is thermodynamically stable and kinetically inert, can be easily produced within a few hours, and has a long half-life of 3.3 days [112], the use of ^{89}Zr tracers represents a promising approach for evaluating the in vivo distribution of monoclonal antibodies in cancer therapies [113,114]. Therefore, a large number of studies have focused on the feasibility of ^{89}Zr immuno-PET imaging, with further investigations on the effectiveness of radio-immunotherapy and imaging of target expression, detection of targeted tumors, and monitoring of anticancer chemotherapies. Additionally, ^{89}Zr-labeled radiopharmaceuticals have applications in nanoparticle imaging and cell tracking [113].

According to Yoon et al. [113], among all synthesized ^{89}Zr-labeled antibodies, trastuzumab [115–117] is the most frequently employed antibody, followed by bevacizumab [118–125], cetuximab [126–128], and rituximab [129,130]. Similarly, the most frequently engaged targets are human epidermal growth factor receptor 2 and 3 (HER2, HER3), epidermal growth factor receptor (EGFR), vascular endothelial growth factor A (VEGF-A), cluster of differentiation (CD) 8 and 20, and PSMA [113].

The antibody-based [^{89}Zr]-tracers (Table S1) are extensively used in prostate cancer [103,131], pancreatic cancer [132,133], bladder cancer [132,134], gastrointestinal adenocarcinoma [127,135–139] and renal cell carcinoma [95,98,137,140–143], solid malignancies [119,121,144–146] and cell lung carcinomas [121,144], and breast cancer [116,129,134,147,148].

Several studies have investigated the feasibility and usefulness of an ^{89}Zr radiolabeled compound with J591 monoclonal antibody (mAb)—known to bind the PSMA extracellular domain—in identifying tumor foci [103,104,149–151]. In 2019, a few studies assessed the pharmacokinetic and biodistribution properties of an ^{89}Zr-labeled DFO-MSTP2109A antibody [152] and confirmed the tracer's excellent uptake in both soft tissue and bone lesions.

For patients diagnosed with breast cancer, studies reported several treatment and/or diagnosis options based on an ^{89}Zr-labeled compound, highly dependent on the (human) epidermal growth factor receptor 2 (HER) assessment [115,116,118,144,153–158]. Moreover, in 2013, for patients diagnosed with head and neck types of cancer, Heukelom et al. analyzed the [^{89}Zr]-cetuximab uptake in the view of chemoradiotherapy selection using either the antiepidermal growth factor receptor (EGFR) mAb cetuximab or cisplatin [159,160]. In addition, Loon et al. performed a phase I trial for patients with head and neck and lung cancer, where the [^{89}Zr]-cetuximab compound (a mAb that blocks the EGFR) was used [161].

Lamberts et al. used [^{89}Zr]-MMOT0530A for patients with pancreatic and ovarian cancer and concluded that the use of this compound in conjugation with an antibody drug conjugate, DMOT4039A, may present promising results for individualized antibody-based treatment guidance [133]. A year later, Bensch et al. studied [^{89}Zr]-lumretuzumab's uptake before and during the treatment (with the HER3-antibody lumretuzumab) in patients with solid tumors [146]. Additionally, the same authors evaluated the feasibility of the [^{89}Zr]-atezolizumab PET imaging tracer in solid malignancies [134].

In 2020, Pandit-Taskar et al. successfully implemented first in-human imaging using ^{89}Zr-IAB22M2C as a radiolabeled body against CD8+T cells in patients diagnosed with solid malignancies [151]. Previously, several studies were focused on the biodistribution and tumor accumulation/uptake of ^{89}Zr-labeled compounds (e.g., [^{89}Zr]-labeled cergutuzumab amunaleukin (CEA-IL2v) [162] and [^{89}Zr]-GSK2849330 [145]) in patients with advanced solid tumors [160].

[^{64}Cu]-Labeled Compounds

With a medium half-life of 12.8 h, [^{64}Cu]-radionuclide has a unique decay profile [114,163], and it is used for PET diagnostic imaging [164] but also for targeted

MIM Software Inc. v. Progenics Pharmaceuticals, Inc.
IPR2025-00630
Progenics EX2017

(radio)therapy. It can be easily conjugated against proteins, antibodies, and/or peptides [112,165].

In the last decade, [^{60,62,64}Cu]-diacetyl-bis (N4-methylthiosemicarbazone) (Cu-ATSM)-labeled PET radiopharmaceuticals have been developed for targeting the hypoxic regions in tumors [166–168]. For [^{64}Cu]-ATSM, one of the recently described uptake mechanisms is that Cu(II)-ATSM is reduced by thiols and, consequently, converted into the Cu(I)-ATSM complex in both normal and hypoxic conditions [169].

For head and neck squamous cell carcinomas, McCall et al. investigated the role of [^{64}Cu]-ATSM (HNSCC) using a combination of in vivo PET imaging and in vitro autoradiography [166]. The results of the study indicated a significantly higher uptake of [^{64}Cu]-ATSM in tumors than the uptake in muscles, therefore concluding that [^{64}Cu]-ATSM uptake is specific for malignant expression [165,166]. A few studies [167,168] have assessed the prognostic significance of [^{64}Cu]-ATSM in patients with locally advanced non-small-cell lung cancer or head and neck cancer prior to treatment. However, no significant differences were found between early (1 h postinjection) and late (16 h postinjection) acquisitions [165], with [^{64}Cu]-ATSM showing high sensitivity but low specificity in therapy response prediction, a result that can be correlated with undetectable rates of hypoxia [167,168].

With respect to [^{60}Cu]-radionuclide, the studies focused on cervical cancer and predicting the tumor response post-therapy; observed that the [^{60}Cu]- and [^{64}Cu]-ATSM magnitude of uptake are similar, even if [^{64}Cu]-ATSM presented a better image quality; and concluded that indeed [^{64}Cu]-ATSM may be a more suitable predictive indicator of tumor response to therapy in patients diagnosed with cervical cancer [165].

In rat models, there is a good correlation between low oxygen partial pressure and high [^{64}Cu]-ATSM uptake. However, preclinical data suggested that [^{64}Cu]-ATSM should not be considered as a hypoxia marker in all types of tumor. For instance, in a study conducted by Vāvere et al., the interplay factors between [^{64}Cu]-ATSM and the overexpression of fatty acid synthase were directly correlated with prostate cancer, despite low [^{64}Cu]-ATSM uptake levels caused by elevated hypoxic conditions [165].

As for other standard [^{64}Cu]-based radiopharmaceuticals, [^{64}Cu]-labeled monoclonal antibodies are widely used for the detection of small colorectal tumor foci in the abdomen and pelvis, and [^{64}Cu]-DOTATATE was developed for neuroendocrine tumor imaging and is currently considered in several ongoing clinical trials due to its favorable pharmacokinetics and high stability [163].

In terms of novel approaches, the [^{64}Cu]-PSMA compound (included in Table S1) seems feasible for prostate cancer detection [163], [^{64}Cu]-dichloride is used for copper trafficking in metabolic diseases [170,171], and [^{64}Cu]-labeled peptides based on uPAR biomarkers (already developed and administrated to humans) can be used for glioblastoma [163]. Additionally, as previously stated at the beginning of this section, due to the radionuclide's unique decay profile, ^{64}Cu can also be used for internal radiotherapy since its favorable β-decay (38%) and Auger electrons emitted from this nuclide are able to damage the tumor cells [172–174].

[^{68}Ga]-Labeled Compounds

Gallium has 31 known isotopes and 11 metastable isomers (the two naturally occurring stable isotopes gallium-69 (60.11%) and gallium-71 (39.89%)). The two gallium isotopes applied for nuclear medicine imaging are gallium-67, with a longest half-life of 3.26 days, and gallium-68, with a half-life of just 67.7 min [112,114,175,176]. Gallium-68 is the most widely used radionuclide, labeled against PSMA-11 and in combination with [^{177}Lu]-Lu-DOTA-PSMA-617, in the diagnosis of prostate cancer with additional theranostic application, due to ^{68}Ga/^{177}Lu-radiolabelled tracers' similar biological behavior [177]. Moreover, a ^{68}Ga theranostic pair is also considered for neuroendocrine tumors. In this context, the most widely used analogues of somatostatin with gallium-68 are [^{68}Ga]-Ga-DOTA-TOC, [^{68}Ga]-Ga-DOTA-TATE, [^{68}Ga]-Ga-DOTA-LAN, and [^{68}Ga]-Ga-DOTA-NOC [178]. Additionally, yttrium-90 and lutetium-177 are used as therapeutic

MIM Software Inc. v. Progenics Pharmaceuticals, Inc.
IPR2025-00630
Progenics EX2017

counterparts [175]. Several ^{68}Ga-labeled radiopharmaceuticals based on exendin-4 (a glucagon-like protein-1 receptor agonist) have been developed, and it was shown that this type of tracers (e.g., [^{68}Ga]-Ga-DOTA-exendin-4) is able to accurately localize small pancreatic tumors known to produce an excessive amount of insulin. It was also demonstrated that [^{68}Ga]-Ga-DOTA-exendin-4 identifies these insulomas significantly better than ^{111}in-labelled radiopharmaceuticals [179].

For the gastrin-releasing peptide receptor's (GRPR) imaging, which is overexpressed in several types of cancer, such as prostate cancer, breast cancer, colorectal and pancreatic cancer, and lung and ovarian cancer, several gallium-68-based radiopharmaceuticals were designed [175], specifically [^{68}Ga]-Ga-BBN-RGD for breast cancer [180], [^{68}Ga]-NOTA-DUPA-RM26 for prostate cancer, and [^{68}Ga]-Ga-NOTA-Aca-BBN for glioma imaging [181]. Similarly to metallic [^{89}Zr]-radiolabeled compounds, ^{68}Ga-based radiopharmaceuticals (Table S1) are used for targeting human epidermal growth factor receptors (HER2) [182] and carcinoembryonic antigen (CEA), which is highly increased in certain types of cancer, but also in benign conditions.

2.1.2. PET Radiopharmaceuticals in Neurology

Without engaging any pharmacological effects, a large variety of PET radiotracers are now considered depending on the targeted biological (in this section, neurological) conditions. Among all these conditions, the worth-noting ones are based on differentiating frontotemporal dementia in Alzheimer disease (AD) [183], developing key biomarkers that can accurately detect the receptors of interest in Huntington's disease (HD) [184,185], differentiating other neurodegenerative disorders [186] through molecular phenotyping, diseases' severity evaluations, seizure onset areas in epilepsy, encephalitis location and diagnosis [183], brain tumor prognosis, and tumoral extent delineations [187].

Within the central nervous system (CNS), the molecular sensitivity of the PET imaging technique enables the quantification of target-ligand interactions with great selectivity in humans, and became particularly useful in further understanding the pathologies and identifying potential new targets for therapeutic purposes. Several well-known and widely debated radiopharmaceuticals for brain imaging include [^{18}F]-FDG compounds used for imaging the alterations of glucose metabolism [188,189], [^{18}F]-FDOPA tracers for dopamine synthesis in schizophrenia and PD, and other tracers for translocator proteins' detection in AD and/or PD. In addition, [^{11}C]-PIB pharmaceuticals are extensively used for tracking the amyloid β plaques' accumulation in AD [190].

In general, the passive diffusion of PET tracers into the brain must follow a lower molecular weight (<500 kDa), a lipophilic coefficient between 1 and 5 (at physiological pH), and a topological polar surface area below 90 Å^2 [191–193]. In terms of pharmacokinetic properties, the essential criteria of all CNS tracers rely on their ability to cross the BBB, while the tracer's selectivity ultimately influences its usefulness and applicability. However, other relevant parameters regarding the targets' expression, alteration in their affinity states (high or low), internalization, and changes in endogenous occupancy must be also considered [194,195].

Since 2012, a consistent number of PET tracers have been developed and evaluated for the detection of abnormal and insoluble accumulation of misfolded proteins within brain cells, considered to be the responsible factors in AD, PD, and HD pathologies [183]. These accumulations in the human brain are known as amyloid β plaques, tau, α-synuclein, and/or fibrils [196].

Amyloid PET tracers (Table S2) are used for the detection of pathological amyloid depositions within the brain tissue [197] (including the white matter), and are mainly benzothiazole and benzoxazole derivatives [196,198–203], such as [^{18}F]-flutemetamol, [^{18}F]-florbetapir, and [^{18}F]-florbetaben [204,205]. In patients presenting mild cognitive impairment and AD, high cortical fibrillar amyloid loads were observed when [^{18}F]-flutemetamol, [^{18}F]-florbetapir, [^{18}F]-florbetaben, and [^{18}F]-flutafuranol compounds were used [206–208]. Recently, other tracers with improved binding specificity and diminished bone uptake (e.g.,

MIM Software Inc. v. Progenics Pharmaceuticals, Inc.
IPR2025-00630
Progenics EX2017

[^{18}F]-FIBT, [^{18}F]-FACT, and [^{18}F]-D15FSP), and others that are able to detect diffuse amyloids (e.g., [^{18}F]-fluselenamyl) were also developed [201,209–211]. In amyloid transgenic mouse models [200,202], several antibody-based PET/SPECT radiotracers, particularly [^{124}I]-RmAb158-scFv8D3 and [^{124}I]-8D3-F(ab')2-h158, have been proposed while showing an adequate BBB entrance.

For treating affective disorders, such as depression, drugs must target the serotonergic system consisting of serotonin (5HT) G-protein-coupled-receptor families and a ligand-gated channel family [212]. Therefore, examples of PET radiotracers with distinctive affinities towards the 5HT system include [^{18}F]-MPPF, [carbonyl-^{11}C]-WAY-100635 for $5HT_{1A}$, [^{18}F]-altanserin, and [^{11}C]-MDL for $5HT_{2A}$, [^{11}C]-GSK215083 for $5HT_6$ [213,214], and [^{11}C]-DASB for the 5HT transporter [212].

The aggregation rates of tau proteins (negative regulators of mRNA translation) represent a pathologic hallmark of AD and are directly correlated with the disease's progression [215]. Between 2013 and 2018, 12 PET tracers were developed, including [^{18}F]-AV-1451 and [^{18}F]-THK [216], being the most extensively studied [217]. Among others, the [^{18}F]-AV-1451 tracer exhibits high selectivity and fast kinetics, allowing for an accurate description of the disease's stages [218–236]. However, it also presents low affinity patterns for non-AD tau accumulations [230,233–235], restricting the tracer's use for other tau-related neuropathies' imaging.

As previously stated, [^{18}F]-THK (523) represents another highly debated tau radiotracer, with its first implementation in humans in 2014 [236]. In both healthy controls and AD conditions, [^{18}F]-THK (523)'s uptake regions are mainly described by subcortical white matter areas, with medium selectivity over amyloids. Until 2016, three other [^{18}F]-THK-based PET tracers were developed and tested in human [237–239], showing highest uptake in cerebellar grey matter regions [237,238,240–242], improved properties over [^{18}F]-THK (523), and better differentiation between AD and healthy controls [241,243]. Table S2 highlights additional radiotracers used for tau protein aggregate imaging, the available in vitro and ex vivo binding studies [244] indicating potential off-target bindings of in-human tau tracers [230–232,245–247], and limited data for in vivo selectivity reports [248].

Taking into consideration that many neurological disorders are directly correlated with particular dysfunctions of the neuroreceptors, transporters, and/or synaptic proteins [249,250], the imaging of the abnormal accumulation of tau filaments is also associated with different affinities of tau tracers for their distinctive binding sites [251,252]. In addition, several in vivo studies have identified a link between the cholinergic system and AD, PD (with dementia), and Lewy body pathologies; therefore, multiple potential targets for cholinergic imaging were also considered [253–260]. Examples of these tracers include [^{18}F]-FEOBV, [^{18}F]-VAT, and [^{18}F]-ASEM with their heterogeneous distribution in line with the target distribution and fast kinetics within most brain areas [259–267].

Adenosine 2A receptors (A_{2A}) are G-protein-coupled receptors targeted by CNS neurotransmitters and highly implicated in multiple neurological disorders [268], such as schizophrenia, bipolar disorder, HD, PD, preclinical models of AD, addiction, aging, epilepsy, and multiple sclerosis [269,270]. In this framework, the most reliable tracers developed for targeting A_{2A} are [^{11}C]-TMSX and [^{11}C]-SCH442416. However, the pharmacokinetic properties of these tracers, despite the fact that they can easily cross the BBB, imply nonspecific bindings in humans, with a low dynamic range of receptor occupancy [270]. To overcome this limitation, in 2015, Barret et al. [271,272] developed the [^{18}F]-MNI-444 tracer with a promising characterization of the adenosine receptors across multiple regions of the brain (striatal and cerebellum areas). The [^{18}F]-MNI-444 radiotracer appears superior for A_{2A} imaging in the CNS to the other evaluated tracers, presenting a higher selectivity and better pharmacokinetic properties for imaging [271,272]. It also presents higher retention in the striatum and fast washout in the cerebellum, where the concentration of A_{2A} is very low [270].

For targeting synaptic vesicle glycoprotein 2A (SV2A) [273], which is specifically expressed in synaptic terminals and particularly studied for antiepileptic treatment devel-

MIM Software Inc. v. Progenics Pharmaceuticals, Inc.
IPR2025-00630
Progenics EX2017

opment, the [^{11}C]-UCB-J and [^{18}F]-UCB-H radiotracers have recently been proposed [274]. Both [^{18}F]-UCB-H and [^{11}C]-UCB-J compounds show a high degree of SV2A-specific bindings and fast kinetics [275], with [^{11}C]-UCB-J presenting higher stability rates, when compared with the other one in healthy controls' test–retest scans [276–278].

Other tracers targeting different types of receptors (Table S2) include: [^{11}C]-BU99008, being the only tracer for imidazoline receptors in humans with great response in blocking studies [279–282] but showing slow kinetics and therefore requiring long scan times; [^{11}C]-ITMM, which shows promising performance in preclinical studies for targeting metabotropic glutamate receptor 1 [283–288], however requiring long scan times and presenting low brain uptake and slow metabolism [289]; [^{11}C]-GR103545 and [^{11}C]-LY2795050 tracers, have recently been tested in humans for targeting K opioid receptors [290–292]; and [^{11}C]-Cimbi-36 tracers, target the serotonin 5-HT$_2$ receptor subtype [293–295] with high binding selectivity and relatively high uptake levels in cortical areas, although showing moderately slow pharmacokinetic profiles [296]. Additionally, for CNS enzyme targets in humans, several new PET radiotracers were developed between 2013 and 2018, including [^{11}C]-PS13 [297,298], [^{18}F]-BCPP-EF [299–305], [^{11}C]-martinostat [306–308], [^{18}F]-MNI-654 [309], and [^{11}C]-MK-3168 [310–312]. Further details regarding this type of tracers and many others are highlighted in Table S2.

Lu et al. announced the discovery of [^{18}F]-LSN3316612 as a novel PET ligand for measuring *O*-linked-*N*-acetyl-glucosamine (O-GlcNAc) hydrolase (OGA) in the human brain. It increases tau protein phosphorylation, which is a biomarker for AD. Moreover, the research was expanded to include PET quantification of O-GlcNAcase in the brains of healthy human volunteers using [^{18}F]-LSN3316612, with V_T calculated using a two-tissue compartment model, as well as region-based and voxel-based quantification of [^{18}F]-LSN3316612 in the human brain for O-GlcNAcase [313,314]. Lindberg et al. created the radioligand [^{18}F]-AZ10419096 for imaging 5-HT1B receptors. The anomalies of the 5-HT1B receptor are linked to CNS illnesses, including anxiety and depression, and have become a great indicator of examination using PET. AZ10419096 demonstrated selectively high brain uptake into the 5-HT1B receptor in a baseline PET analysis with [^{18}F]; however, in a blocking PET investigation with an AR-A000002 blocker, the binding was found to be 80% in the occipital cortex, suggesting strong specific binding [315].

The [^{18}F]-MK-6240 compound, a new radiotracer for imaging neurofibrillary tangles, was described by Koole et al. Tangles are a significant pathogenic hallmark of Alzheimer's disease that is linked to cognitive deterioration. Preclinical toxicity studies, first-in-human biodistribution, and dosimetry studies for clinical application in imaging investigations of the human brain have all validated the safety of [^{18}F]-MK-6240 [316].

The new radioligand [^{11}C]-MC1 was described by Shrestha et al. for imaging the low-density cyclooxygenase 2 (COX-2) enzyme in the human brain. Neuroinflammation requires it as a target. In healthy brain tissue, COX-1 expression is high, whereas COX-2 expression is low, although it is elevated during the inflammatory process. This [^{11}C]-MC1 is a selective radioligand for COX-2, and it was discovered that it detected high-density COX-2 in symptomatic joints in rheumatoid arthritis patients. The particular binding to COX-2 was validated by blocking tests with celecoxib in this work, which showed significant absorption of [^{11}C]-MC1 in the human brain [317].

In 2021, Yan et al. used the PET radioligand [^{11}C]-deschloroclozapine ([^{11}C]-DCZ) to measure the number of muscarinic DREADDs transfected in monkey brains. Due to a substantially lower background uptake, the signal-to-background ratio of [^{11}C]-DCZ was about twofold larger than that of [^{11}C]-clozapine ([^{11}C]-CLZ) in the monkey DREADD model. As a result, [^{11}C]-deschloroclozapine appears to have a higher selectivity for DREADD hM4Di receptors than [^{11}C]-CLZ [318]. DREADDs (designer receptors exclusively activated by designer drugs) are a new chemogenetic technique that may be used to activate or inhibit distinct neuronal populations in the brain, allowing for the regulation of various neurological diseases [319].

MIM Software Inc. v. Progenics Pharmaceuticals, Inc.
IPR2025-00630
Progenics EX2017

The first-in-human assessment of a new radioligand, [^{11}C]-PS13, to measure cyclooxygenase-1 (COX-1) in the brain was published by Kim et al. [320]. The vesicular monoamine transporter 2 (VMAT2) protein is used as a biomarker to assess PD symptoms. VMAT2 receptors transport and store the produced dopamine in the synaptic storage vesicles in the striatal cells. As a result, a recent study used micro-PET to produce a new radiotracer, 10−(+)−[^{11}C]-DTBZ, for in vivo PET imaging of VMAT2 to better understand PD [321].

Even though [^{18}F]-FDG is widely used and exhibits great performances in brain imaging, a research group reported a potential PET tracer with even more potential for brain glioma imaging. Thus, *N*-(2-[^{18}F]-fluoropropionyl)-L-glutamate ([^{18}F]-FPGLU) showed remarkable visibility of the tumor and the capability to detect tumor activity [322].

With so many tracers on development that show great feasibility, the future prospects of PET imaging in a wide range of diseases is rather encouraging. The possibility of exceeding the performances of current radiopharmaceuticals in clinical use is also to be considered; thus, further testing of the available potential agents is mandatory.

2.1.3. PET Radiopharmaceuticals for Cardiovascular Events

The first application of radiotracers for myocardial blood flow studies in humans was reported in 1927. Among all nuclear cardiology techniques, myocardial perfusion imaging is nowadays the most heavily used. Nuclear cardiology has extended its implementations over the last decades to heart function, blood circulation, and noninvasive imaging of myocardial viability, cardiac inflammation, cardiac metabolism, and prognosis [323,324].

The most important properties of an ideal PET/SPECT radiotracer for myocardial perfusion imaging include a physical half-life of the radionuclides that allows sufficient time for image acquisition and repeated measurements, easy and stable labeling, optimal radiation dosimetry for integral test–retest evaluations, high myocardial uptake, linear dependence between the myocardial uptake and coronary blood flow, rapid blood clearance, and, lastly, high target-to-background ratio involving lower radiotracer uptake levels in the adjacent organs, such as lungs, stomach, liver, and bowels [323,325,326].

For the myocardial uptake assessment [327] or the myocardial blood flow measurement [328,329], [^{13}N]-ammonia represents a suitable radiotracer [330–332], however, imposing some limitations due to its physical half-life of 10 min. Conversely, rubidium-82 has the advantage of its short half-life of only 75.5 s [333–338], allowing for complete rest–stress studies within 30 min. Moreover, it exhibits high diagnostic accuracy in the clinical detection of coronary artery disease [339]. Another promising radiotracer, an analogue of mitochondrial (complex I) inhibitors, is represented by the [^{18}F]-flurpiridaz compound [340,341].

Keeping in mind that the heart acquires its energy to pump from several sources, including glucose, ketones, and free fatty acids, various radiotracers targeting these sources (see Table S3) were investigated to study different aspects of cardiac metabolism [342]. In 2018, Manabe et al. classified in their review article the cardiac imaging radiotracers into: inorganic tracers, radiometal ions, small organic tracers, and radiometal complexes [342]. The inorganic radiopharmaceuticals, labeled with short half-life radionuclides, such as ^{13}N and ^{15}O [343] (10 and 2 min, respectively), have been widely used for cardiac perfusion imaging. Additionally, the radiometal positron emitter $^{82}Rb^{+}$, presenting an ionic radius comparable to that of K^{+} in its monovalent cationic form and belonging to the same family as K (such as alkaline metals), exhibits kinetics similar to those of K^{+} and has been extensively engaged as a PET imaging tracer [344]. Other than cationic radionuclides, the monovalent anion $^{18}F^{-}$ has been widely used for calcification lesion imaging in bone PET scans [345]. With regard to small organic tracers, ^{11}C-epinephrine and ^{18}F-fluorodopamine are also used to image the presynaptic sympathetic nervous system of the heart [346], since it plays an essential role in the abnormal processes associated with various cardiac diseases. In addition, in terms of cardiac inflammation [347], but also for various CNS pathologies and psychiatric diseases [348–350] as previously discussed in Section 2.1.2, the translocator proteins encoded by translocator protein (TSPO) genes and mainly expressed on the outer

MIM Software Inc. v. Progenics Pharmaceuticals, Inc.
IPR2025-00630
Progenics EX2017

mitochondrial membrane are considered suitable targets for the radiolabeled receptor ligands in PET imaging [351]. Among the tracers used for targeting TSPO receptors, [^{11}C]-PK11195 is used for carotid stenosis imaging and shows a great potential for detecting inflammatory macrophages in atherosclerotic plaques as well [352]. Additionally, several next-generation TSPO-targeted radioligands have been developed to improve the binding specificity and to lower the signal-to-noise ratio for neuroinflammation imaging, subsequently enhancing the cardiovascular inflammation imaging performance [349,350]. Here, other tested radiolabeled compounds include [^{18}F]-FEDAA1106 [347], [^{18}F]-FEMPA [353], and [^{18}F]-GE180 [354].

The approved PET tracers for myocardial perfusion imaging and their molecular targets include [^{82}Rb]-chloride targeting Na^+/K^+ ATPase cotransporters (the most commonly used), [$^{13}NH_3$]-ammonia [355] with a retention in the myocardium mediated by the ATP-dependent conversion of glutamate to glutamine, and the traditional H_2 ^{15}O [356,357], which is not metabolically retained in tissues but used as a standard validation against which other tracers are being evaluated for optimal myocardial blood flow quantification [358].

For targeting mitochondrial complex I and the mitochondrial membrane, research regarding novel PET tracers has been oriented towards ^{18}F radioisotope due to its relatively long half-life of 110 min, enabling tracer synthesis, but short positron range, allowing for higher image spatial resolutions [358]. Within this framework, the novel ^{18}F-labeled tracers are classified considering two mechanisms of mitochondrial targeting: (1) targeting mitochondrial complex I through analogues, MC1 inhibitors, which specifically bind to the MC1 receptors on the inner mitochondrial membrane, and (2) targeting mitochondrial membrane considering lipophilic cations that are able to penetrate it through electrical potential voltage gradients [359,360]. Within the first targeting mechanism group, the PET tracers include [^{18}F]-flurpiridaz [340,341,361,362], [^{18}F]-FPTP2 [363,364], and [^{18}F]-FDHR [358], whereas from the second targeting mechanism group, novel PET tracers include [^{18}F]-FBnTP, [^{18}F]-FTPP [358], and [^{18}F]-FPTP [365].

In 2020, Heo et al. published a review article dedicated to current and novel PET/SPECT radiopharmaceuticals specifically used to image cardiovascular inflammatory diseases [366]. They stated that imaging cardiovascular inflammation presents several challenges, from the small sizes of atherosclerotic lesions and complex pathophysiological characteristics of atherosclerotic plaques, to targeting the specificity and sensitivity of the required radiotracers and their pharmacokinetic properties. However, PET imaging techniques are preferred owing to their high sensitivity, quantitative and functional detections, noninvasive nature, and well-established approaches for human translation [366–368]. Going back to the great importance of glucose metabolism that is significantly enhanced in activated inflammatory cells, glucose transporters such as GLUT-1 and GLUT-3 [369], among many blood cell types, such as monocytes, macrophages (M0, M1, and M2), neutrophils, B cells, T cells, and platelets, are known to lead to higher accumulation of metabolized glucose analogues, including the gold standard [^{18}F]-FDG [358,370].

The chemokine receptors are also considered promising targets for imaging inflammatory diseases, such as atherosclerosis and its corresponding complications. The alpha-chemokine CXCR4 receptor [371] acts as a biomarker of atherosclerosis in both humans and animal models. Several studies have demonstrated that CXCR4's specific uptake of [^{68}Ga]-pentixafor is associated with calcified plaques of carotid stenosis and other cardiovascular risk factors, proving the radiotracer's potential for further evaluation of atherosclerotic lesions. The same studies also demonstrated the CXCR4's upregulation within rabbit and human plaques, mainly colocalized with macrophage staining through immunohistochemistry [372–376]. Moreover, [^{68}Ga]-pentixafor PET images of postmyocardial infarction patients presented significant differences in the radiotracer's uptake, designating different degrees of inflammatory responses. The tracer's uptake might also be able to predict heart failure in postmyocardial infarction patients and to detect culprit plaques within the coronary arteries.

MIM Software Inc. v. Progenics Pharmaceuticals, Inc.
IPR2025-00630
Progenics EX2017

The [^{64}Cu]-DOTA-ECL1i radiotracer is another compound widely used for cardiovascular inflammation and is also being investigated as an imaging agent in clinical trials for imaging lung inflammation [377,378] and pancreatic cancer. In addition, in mouse models of atherosclerotic plaque, [^{64}Cu]-DOTA-ECL1i shows decreased levels of monocytes and macrophages, playing as an indicator of inflammatory leukocyte migration to plaque regression [379], therefore being able to image leukocytes in vivo [380]. Other ^{64}Cu-radiolabeled compounds, including [^{64}Cu]-DOTA-DAPTA and [^{64}Cu]-DOTA-DAPTA-comb, which has a conjugated polymeric structure, were tested in a femoral artery injury of atherosclerosis-prone apolipoprotein E-deficient (apoE−/−) mice model, showing high uptake levels in injured lesions. However, the second tracer, a nanoparticle-based one, showed even higher accumulation rates when compared with the first tracer [381]. Moreover, in the same mice model, in vivo blocking studies using [^{64}Cu]-DOTA-vMIP-II demonstrated that more than eight chemokine receptors, including CCR1, CCR2, CCR3, CCR4, CCR5, CCR8, CXCR4, and CX3CR1, contributed to the uptake [382].

With respect to [^{68}Ga]-labeled radiopharmaceuticals (Tables S1 and S3), several preclinical studies showed specific bindings of [^{68}Ga]-DOTATATE and [^{68}Ga]-DOTANOC compounds to macrophages originated from blood monocytes in the atherosclerotic plaques of mouse aorta [383,384]. Studies focused on [^{68}Ga]-DOTATATE and [^{64}Cu]-DOTATATE tracers also showed increased uptakes in coronary arteries and large arteries [385,386], reporting a direct correlation between these radiotracers' uptake and cardiovascular risk factors' assessment, but with a potential higher uptake performance for [^{64}Cu]-DOTATATE [387,388].

Another radiotracer using DOTATATE peptide as vehicle molecule, the [^{177}Lu]-DOTATATE compound was approved for the radionuclide therapy of gastroenteropancreatic neuroendocrine tumors and showed that its use during the treatment significantly reduced the [^{68}Ga]-DOTATATE accumulation in plaques, encouraging this particular therapy against inflammatory conditions related to plaques [389].

The [^{18}F]-2-fluoro-2-deoxy-D-mannose ([^{18}F]-FDM) tracer presents similar in vivo and ex vivo uptakes to ^{18}F-FDG in atherosclerotic rabbits, however, imposing much higher in vitro uptake levels into macrophages, contrasting ^{18}F-FDG [390]. A probable explanation for this might involve [^{18}F]-FDM's uptake mechanism, since mannose—the sugar monomer of the aldohexose series of carbohydrates—is taken up by macrophages through the protein family GLUTs; therefore, [^{18}F]-FDM total uptake depends not only on GLUTs but also on macrophage mannose receptors, being able to provide additional insights when compared with ^{18}F-FDG. However, it might also mean that they could share the same PET imaging limitations of [^{18}F]-FDG.

Another tracer with higher standardized uptake values in abdominal aortas of atherosclerotic rabbits, when compared with ^{18}F-FDG, is the [^{68}Ga]-labeled NOTA-neomannosylated human serum albumin ([^{68}Ga]-NOTA-MSA) [391]. Moreover, several [^{68}Ga]-labeled macrophage mannose receptor antibodies or nanobodies were studied in atherosclerotic mouse and/or rabbit models, showing higher accumulation rates in aortas, when compared with healthy control models. In 2018, Senders et al. concluded that the uptake levels of [^{68}Ga]-labeled macrophage mannose receptors, together with [^{18}F]-FDG and [^{18}F]-NaF, exhibit different inflammatory cell populations and uptake mechanisms [392]. Moreover, a year before, Varasteh et al. targeted mannose receptor expression in macrophages on atherosclerotic plaques of apolipoprotein E-knockout mice using tilmanocept compound labeled with [^{111}In], and observed that [^{111}In]-tilmanocept accumulated in mannose receptor-expressing organs, such as liver and spleen, but associated with only low residual blood signal. The same study concluded that a tilmanocept-radiolabeled compound might represent a promising tracer for noninvasive detections of macrophages in atherosclerotic plaques [393].

Hellberg et al. conducted in 2016 a retrospective imaging study using the PET tracer [^{18}F]-fluoromethylcholine ([^{18}F]-FMCH) and demonstrated that type 2 diabetes enhances the arterial uptake of choline in atherosclerotic mice models, when compared with nondiabetic models, even though both models showed comparable macrophage content [394]. The study also provides diagnostic advantages for choline transportation imaging in pa-

MIM Software Inc. v. Progenics Pharmaceuticals, Inc.
IPR2025-00630
Progenics EX2017

tients diagnosed with type 2 diabetes, since PET imaging with [^{18}F]-FDG can be quite challenging due to elevated blood glucose levels in those patients. In the same year, Vöö et al. demonstrated the feasibility and potential of the [^{18}F]-FCH tracer to evaluate the vulnerable plaques and to differentiate them from the stable ones [395]. The [^{18}F]-FLT is another PET radiopharmaceutical compound that showed higher uptake levels not only in atherosclerotic plaques of mice and rabbit models but also in humans. However, when compared with [^{18}F]-FDG, [^{18}F]-FLT showed no significant myocardial uptakes [396], but uptakes in other proliferating cells (parenchymal cells) might affect [^{18}F]-FLT's specificity, considering that endothelial and smooth muscle cells also contain plaques.

Last but not least, other PET tracers widely used or recently developed for cardiovascular imaging or to monitor treatments' efficacy include [^{89}Zr]-DNP [397], [^{18}F]-macroflor [398], [^{111}In]-DANBIRT [399,400], and [^{18}F]-FB-IL2 [401]. Since matrix metalloproteinases (MMPs)—or matrixins—represent a family of proteinases with multiple and crucial roles in the inflammatory processes, imaging the MMPs could provide insights not on the density of macrophages, like most probes, but on their activity to promote inflammation and plaque ruptures. In this context, the [^{111}In]-DTPA-RP782-radiolabeled MMP inhibitor has been considered for molecular imaging of atherosclerosis and aneurysm and, particularly, monitoring of distinctive MMP activities [402–405]. More preclinical and clinical studies are mandatory to further assess its feasibility; nevertheless, the development of these selective MMP inhibitors is already in progress [406–408] in order to minimize the side effects of treatments.

2.1.4. PET Radiopharmaceuticals for Bacteria Imaging

Taking into account the heterogeneity of animal models and bacterial strains, Auletta et al. classified the research studies focused on bacteria PET imaging (Table S4) based on the type of bacterium (Gram-positive, Gram-negative, Gram-positive and negative, others) [409]. According to the literature, most studies that used Gram-positive bacteria imaging obtained better results in terms of radiopharmaceutical binding in both animal models and humans. Ubiquicidin peptide fragments, specifically UBI-31-38 and UBI-29-41, are reported to have enabled the imaging of *Staphylococcus aureus* (*S. aureus*) infection foci in models with high target-to-nontarget ratios. However, even though the preliminary results showed safety in terms of toxicity rates in humans, further research must be conducted [410–413].

The ^{124}I-labeled FIAU compound reported good results in animal models; however when translated to humans, the results were less promising [414]. [^{18}F]-FDG-6-P agents are potential substrates for bacterial hexose phosphate transporters, heavily expressed in many bacteria species, and present the ability to discriminate between infection and sterile inflammation; thus further research might confirm their initial potential as a new radiopharmaceutical for bacteria imaging [415]. Compared with [^{18}F]-FDG, [^{18}F]-FDG-6-phosphate shows similar biodistributions both visually and semiquantitatively. However, in contrast with [^{18}F]-FDG, [^{18}F]-FDG-6-phosphate indicates no accumulation in sterile inflammation of noninfected mice models [415].

The radiolabelled ciprofloxacin showed high specificity when labeled with gallium-68 [416], but interestingly, when labeled with technetium-99m [417] or fluorine-18 [409], the results led to nonspecific patterns. Their divergent results involved no apparent specific interactions, and the uptake using both radionuclides was rapidly cleared. Note that it is worth concluding that the difference between the used isotopes and the labeling chemistry might affect the biological behavior of radiopharmaceuticals [409]. Most studies conducted using Gram-positive bacteria reported promising results when radiolabeled glucose analogues were used, particularly for [^{18}F]-FDS compounds that showed high binding specificity to *E. coli* or *K. pneumoniae* [418–420].

Other sensitive and specific radiopharmaceuticals for *E. coli* detection include [^{18}F]-fluoromaltose and [^{18}F]-FAG [421,422]. When using both Gram-positive and Gram-negative bacteria or a combination of bacteria to induce infection in the preclinical models, [^{18}F]-

MIM Software Inc. v. Progenics Pharmaceuticals, Inc.
IPR2025-00630
Progenics EX2017

fluoropropyl-trimethoprim, [^{18}F]-fluoromaltose, and other fluorine-labeled analogues showed good specificity for bacterial infection imaging with possible applicability in clinics [423–425]. Although [^{68}Ga]-gallium-DOTA-TBIA101 is also considered a promising agent for *E. coli* infection [426], when the infection is being induced by *S. aureus* or *M. tuberculosis*, this radiopharmaceutical was found to be nonspecific [427].

2.1.5. PET Radiopharmaceuticals for Infection/Inflammation

Inflammation is associated with a variety of human diseases, including stroke, Alzheimer's disease, atherosclerosis, autoimmune diseases, and even malignant conditions, either directly or indirectly. As a result, information gleaned from molecular imaging of inflammation in various conditions is extremely useful for disease diagnosis and prognosis, therapeutic response monitoring, and better understanding disease processes. Many inflammation-related biomarkers, such as inflammatory cell metabolism, membrane markers, cytokines, and vascular alterations during inflammation, have been discovered and explored for potential imaging or therapeutic targets thus far. However, not many such radiopharmaceuticals have been developed in recent years.

In both physiological and pathological settings, B cells are essential for controlling immunological responses. The deregulation of B-cell function is assumed to be the cause of a number of B-cell-mediated illnesses, such as B-cell malignancies (e.g., lymphomas, leukemia) [428], autoimmune disorders (e.g., rheumatoid arthritis (RA)) [429], multiple sclerosis (MS) [430–432], inflammatory illnesses (e.g., obesity, diabetes [433,434]), and transplant complications [435]. Thus, B cells are a very important therapeutic target. BTK is a cytoplasmic tyrosine kinase that is expressed by both B cells and myeloid cells such as microglia. The kinase is implicated in various signal transduction pathways that are important in B-cell development [436]. BTK inhibitors are being studied for the treatment of B-cell malignancies [437], but also in order to combat inflammatory and autoimmune illnesses [438], such as RA [439] and MS [440]. Radiolabeling BTK inhibitors and using the resulting radiopharmaceuticals in PET imaging will be extremely beneficial in the monitoring and treatment of B-cell-mediated diseases.

Donnelly et al. proposed the syntheses of such radiopharmaceuticals, using carbon-11 isotopes, due to their optimal half-life of 20 min. By the end of the study, one of the radiopharmaceuticals presented encouraging prospects as a novel PET tracer. [^{11}C]-ibrutinib presented >98% radiochemical purity and molar activity of 7.6 $\pm$ 2.7 Ci/µmol (281 $\pm$ 99 Gbq/µmol) and with a half-life ranging from 19.89 to 20.15 min. Moreover, quality control tests revealed that this radiopharmaceutical is sterile [441].

In peripheral tissues, TSPO is widely expressed, but in the healthy human brain, it is only moderately expressed. TSPO expression was shown to be high in macrophages, neutrophils, lymphocytes [352,442], activated microglia, and astrocytes in previous research [443,444]. Most investigated radiotracers used in PET imaging are either ^{11}C or ^{18}F labeled. Examples of such tracers that bind to TSPO are: ^{11}C or ^{18}F-labeled isoquinoline carboxamide PK11195 (1-(2-chlorophenyl)-*N*-methyl-*N*-(1-methylpropyl)-3-isoquinoline carboxamide) [352] and, more recently, ^{11}C-PBR28 (*N*-(2-[^{11}C]-methoxybenzyl)-*N*-(4-phenoxypyridin-3-yl)acetamide) [443,445]. Moreover, it has been found that in rat models, TSPO ligands were able to accumulate in infarct areas. Furthermore, PET imaging using TSPO has also been reported to have shown promising results in atherosclerosis detection, ^{3}H-DAA1106 ((*N*-5-fluoro-2-phenoxyphenyl)-*N*-(2,5-dimethoxybenzyl)acetamide), ^{3}H-(R)-PK11195, and ^{11}C-PK11195 being such examples [352]. PET imaging using the TSPO radio-ligands ^{18}F-FEDAC, ^{11}C-(R)-PK11195 41, and ^{123}I-(R)-PK11195 57 revealed considerable lung lesion absorption, mostly from active neutrophils and macrophages, in a lipopolysaccharide-induced infectious lung inflammation model [442].

The somatostatin receptor (SSTR) has been taken into account for neuroendocrine tumor imaging. However, very few PET tracers have been reported to target SSTR, but it has been deemed more successful in SPECT imaging [446].

MIM Software Inc. v. Progenics Pharmaceuticals, Inc.
IPR2025-00630
Progenics EX2017

MMPs are zinc- and calcium-dependent metalloproteases that may destroy extracellular matrix (ECM) protein components. MMPs and their inhibitors, MMPIs, regulate the balance of extracellular proteolysis, and increased MMP activity is linked to cancer, atherosclerosis, and other inflammatory diseases. In a separate investigation [402], ApoE-/- mice with a high-cholesterol diet were given ^{18}F-MMPI. MMP-positive plaques may be seen in the aorta's inner curvature using ex vivo PET/CT.

Interleukin-2 (IL-2) is a 133-amino-acid single-chain glycoprotein produced and released by activated T cells, particularly CD4^{+} and CD8^{+} Th1 lymphocytes. Many forms of inflammatory disorders, such as inflammatory degenerative diseases, transplant rejection, tumor inflammation, organ-specific autoimmune diseases, and adipose inflammatory insulin resistance, are associated with T-cell activation. Di Gialleonardo et al. described the production of ^{18}F-FB-IL-2 by tagging IL-2 with *N*-succinimidyl 4-^{18}F-fluorobenzoate (^{18}F-SFB) to identify activated T cells in inflammation [401]. These preliminary findings imply that ^{18}F-FB-IL-2 is stable, physiologically active, and capable of detecting activated T cells in vivo [447].

VCAM-1, a member of the immunoglobulin superfamily of endothelial adhesion molecules, is a vascular cell adhesion molecule. It is crucial in all phases of atherosclerotic plaque formation [448]. It is found on active endothelium and can cause macrophage adherence in the early stages of plaque development. VHPKQHR, a linear peptide affinity ligand, was discovered in apolipoprotein E-deficient mice utilizing in vivo phage display. This peptide is similar to very late antigen-4, a known VCAM-1 ligand. Based on this peptide sequence, a multivalent PET imaging agent (^{18}F-4V) was created and used to assess VCAM-1 expression. PET imaging of atherosclerotic plaques in the aortic root in (ApoE)-/- mice revealed a large focused signal in the aortic root [448].

The [^{18}F]-FDG was found to be the most suitable radiopharmaceutical for infectious and inflammatory diseases. For fungal infections, this radiotracer showed promising results by detecting pathophysiological changes in earlier stages and being able to image infectious foci. Moreover, [^{18}F]-FDG is a good candidate for biopsy, as it is able to detect most active infection sites. Studies also confirmed that this radiopharmaceutical is suitable for treatment monitoring and regulation [449–451]. It has been also reported that [^{18}F]-FDG has a great impact on large vessel vasculitis (LVV) imaging and treatment recommendations. Specifically, a study reported a 26.7% change in the treatment of patients with LVV who did not receive immunosuppressive medication and a 22.6% change of treatment in those who received medication [452]. In order to prevent younger patients' exposure to radiation, [^{18}F]-FDG-PET/MRI showed great feasibility in LVV detection in preliminary results; however, further research must be conducted in order to confirm its efficacy [453].

Current applications of FDG-PET include bloodstream infections of unknown origins, fever of unknown origins, infective endocarditis, vascular graft infections, spondylodiscitis, and cyst infections [454]. Another research article suggested that [^{18}F]-FDG is better for monitoring the disease during immunosuppressive therapy. However, when it comes to imaging an immunological network in cancer, [^{18}F]-FDG is not suitable, particularly in the early phases of the treatment. The radiopharmaceutical targets the tumor cells as well as inflammatory cells; thus [^{18}F]-FDG might show an increase in metabolic burden due to the fact that immunotherapeutic drugs present an inflammatory response. Other studies also confirmed the [^{18}F]-FDG tracer's inability to differentiate from pseudo-progression and when a patient should cut off therapy [455,456].

The [^{64}Cu]-GTSM is widely used for imaging inflammation using cell migration trafficking [457] and expected to be more suitable than [^{64}Cu]-PTSM. Moreover, in a review article published in 2019, Werry et al. presented an overview of recent developments in TSPO-dependent PET imaging biomarkers for neuroinflammation in neurodegenerative disorders [458]. The inflammatory responses in the brain and spinal cord are known to promote the activation of microglia and astrocytes, and represent a pathological hallmark in many central nervous system diseases. A direct correlation between activated microglia, inflammatory cytokines, and TSPO ligand bindings has been demonstrated

MIM Software Inc. v. Progenics Pharmaceuticals, Inc.
IPR2025-00630
Progenics EX2017

in neurodegenerative patterns of animal models; therefore, increased TSPO PET signals may occur in disease-relevant brain regions within a large variety of neurodegenerative disorders [458,459]. For monitoring this type of inflammations in neurodegenerative diseases, [^{11}C]-PK11195 [460,461], [^{11}C]-ER176 [460,462], [^{18}F]-GE-180 [463–470], [^{11}C]-DPA-713 [460,465], [^{18}F]-DPA-713 [471], [^{11}C]-PBR-28 [460,462,472–479], [^{18}F]-PBR111 [480,481], [^{18}F]-FEDAA1106 [482,483], and [^{11}C]-DAA1106 [484] radiotracers have been investigated.

2.1.6. Novel PET Tracers in Oncology and PET Radiopharmaceuticals with Proven Use in Clinical Practice

In oncology, several studies reported novel radiotracers for PET imaging. For example, an ^{18}F-labeled tropomyosin receptor kinase (TRK) inhibitor, [^{18}F]-TRACK, was described by Gauthier et al. Overexpression of the TRK A, B, or C receptors leads to tumor development, metastasis, and neurological disorders, such as Alzheimer's and Parkinson's. In experiments with nonhuman primates, [^{18}F]-(R)-TRACK was observed to pass the BBB and demonstrated high brain uptake [485]. Mossine et al. described an ^{18}F-labeled sulfonamide analogue as a human carbonic anhydrase IX inhibitor for PET imaging of hypoxic tumors [486].

Song et al. used ^{18}F-IRS as an EGF-specific ligand to image mutant EGF receptors in patients with NSCLC. Overproduction of EGF receptor ligands in the tumor microenvironment causes severe EGFR receptor alterations, which speed up epithelial tumor cell proliferation, invasion, and metastasis [487,488]. In vivo, this radiotracer exhibited excellent tumor cell absorption by targeting mutant EGF receptors.

Several studies have demonstrated the overexpression of TSPO in gliomas, and a recent research, conducted by Su et al., found that using the [^{11}C]-PK11195 radiotracer, low-grade astrocytomas and oligodendrogliomas may be clearly distinguished using a PET dynamic analysis [489]. PET molecular imaging studies with endogenous reporter genes have been translated into clinical research, and one recent study with trimethoprim labeled with carbon-11 ([^{11}C]-TMP) in a xenograft mouse model showed high biodistribution and good sensitivity toward *Escherichia coli* dihydrofolate reductase expressing cells, implying that it could provide advancement in current PET reporter gene technologies [490].

Since the absorption of [^{18}F]-fluciclovine in prostate cancer cells was shown to be high in patients with recurrent prostate cancer [491], [^{18}F]-fluciclovine, also known as Axumin, has been authorized by the US Food and Drug Administration (FDA) for clinical use. Another novel ^{18}F-labeled tracer was reported by Strebl et al. Their work revealed significant brain uptake, specific binding, and regional distribution of the novel radiotracer [^{18}F]-MGS3 for PET imaging of histone deacetylase in humans [492]. Moreover, among other tracers with clinical approval, a transgenic mouse model of breast cancer study revealed encouraging findings using [^{11}C]-PAQ to monitor the cancer treatment status and was deemed a a good radiotracer in cancer therapy response treatment [493]. Last but not least, the [^{11}C]-4DST (4′-[methyl-11C]-thiothymidine) compound, a thymidine derivative, has also been authorized for clinical use, particularly for the assessment of cancerous cell development, metastasis, and invasion [494,495].

2.2. SPECT Radiopharmaceuticals

The ^{99m}Tc is a pure gamma emitter radionuclide with a half-life of 6 h. It decays into ^{99}Tc by isomeric transition (140.5 keV 98.6% and 142.6 keV 1.4%). It is readily available from ^{99}Mo/^{99m}Tc generators and is extracted as a [^{99m}Tc(VII)]-O_4 solution. The physical properties for ^{99m}Tc are close to ideal for SPECT and planar scintigraphy imaging: the 140.5 keV photon energy is optimal for gamma cameras, being a pure gamma emitter ensures no additional radiation burden to the patient, and the versatility of ^{99m}Tc chemistry allows for the development of a multitude of easy-to-prepare compounds through the introduction of cold labeling kits. Technetium-labeled radiopharmaceuticals are the most used imaging agents in nuclear medicine worldwide and cover a wide range of applications:

MIM Software Inc. v. Progenics Pharmaceuticals, Inc.
IPR2025-00630
Progenics EX2017

thyroid, bone, renal, myocardial perfusion, intestinal, cerebral, hepatic, cerebral imaging, and so forth [9,496,497].

In the last decade, a large number of studies were devoted to technetium chemistry and developing new radiopharmaceuticals; however, the imaging capabilities of SPECT systems in terms of sensitivity and resolution were outperformed by PET/CT. While the 1990s and 2000s saw a significant number of new radiopharmaceuticals transitioning to clinical practice, in the last decade, just a few passed the clinical trials. Nevertheless, the last years saw a renewed interest in SPECT imaging through the introduction of CZT detector technology, more specialized dedicated systems, and advances in image reconstruction and quantification [498–503].

Modern technetium-labeled radiopharmaceuticals are developed through indirect labeling using bifunctional chelators. An important aspect of this method is finding the ideal chelator to incorporate the radiometal and link it to the pharmacophore. An interesting feature of ^{99m}Tc is the formation of characteristic moieties that dictate the chemical properties of the resulting complexes. Examples of technetium cores used in the development of promising compounds are [^{99m}Tc(I)]-tricarbonyl, [^{99m}Tc(V)]-HYNIC, and [^{99m}Tc(V)]-nitrido [10]. To this end, a large body of work was directed to the synthesis and structural and chemical characterization of bifunctional chelating agents for technetium.

2.2.1. SPECT Radiopharmaceuticals in Oncology

SPECT imaging in clinical oncology plays an important role in identifying various tumors overexpressing particular receptors. Radiopharmaceuticals have been successfully developed for imaging of somatostatin receptors (neuroendocrine, gastroenteropancreatic, breast, brain, and small cell lung cancer tumors), prostate-specific membrane antigen (prostate cancer), gastrin-releasing peptide receptor (prostate, breast, pancreas, small cell lung cancer, and colorectal tumors), melanocortin 1 receptor (melanomas), and integrin $\alpha_v\beta_3$ receptor (brain, lung, ovary, breast, and skin cancer), to name a few [504].

SSTR-targeting Tc-labeled radiopharmaceuticals were the first to be developed. The first commercially available agent was [^{99m}Tc(V)]-EDDA-HYNIC-TOC, consisting of a [^{99m}Tc(V)]-HYNIC core, EDDA as coligand, and Tyr3-octreotide as an SSTR agonist peptide [10,505]. Studies showed good specificity and sensitivity and performed similarly in a direct comparison with [^{111}In]-DTPA-octreotide. The [^{99m}Tc(V)]-HYNIC/EDDA-TOC is a reasonable alternative, the main advantages being related to the superior physical properties of [^{99m}Tc] as an imaging agent [506].

The choice of agonist peptides as pharmacophores was natural, considering the increase in tumor uptake due to internalization; however, it was determined that RFs with peptide antagonists had higher uptake most likely due to the fact that antagonists bind to multiple sites, increasing radiopharmaceutical retention [10]. Makris et al. developed a series of compounds using the tricarbonyl core and NOTA and NODAGA as chelators, conjugated to a SSTR type 2 antagonist peptide. Structural characterization was performed on the Re analogues by means of LC-ESIMS, HR-ESI-MS, and NMR spectroscopy. Radiolabeling resulted in high yields (>95%) determined by HPLC, and both were stable in rat serum with a protein binding of 9%–24% [507]. In the preclinical studies, biodistribution and SPECT imaging were evaluated in AR42J tumor-bearing ICR SCID mice. [^{99m}Tc(I)]-NOTA revealed significantly higher tumor uptake than [^{99m}Tc]-NODAGA, 16.7 $\pm$ 3.32%ID/g compared with 2.78 $\pm$ 0.27%ID/g. Both complexes had medium to low tumor retention, rapid renal clearance, and tumor accumulation, which could clearly be identified on SPECT/CT images in accordance with biodistribution data [508].

Another recent study [509] compared two ^{99m}Tc radiolabeled somatostatin receptor antagonists based on a new peptide, SS-01 (p-Cl-Phe-cyclo(D-Cys-Tyr-D-Trp-Lys-Thr-Cys)D-Tyr-Nh2), using the HYNIC and tetraamine chelators. Preclinical evaluation revealed a better performance from the tetraamine compound [^{99m}Tc(V)]-N4-SS-01 with a very high tumor uptake of 47%/IA/g and rapid clearance from nonspecific organs, resulting in high-contrast SPECT/CT images, while the HYNIC compound exhibited almost no uptake

MIM Software Inc. v. Progenics Pharmaceuticals, Inc.
IPR2025-00630
Progenics EX2017

in vitro. As a follow-up, Fani et al. [510] evaluated two [^{99m}Tc(V)]-tetraamine sst2 antagonists: TECANT-1 based on an LM3 structure and TECANT-2 based on the SS-01 peptide. The preclinical results in HEK-SST2-bearing mice revealed similar uptake and stability. TECANT-1 had lower uptake in blood, kidney, and muscles, providing the best tumor to background ratios, and was selected for clinical translation. Although the [^{99m}Tc(V)]-tetraamine compounds performed better, Gaonkar et al. [511] investigated why the Tc-HYNIC fragment lost tumor cell uptake when conjugated with the SS-01 antagonist peptide. They evaluated the effects of spacers of different lengths on [^{99m}Tc(V)]-HYNIC/EDDA conjugated with the potent antagonist peptides SS-01 and JR11 in a head-to-head comparison with [^{99m}Tc(V)]-N4-SS-01 and [^{99m}Tc(V)]-N4-JR11, with the commercially available [^{99m}Tc(V)]-HYNIC/EDDA-TOC as reference. In vitro studies determined that introducing the spacer increased cellular uptake depending on the spacer's length. The best uptake was found for the Ahx (C_6 amino-hexanoic acid) spacer with a 16-fold increase compared with [^{99m}Tc(V)]-HYNIC/EDDA-SS-01, nearly on the same level as the reference. Further biodistribution and SPECT/CT studies of [^{99m}Tc(V)]-HYNIC/EDDA-Ahx-SS-01 and [^{99m}Tc(V)]-HYNIC/EDDA-Ahx-JR11 in HEK-SST2-tumor-bearing mice revealed a similar picture. Although tumor uptake was still higher for the N4 conjugates, they also exhibited increased uptake in the kidneys and higher background activity. This, in turn, resulted in higher contrast SPECT/CT images for the HYNIC conjugates.

PSMA has become the primary focus of targeted imaging and therapy in prostate cancer. A great number of PSMA inhibitor small-molecule imaging agents have been developed for both SPECT/CT and PET/CT [10,512,513]. The most representative are [^{123}I]-MIP-1072, [^{99m}Tc(I)]-MIP-1404, [^{99m}Tc(V)]-HYNIC-iPSMA, and [^{99m}Tc(V)]-O-N_3S-PSMA I&S.

The [^{123}I]-MIP-1072 and ^{123}I-MIP-1095 based on the Glu-urea-Lys motif were the first to gain clinical attention. Preclinical results showed higher tumor uptake for MIP-1072 at 1 h postinjection and higher uptake for MIP-1095 at 24 h postinjection. Based on these results MIP-1072 was further evaluated as an imaging agent for SPECT/CT clinical studies, while MIP-1095 was proposed as a therapeutic agent labeled with $^{125/131}$I due to higher tumor retention [514–516].

Hillier et al. [517] evaluated four technetium-labeled PSMA inhibitors based on the [^{99m}Tc(I)] $(CO)_3^+$ core and Glu-urea-Glu and Glu-urea-Lys pharmacophores conjugated to CIM or TIM chelators. Out of the four, [^{99m}Tc(I)]-MIP-1404 showed the most promising results. In phase I and II clinical trials, the compound successfully identified small lesions in the prostate gland, lymph nodes, and bones [517,518]. However, it failed the specificity coprimary endpoint of a phase III clinical trial, detecting clinically meaningful prostate cancer with a specificity of 71–75% [513].

Promising results using the [^{99m}Tc(V)]-HYNIC core were obtained for [^{99m}Tc(V)]-HYNIC/EDDA-iPSMA and [^{99m}Tc(V)]-HYNIC/EDDA-ALUG [519–523]. The [^{99m}Tc(V)]-HYNIC/EDDA-ALUG showed good binding affinity to PSMA-positive LNCaP cells and small animal imaging of mice bearing LNCaP tumor xenographs [519]. The [^{99m}Tc(V)]-HYNIC/EDDA-iPSMA composed of a ligand incorporating the Lys(NaI)-urea-Glu inhibitor was synthesized through kit formulation with high yield and no need for further purification. Results showed high tumor uptake, mainly kidney excretion, with preliminary SPECT/CT images able to detect tumors and metastasis in patients with prostate cancer [520,521]. Follow-up studies [522,523] evaluated the performance of [^{99m}Tc(V)]-HYNIC/EDDA-iPSMA SPECT/CT in comparison with [^{68}Ga]-PSMA-11 PET/CT images based on maximal standardized uptake values on prostate, bone lesions, and lymph nodes. The authors found the performance of [^{99m}Tc(V)-HYNIC/EDDA-iPSMA comparable to that of [^{68}Ga]-PSMA-11 for prostate and bone lesions and for lymph nodes with a size greater that 10 mm; however, the technetium compound had lower sensitivity for small lesions, detecting only 28% of the nodes with a size of less than 10 mm, identified by the PET scan. This can be attributed to the lower sensibility and resolution of SPECT systems and the technical difficulty in SPECT SUV calibrations.

MIM Software Inc. v. Progenics Pharmaceuticals, Inc.
IPR2025-00630
Progenics EX2017

The [^{99m}Tc(V)]-O-N_3S-PSMA-I&S [524,525] was designed for radio-guided surgery. The [Tc(V)≡O]$^{3+}$ core was coordinated to a mercaptoacetyl-trisine chelator coupled to the PSMA targeting pharmacophore. Biodistribution studies in patients showed slow clearance, which allowed imaging at 3-5 h after injection for visualization of PSMA-rich lesions. Various hospitals implemented protocols for radio-guided surgery and reported successful intraoperative detection and removal of metastatic lesions.

A different method for PSMA receptor targeting is based on utilizing radiolabeled nanobodies. Nanobodies are fragments of antibodies that retain certain binding properties and exhibit faster pharmacokinetics than the original structure [526].

Evazalipour et al. [527] developed a series of technetium-labeled anti-PSMA nanobodies. The two most promising compounds, [^{99m}Tc(I)]-PSMA30 and [^{99m}Tc(I)]-PSMA6, showed specific binding affinity for LNCaP but not PC3 cells. PSMA30 had better tumor uptake and tumor-to-normal-organ ratio and was chosen for further investigations.

Several novel $\alpha_v\beta_3$-targeting SPECT imaging agents have been developed based on the RGD motif (arginyl-glycyl-aspartic acid). However, so far, none have been introduced in clinical practice. The [^{99m}Tc]-maraciclatide ([^{99m}Tc]-NC100692) is a cyclic peptide conjugated to the RGD motif initially evaluated in breast and lung cancer. Recently, Cook et al. [528] investigated the potential of [^{99m}Tc]-maraciclatide in the detection and therapy response assessment in patients with prostate cancer. They successfully demonstrated that 99mTc-maraciclatide specifically accumulates in metastatic bone lesions in patients with prostate cancer. Furthermore, based on measurements of CT Hounsfield units, they determined a possible relation between the uptake and the degree of osteoclast activity.

The [^{99m}Tc(V)]-3P4-RGD2 [529–532], a promising compound based on a HYNIC chelator, PEG4 linkers, and RGD2 peptide, showed good pharmacokinetic properties. Clinical investigations showed good results for the detection of malignant lesions in pulmonary cancer [529] and bone metastasis [533]. Two other studies comparing [^{99m}Tc(V)]-3P4-RGD2 with [^{99m}Tc(I)]-sestamibi scintimammography revealed that [^{99m}Tc(V)]-3P4-RGD2 had slightly better performance in sensitivity, specificity, and accuracy, but it was not statistically significant [530,531]. Two other prospective studies performed comparison studies of [^{99m}Tc(V)]-3PRGD2 with [^{18}F]-FDG in breast cancer [534] and esophageal cancer [535] showing comparable results between the two compounds, highlighting the potential of this technetium radiopharmaceutical.

2.2.2. SPECT Radiopharmaceuticals for Cardiovascular Events

Similarly to PET radiotracers, myocardial perfusion imaging with SPECT plays a pivotal role in cardiology, predominantly in the diagnosis and risk assessment of coronary artery disease (CAD). There are three SPECT imaging agents currently in clinical use: [^{201}Tl]-Cl, [^{99m}Tc(I)]-sestamibi, and [^{99m}Tc(V)]-tetrofosmin. The [^{201}Tl]-Cl is used less than the Tc analogues due to limitations regarding long half-life, attenuation artifacts produced by the low characteristic X-ray emission in the range of 69 to 81 keV, and administered dose constraints due to radiation burden [536].

The [^{99m}Tc(I)]-sestamibi is a lipophilic cation consisting of a technetium core bound to six 2-methoxyisobutylisonitrile (MIBI) ligands. Given the importance of this radiopharmaceutical, we previously reported a detailed structural characterization of the MIBI ligand by means of vibrational spectroscopy and density functional theory calculations [537]. The [^{99m}Tc(V)]–tetrofosmin consists of a di-oxo core bound to two diphosphine ligands. Both compounds benefit from easy cold kit preparation and were developed in the 1980s. The two tracers perform similarly with some differences regarding extraction coefficient, heart uptake, blood and liver washout, and optimal time of imaging from injection [538].

In a comprehensive review conducted by Boschi et al. [539], the authors highlight the fact that despite the extensive use of these compounds in nuclear cardiology for decades, they do not meet the requirements of an ideal perfusion imaging agent. The main disadvantages are low first-pass extraction, high liver absorption which can hinder the interpretation

MIM Software Inc. v. Progenics Pharmaceuticals, Inc.
IPR2025-00630
Progenics EX2017

of the lower and left ventricular wall, and lack of a linear relationship between uptake and coronary blood flow.

Promising imaging agents were developed based on the [^{99m}Tc][Tc(V)N(L)(PNP)]$^{+}$ scaffold consisting of the [^{99m}Tc]-nitride core [^{99m}Tc(V)≡N]$^{2+}$, a PNP-type bis-phosphine, and one monoanionic chelate (L) [540]. Biodistribution studies of [^{99m}Tc(V)]-N-MPO, consisting of a [^{99m}Tc(V)≡N]$^{2+}$ core with 2-mercaptopyridine and biphosphine as chelators, showed higher myocardial uptake than [^{99m}Tc(I)]-sestamibi and very fast liver clearance. Clinical studies showed favorable results. Due to the fast liver washout, the myocardium was clearly separated from the left liver lobe on images acquired at 10 min after injection, making [^{99m}Tc(V)]-N-MPO a good candidate for imaging patients with known CAD [541].

In a more recent study, Salvarese et al. [542] evaluated a new class of complexes of the general formula [^{99m}Tc][Tc(V)N(DASD)(PNP*n*)]$^{+}$, where DASD = 1,4-dioxa-8-azspiro[4,5]-decandithiocarbamate and PNP*n* = bisphosphinoamine. The compounds are modified versions of the [^{99m}Tc(V)]-N-DBODC(5) complex, which showed comparable results to commercially available agents in clinical studies. Animal studies showed increased myocardial uptake and superior heart-to-liver ratios for two of the four compounds investigated when compared with [^{99m}Tc(V)]-N-DBODC(5), [^{99m}Tc(I)]-sestamibi, and [^{99m}Tc(V)]-tetrofosmin.

The [^{99m}Tc(III)]-teboroxime is one of the first approved tracers for cardiac imaging. It has excellent pharmacokinetic properties: high first pass extraction, linear relation between uptake and blood flow and rapid clearance [543–545]. The main drawback of this tracer is the very fast cardiac washout that leaves a 5 min window for image acquisition, which is difficult to achieve on conventional gamma cameras. A new class of [^{99m}Tc(III)] derivatives was developed [546–548] similar in structure to teboroxime except for the replacement of the methyl group added to the boronate cap by a sulfonyl group. As a follow-up, Xi et al. [549] performed a comparative study on normal and acute myocardial infarction swine between [^{99m}Tc(III)]-3SPboroxime and [^{99m}Tc(I)]-sestamibi. The results showed high initial heart uptake, longer myocardial retention, and high heart-to-background ratio. These results make [^{99m}Tc(III)]-3SPboroxime an excellent candidate for future clinical studies.

2.2.3. SPECT Radiopharmaceuticals in Neurological Disorders

The most commonly used SPECT imaging agents in neurology are [^{99m}Tc(V)]-HMPAO, [^{123}I]-ioflupane. and [^{99m}Tc(I)]-TRODAT-1. The [^{99m}Tc(V)]-HMPAO ([^{99m}Tc(V)]-exametazime) is regularly used for the assessment of cerebral perfusion in neurological diseases [550,551]. [^{123}I]-ioflupane and [^{99m}Tc(I)]-TRODAT-1 bind to the presynaptic dopamine transporter to give images of the striatum. They are useful in the diagnosis of Parkinson's disease, which can be evaluated by the asymmetric or degraded uptake in the two striata. Although the preparation of [^{99m}Tc(I)]-TRODAT-1 is more convenient, its brain uptake is lower than that of [^{123}I]-ioflupane [550].

Promising ^{123}I-based tracers have been developed for beta-amyloid imaging. Chen et al. developed a series of imidazopyridine compounds [552]. The most successful compound based on brain permeability, rapid nonspecific organ washout, and affinity to Aβ aggregate, termed DRM106 (6-iodo-2-[4-(1H-3-pyrazolyl)phenyl]imidazole[1,2-α]pyridine), was further evaluated in vivo. Results showed that the performance of the trace is comparable to that of [^{11}C]-PiB in detecting Aβ deposition. In 2016, Maya et al. [553] evaluated a novel tracer, [^{123}I]-I-ABC577, in preclinical and clinical studies. The results revealed favorable pharmacokinetics, and SPECT imaging was able to differentiate Alzheimer's disease patients from normal controls.

One of the limiting factors of designing technetium radiopharmaceuticals for neurological applications is their poor ability to cross the blood–brain barrier. Many different compounds have been designed that bind to Aβ plaques, but they do not mark all the checks required to pass the barrier [554].

Sangou et al. [555] reported novel technetium/rhenium derivatives of benzothiazole, benzimidazole, and *N*-methylbenzimidazole that demonstrated affinity for Aβ plaques and impressive brain uptake. The structures of the compounds were obtained by replacing

MIM Software Inc. v. Progenics Pharmaceuticals, Inc.
IPR2025-00630
Progenics EX2017

the phenyl moiety of 2-phenylbenzothiazole with the cyclopentadienyl tricarbonyl core $[Cp^{99m}Tc(I)(CO)_3]^+$. The 2-arylbenzothiazole scaffold has been extensively used as a pharmacophore for Aβ plaques, and the $[Cp^{99m}Tc(I)(CO)_3]^+$ possesses favorable properties for BBB penetration. The Re complexes were characterized by IR, NMR, MS-ESI, and elemental analysis. X-ray crystallography was possible for the Re benzothiazole derivative. Spectroscopic analysis revealed a piano-stool-type structure. The [^{99m}Tc] derivatives obtained were stable with high radiolabeling yield and retained binding affinity for Aβ plaques and showed impressive brain uptake of 7.94 ± 1.46, 3.99 ± 0.6, and 5.36 ± 0.65%IA/g at 2 min postinjection. Overall, these tracers show remarkable properties for Aβ imaging [555].

3. Materials and Methods

A literature research was conducted within scientific databases, including PubMed, Scopus, and Web of Science, and random google searches. Our interest focuses on articles and/or review papers published in the last 10 years. Two authors screened and selected (independently) the studies related to the herein presented topics on PET, and two authors were (independently) focused on the literature related to radiopharmaceuticals used for SPECT scans.

All searches were based on multiple combinations of the following keywords: "PET/CT" OR "positron emission tomography/computed tomography", "radionuclide", "radiopharmaceuticals", "ligands" OR "radioligand", "PET tracers", "oncology", "overview", "SPECT/CT" OR "single photon emission computed tomography/computed tomography, "Technetium radiopharmaceuticals", "SPECT radiopharmaceuticals", "myocardial perfusion imaging", and "structural characterization".

For the studies reported in this review article, the authors considered gathering the required information within the following parameters: author, year of publication, articles' DOI (for an easier access to the articles of interest), title, radionuclide, half-life, compound, disease, uptake localization, function, standard/new, key aspects, short abstract, and conclusions.

Moreover, in order to complete the herein final list of references, the authors also considered the reference lists of the primary and relevant studies.

4. Conclusions

4.1. PET Radiopharmaceuticals

Based on our findings within the available literature, there are encouraging results that suggest great development in the radiopharmaceutical industry for PET imaging. Among the most effective PET tracers with a wide range of applications are the ^{18}F- and ^{11}C-labeled radiopharmaceuticals due to their convenient half-life. Although there are few tracers developed in the past 10 years regarding inflammatory diseases, many novel tracers have been released to clinical use and subjected to oncological and neurological pathologies. Moreover, many tracers have shown great preliminary results, and even though further research is needed for their validation and commercialization, the prospects are promising.

4.2. SPECT Radiopharmaceuticals

Significant effort has made in researching novel SPECT radiopharmaceuticals, with limiting results, especially in comparison with PET tracers. The few that were evaluated in clinical trials were found to be statistically similar to currently used first-generation radiopharmaceuticals. Due to advances in the chemistry of bifunctional chelators and the versatility of [^{99m}Tc] metal fragments, promising results have been published in more recent literature. The bulk of the research has focused on peptide receptor targeting radiopharmaceuticals for tumor imaging, specifically for SSTR and PSMA targeting. Compounds with favorable pharmacokinetics were obtained using a variety of ligands, most notably NOTA/NODAGA, HYNIC, and tetramine, which were successfully conjugated to relevant peptides, all showing good tumor uptake and tumor-to-background ratios in preclinical evaluations.

MIM Software Inc. v. Progenics Pharmaceuticals, Inc.
IPR2025-00630
Progenics EX2017

Moreover, advances in SPECT detector design demonstrating higher resolution, sensitivity, and faster acquisition times have renewed interest in older radiopharmaceuticals, such as [^{99m}Tc(III)]-teboroxime, prompting the development of new derivatives with excellent potential for myocardial perfusion imaging. Although the preclinical results are promising, further clinical studies are needed for the validation of biodistribution data and imaging capabilities in human patients for these novel compounds. Nevertheless, we conclude that SPECT radiopharmaceuticals still play a significant role in molecular imaging as a complementary technique to PET imaging.

Supplementary Materials: The following supporting information can be downloaded at: https://www.mdpi.com/article/10.3390/ijms23095023/s1.

Author Contributions: Conceptualization, V.C., G.A. and C.C.; methodology, V.C., G.A., G.C. and N.S.M.-C.; investigation, G.C., N.S.M.-C. and D.-G.T.; data curation, G.C., N.S.M.-C. and V.C.; writing—original draft preparation, N.S.M.-C., G.C., D.-G.T. and V.C.; writing—review and editing, N.S.M.-C., G.C. and V.C.; supervision, V.C., G.A. and C.C.; project administration, V.C.; funding acquisition, V.C. All authors have read and agreed to the published version of the manuscript.

Funding: This research was funded by CNCS/CCCDI UEFISCDI, project number PN-III-P4-ID-PCCF-2016-0112.

Institutional Review Board Statement: Not applicable.

Informed Consent Statement: Not applicable.

Data Availability Statement: No new data were created or analyzed in this study. Data sharing is not applicable to this article.

Acknowledgments: The research undertaken for this article was conducted using the Babeș-Bolyai University Research infrastructure financed through the project MADECIP (POSCEE COD SMIS CSNR 48801/1862). D.-G. Timaru acknowledges financial support from the World Federation of Scientists, CERN, Geneva.

Conflicts of Interest: The authors declare no conflict of interest.

References

1. Cuocolo, A.; Petretta, M. PET and SPECT Specialty Grand Challenge. When Knowledge Travels at the Speed of Light, Photons Take to the Field. *Front. Nucl. Med.* **2021**, *1*, 671914. [CrossRef]
2. Van der Meulen, N.P.; Strobel, K.; Lima, T.V.M. New Radionuclides and Technological Advances in SPECT and PET Scanners. *Cancers* **2021**, *13*, 6183. [CrossRef] [PubMed]
3. Wadsak, W.; Mitterhauser, M. Basics and principles of radiopharmaceuticals for PET/CT. *Eur. J. Radiol.* **2010**, *73*, 461–469. [CrossRef] [PubMed]
4. Lau, J.; Rousseau, E.; Kwon, D.; Lin, K.S.; Bénard, F.; Chen, X. Insight into the Development of PET Radiopharmaceuticals for Oncology. *Cancers* **2020**, *12*, 1312. [CrossRef]
5. Lee, Y.S. Radiopharmaceuticals for Molecular Imaging. *Open Nucl. Med. J.* **2010**, *2*, 178–185. [CrossRef]
6. Kuna, M.; Mahdi, F.; Chade, A.R.; Bidwell, G.L., III. Molecular Size Modulates Pharmacokinetics, Biodistribution, and Renal Deposition of the Drug Delivery Biopolymer Elastin-like Polypeptide. *Sci. Rep.* **2018**, *8*, 7923. [CrossRef]
7. Waterhouse, R.N. Determination of lipophilicity and its use as a predictor of blood-brain barrier penetration of molecular imaging agents. *Mol. Imaging Biol.* **2003**, *5*, 376–389. [CrossRef]
8. Kratochwil, N.A.; Huber, W.; Muller, F.; Kansy, M.; Gerber, P.R. Predicting plasma protein binding of drugs: A new approach. *Biochem. Pharmacol.* **2002**, *64*, 1355–1374. [CrossRef]
9. Israel, O.; Pellet, O.; Biassoni, L.; De Palma, D.; Estrada-Lobato, E.; Gnanasegaran, G.; Kuwert, T.; la Fougère, C.; Mariani, G.; Massalha, S.; et al. Two decades of SPECT/CT—The coming of age of a technology: An updated review of literature. *Eur. J. Nucl. Med. Mol. Imaging* **2019**, *46*, 1990–2012. [CrossRef]
10. Duatti, A. Review on ^{99m} Tc radiopharmaceuticals with emphasis on new advancements. *Nucl. Med. Biol.* **2021**, *92*, 202–216. [CrossRef]
11. Fahey, F.; Stabin, M. Dose optimization in nuclear medicine. *Semin. Nucl. Med.* **2014**, *44*, 193–201. [CrossRef] [PubMed]
12. Mettler, F.A., Jr.; Huda, W.; Yoshizumi, T.T.; Mahesh, M. Effective doses in radiology and diagnostic nuclear medicine: A catalog. *Radiology* **2008**, *248*, 254–263. [CrossRef] [PubMed]
13. Salvatori, M.; Rizzo, A.; Rovera, G.; Indovina, L.; Schillaci, O. Radiation dose in nuclear medicine: The hybrid imaging. *Radiol. Med.* **2019**, *124*, 768–776. [CrossRef] [PubMed]

MIM Software Inc. v. Progenics Pharmaceuticals, Inc.
IPR2025-00630
Progenics EX2017

14. Liberti, M.V.; Locasale, J.W. The Warburg Effect: How Does it Benefit Cancer Cells? *Trends. Biochem. Sci.* **2016**, *41*, 211–218. [CrossRef]
15. Deng, X.; Rong, J.; Wang, L.; Vasdev, N.; Zhang, L.; Josephson, L.; Liang, S.H. Chemistry for Positron Emission Tomography: Recent Advances in ^{11}C-, ^{18}F-, ^{13}N-, and ^{15}O-Labeling Reactions. *Angew. Chemie. Int. Ed.* **2019**, *58*, 2580–2605. [CrossRef]
16. Qi, Y.; Liu, X.; Li, J.; Yao, H.; Yuan, S. Fluorine-18 labeled amino acids for tumor PET/CT imaging. *Oncotarget* **2017**, *8*, 60581–60588. [CrossRef]
17. Katsanos, A.H.; Alexiou, G.A.; Fotopoulos, A.D.; Jabbour, P.; Kyritsis, A.P.; Sioka, C. Performance of 18F-FDG,11C-Methionine, and 18F-FET PET for Glioma Grading: A Meta-analysis. *Clin. Nucl. Med.* **2019**, *44*, 864–869. [CrossRef]
18. Liu, Z.; Chen, H.; Chen, K.; Shao, Y.; Kiesewetter, D.O.; Niu, G.; Chen, X. Boramino acid as a marker for amino acid transporters. *Sci. Adv.* **2015**, *1*, e1500694. [CrossRef]
19. Nodwell, M.B.; Yang, H.; Čolović, M.; Yuan, Z.; Merkens, H.; Martin, R.E.; Bénard, F.; Schaffer, P.; Britton, R. ^{18}F-Fluorination of Unactivated C-H Bonds in Branched Aliphatic Amino Acids: Direct Synthesis of Oncological Positron Emission Tomography Imaging Agents. *J. Am. Chem. Soc.* **2017**, *139*, 3595–3598. [CrossRef]
20. Nodwell, M.B.; Yang, H.; Merkens, H.; Malik, N.; Čolović, M.; Wagner, B.; Martin, R.E.; Bénard, F.; Schaffer, P.; Britton, R. ^{18}F-branched-chain amino acids: Structure-activity relationships and PET imaging potential. *J. Nucl. Med.* **2019**, *60*, 1003–1009. [CrossRef]
21. Paquette, M.; Lavallée, É.; Phoenix, S.; Ouellet, R.; Senta, H.; Van Lier, J.E.; Guérin, B.; Lecomte, R.; Turcotte, É.E. Improved estrogen receptor assessment by PET using the novel radiotracer ^{18}F-4FMFES in estrogen receptor–positive breast cancer patients: An ongoing phase II clinical trial. *J. Nucl. Med.* **2018**, *59*, 197–203. [CrossRef] [PubMed]
22. Takiguchi, Y. *Molecular Targeted Therapy of Lung Cancer*; Springer: Singapore, 2017.
23. Huang, G. *Nuclear Medicine in Oncology*; Springer: Singapore, 2019.
24. Cai, J.; Chang, J.; Yin, F. *Principles and Practice of Image-Guided Radiation Therapy of Lung Cancer*; CRC Press: Boca Raton, FL, USA, 2017.
25. Kandathil, A.; Kay, F.U.; Butt, Y.M.; Wachsmann, J.W.; Subramaniam, R.M. Role of FDG PET/CT in the eighth edition of TNM staging of non–small cell lung cancer. *Radiographics* **2018**, *38*, 2134–2149. [CrossRef] [PubMed]
26. Telo, S.; Calderoni, L.; Vichi, S.; Zagni, F.; Castellucci, P.; Fanti, S. Review: Alternative and new radiopharmaceutical agents for lung cancer. *Curr. Radiopharm.* **2019**, *13*, 185–194. [CrossRef] [PubMed]
27. Rayamajhi, S.J.; Mittal, B.R.; Maturu, V.N.; Agarwal, R.; Bal, A.; Dey, P.; Shukla, J.; Gupta, D. (18)F-FDG and (18)F-FLT PET/CT imaging in the characterization of mediastinal lymph nodes. *Ann. Nucl. Med.* **2016**, *30*, 207–216. [CrossRef] [PubMed]
28. Saga, T.; Inubushi, M.; Koizumi, M.; Yoshikawa, K.; Zhang, M.R.; Tanimoto, K.; Horiike, A.; Yanagitani, N.; Ohyanagi, F.; Nishio, M. Prognostic value of (18) F-fluoroazomycin arabinoside PET/CT in patients with advanced non-small-cell lung cancer. *Cancer Sci.* **2015**, *106*, 1554–1560. [CrossRef] [PubMed]
29. Szyszko, T.A.; Yip, C.; Szlosarek, P.; Goh, V.; Cook, G.J. The role of new PET tracers for lung cancer. *Lung Cancer* **2016**, *94*, 7–14. [CrossRef] [PubMed]
30. Theodoropoulos, A.S.; Gkiozos, I.; Kontopyrgias, G.; Charpidou, A.; Kotteas, E.; Kyrgias, G.; Tolia, M. Modern radiopharmaceuticals for lung cancer imaging with positron emission tomography/computed tomography scan: A systematic review. *SAGE Open Med.* **2020**, *8*, 2050312120961594. [CrossRef]
31. Araz, M.; Aras, G.; Küçük, Ö.N. The role of 18F–NaF PET/CT in metastatic bone disease. *J. Bone Oncol.* **2015**, *4*, 92–97. [CrossRef]
32. Wang, R.; Shen, G.; Huang, M.; Tian, R. The Diagnostic Role of ^{18}F-Choline, ^{18}F-Fluciclovine and ^{18}F-PSMA PET/CT in the Detection of Prostate Cancer with Biochemical Recurrence: A Meta-Analysis. *Front. Oncol.* **2021**, *11*, 684629. [CrossRef]
33. Sørensen, M.; Mikkelsen, K.S.; Frisch, K.; Villadsen, G.E.; Keiding, S. Regional metabolic liver function measured by 2-[^{18}F]fluoro-2-deoxy-galactose PET/CT in patients with cirrhosis. *J. Hepatol.* **2013**, *58*, 1119–1124. [CrossRef]
34. Horsager, J.; Munk, O.L.; Sørensen, M. Metabolic liver function measured in vivo by dynamic (18)F-FDGal PET/CT without arterial blood sampling. *EJNMMI Res.* **2015**, *5*, 32. [CrossRef] [PubMed]
35. Bak-Fredslund, K.P.; Keiding, S.; Villadsen, G.E.; Kramer, S.; Schlander, S.; Sørensen, M. [^{18}F]-Fluoro-2-deoxy-D-galactose positron emission tomography/computed tomography as complementary imaging tool in patients with hepatocellular carcinoma. *Liver Int.* **2020**, *40*, 447–455. [CrossRef] [PubMed]
36. Kim, S.J.; Pak, K.; Kim, K. Diagnostic accuracy of F-18 FDG PET or PET/CT for detection of lymph node metastasis in clinically node negative head and neck cancer patients: A systematic review and meta-analysis. *Am. J. Otolaryngol.* **2019**, *40*, 297–305. [CrossRef] [PubMed]
37. Castaldi, P.; Leccisotti, L.; Bussu, F.; Micciché, F.; Rufini, V. Role of (18)F-FDG PET-CT in head and neck squamous cell carcinoma. *Acta Otorhinolaryngol. Ital.* **2013**, *33*, 1–8. [PubMed]
38. Helsen, N.; Roothans, D.; Van Den Heuvel, B.; Van den Wyngaert, T.; Van den Weyngaert, D.; Carp, L.; Stroobants, S. 18F-FDG-PET/CT for the detection of disease in patients with head and neck cancer treated with radiotherapy. *PLoS ONE* **2017**, *12*, e0182350. [CrossRef] [PubMed]
39. Schöder, H.; França, P.; Nakajima, R.; Burnazi, E.; Roberts, S.; Brand, C.; Grkovski, M.; Mauguen, A.; Dunphy, M.P.; Ghossein, R.A.; et al. Safety and Feasibility of PARP1/2 Imaging with ^{18}F-PARPi in Patients with Head and Neck Cancer. *Clin. Cancer Res.* **2020**, *26*, 3110–3116. [CrossRef] [PubMed]
40. Carney, B.; Kossatz, S.; Reiner, T. Molecular imaging of PARP. *J. Nucl. Med.* **2017**, *58*, 1025–1030. [CrossRef]

MIM Software Inc. v. Progenics Pharmaceuticals, Inc.
IPR2025-00630
Progenics EX2017

41. Wilson, T.C.; Xavier, M.A.; Knight, J.; Verhoog, S.; Torres, J.B.; Mosley, M.; Hopkins, S.L.; Wallington, S.; Allen, P.D.; Kersemans, V.; et al. PET imaging of PARP expression using (18)F-Olaparib. *J. Nucl. Med.* **2019**, *60*, 504–510. [CrossRef]
42. Guru, N.; De Souza França, P.D.; Pirovano, G.; Huang, C.; Patel, G.S.; Reiner, T. [^{18}F]PARPi Imaging Is Not Affected by HPV Status In Vitro. *Mol. Imaging* **2021**, *2021*, 6641397. [CrossRef]
43. Young, R.J.; Demétrio De Souza França, P.; Pirovano, G.; Piotrowski, A.F.; Nicklin, P.J.; Riedl, C.C.; Schwartz, J.; Bale, T.A.; Donabedian, P.L.; Kossatz, S.; et al. Preclinical and first-in-human-brain-cancer applications of [^{18}F]poly (ADP-ribose) polymerase inhibitor PET/MR. *Neurooncol. Adv.* **2020**, *2*, vdaa119. [CrossRef]
44. Ramos-Álvarez, I.; Moreno, P.; Mantey, S.A.; Nakamura, T.; Nuche-Berenguer, B.; Moody, T.W.; Coy, D.H.; Jensen, R.T. Insights into bombesin receptors and ligands: Highlighting recent advances. *Peptides* **2015**, *72*, 128–144. [CrossRef] [PubMed]
45. Moreno, P.; Mantey, S.A.; Nuche-Berenguer, B.; Reitman, M.L.; González, N.; Coy, D.H.; Jensen, R.T. Comparative pharmacology of bombesin receptor subtype-3, nonpeptide agonist MK-5046, a universal peptide agonist, and peptide antagonist Bantag-1 for human bombesin receptors. *J. Pharmacol. Exp. Ther.* **2013**, *347*, 100–116. [CrossRef] [PubMed]
46. Sah, B.R.; Burger, I.A.; Schibli, R.; Friebe, M.; Dinkelborg, L.; Graham, K.; Borkowski, S.; Bacher-Stier, C.; Valencia, R.; Srinivasan, A.; et al. Dosimetry and first clinical evaluation of the new 18F-radiolabeled bombesin analogue BAY 864367 in patients with prostate cancer. *J. Nucl. Med.* **2015**, *56*, 372–378. [CrossRef] [PubMed]
47. Varshney, R.; Chitkara, A.; Saklani, M.; Kaur, A.; Mathur, R.; Tiwari, A.; Singh, B.; Mishra, A.K. Targeting Bombesin Peptide Receptors for Cancer Imaging: Perspective in Prostate, Lung and Breast Cancer. *Nov. Appro. Can. Study* **2020**, *5*, 483–491. [CrossRef]
48. Taddei, C.; Pike, V.W. [^{11}C]Carbon monoxide: Advances in production and application to PET radiotracer development over the past 15 years. *EJNMMI Radiopharm. Chem.* **2019**, *4*, 25. [CrossRef]
49. Qu, W.; Hu, B.; Babich, J.W.; Waterhouse, N.; Dooley, M.; Ponnala, S.; Urgiles, J. A general ^{11}C-labeling approach enabled by fluoride-mediated desilylation of organosilanes. *Nat. Commun.* **2020**, *11*, 1736. [CrossRef]
50. Yang, L.; Scott, P.J.H.; Shao, X. [^{11}C]Carbon Dioxide: Starting Point for Labeling PET Radiopharmaceuticals. In *Carbon Dioxide Chemistry, Capture and Oil Recovery*; Karamé, I., Shaya, J., Srour, H., Eds.; IntechOpen: London, UK, 2017. [CrossRef]
51. Moldovean, S.N.; Timaru, D.G.; Chiş, V. All-Atom Molecular Dynamics Investigations on the Interactions between D2 Subunit Dopamine Receptors and Three 11C-Labeled Radiopharmaceutical Ligands. *Int. J. Mol. Sci.* **2022**, *23*, 2005. [CrossRef]
52. Dahl, K.; Halldin, C.; Schou, M. New methodologies for the preparation of carbon-11 labeled radiopharmaceuticals. *Clin. Transl. Imaging* **2017**, *5*, 275–289. [CrossRef]
53. Gómez-Vallejo, V.; Gaja, V.; Koziorowski, J.; Llop, J. Specific activity of 11 C-labeled radiotracers: A big challenge for PET chemists. In *Positron Emission Tomography—Current Clinical and Research Aspects*; Hsieh, C.-H., Ed.; IntechOpen: London, UK, 2012; pp. 183–209. [CrossRef]
54. Rotstein, B.H.; Liang, S.H.; Holland, J.P.; Collier, T.L.; Hooker, J.M.; Wilson, A.A.; Vasdev, N. 11CO_2 Fixation: A renaissance in PET radiochemistry. *Chem. Comm.* **2013**, *49*, 5621–5629. [CrossRef]
55. Taddei, C.; Gee, A.D. Recent progress in [^{11}C]carbon dioxide ([^{11}C]CO_2) and [^{11}C]carbon monoxide ([^{11}C]CO) chemistry. *J. Label. Comp. Radiopharm.* **2018**, *61*, 237–251. [CrossRef]
56. Haywood, T.; Kealey, S.; Sánchez-Cabezas, S.; Hall, J.J.; Allott, L.; Smith, G.; Plisson, C.; Miller, P.W. Carbon-11 radiolabelling of organosulfur compounds: (11)C synthesis of the progesterone receptor agonist Tanaproget. *Chem. Eur. J.* **2015**, *21*, 9034–9038. [CrossRef] [PubMed]
57. Haywood, T.; Cesarec, S.; Kealey, S.; Plisson, C.; Miller, P.W. Ammonium [^{11}C]thiocyanate: Revised preparation and reactivity studies of a versatile nucleophile for carbon-11 radiolabelling. *MedChemComm* **2018**, *9*, 1311–1314. [CrossRef] [PubMed]
58. Haskali, M.B.; Pike, V.W. [^{11}C]Fluoroform, a breakthrough for versatile labeling of PET radiotracer trifluoromethyl groups in high molar activity. *Chem. Eur. J.* **2017**, *23*, 8156–8160. [CrossRef] [PubMed]
59. Picchio, M.; Castellucci, P. Clinical indications of ^{11}C-choline PET/CT in prostate cancer patients with biochemical relapse. *Theranostics* **2012**, *2*, 313–317. [CrossRef]
60. Grassi, I.; Nanni, C.; Allegri, V.; Morigi, J.J.; Montini, G.C.; Castellucci, P.; Fanti, S. The clinical use of PET with (11)C-acetate. *Am. J. Nucl. Med. Mol. Imaging.* **2012**, *2*, 33–47.
61. Chen, M.; Zhu, W.; Du, J.; Yang, C.; Han, B.; Zhou, D.; Huo, L.; Zhuang, J. 11C-acetate positron emission tomography is more precise than 18F-fluorodeoxyglucose positron emission tomography in evaluating tumor burden and predicting disease risk of multiple myeloma. *Sci. Rep.* **2021**, *11*, 22188. [CrossRef]
62. Spick, C.; Herrmann, K.; Czernin, J. Evaluation of Prostate Cancer with 11C-Acetate PET/CT. *J. Nucl. Med.* **2016**, *57* (Suppl. 3), 30S–37S. [CrossRef]
63. Jambor, I.; Borra, R.; Kemppainen, J.; Lepomäki, V.; Parkkola, R.; Dean, K.; Alanen, K.; Arponen, E.; Nurmi, M.; Aronen, H.J.; et al. Improved detection of localized prostate cancer using co-registered MRI and 11 C-acetate PET/CT. *Eur. J. Radiol.* **2012**, *81*, 2966–2972. [CrossRef]
64. Mena, E.; Turkbey, B.; Mani, H.; Adler, S.; Valera, V.A.; Bernardo, M.; Shah, V.; Pohida, T.; McKinney, Y.; Kwarteng, G.; et al. 11 C-acetate PET/CT in localized prostate cancer: A study with MRI and histopathologic correlation. *J. Nucl. Med.* **2012**, *53*, 538–545. [CrossRef]

MIM Software Inc. v. Progenics Pharmaceuticals, Inc.
IPR2025-00630
Progenics EX2017

65. Schöder, H.; Ong, S.C.; Reuter, V.E.; Cai, S.; Burnazi, E.; Dalbagni, G.; Larson, S.M.; Bochner, B.H. Initial results with (11)C-acetate positron emission tomography/computed tomography (PET/CT) in the staging of urinary bladder cancer. *Mol. Imaging. Biol.* **2012**, *14*, 245–251. [CrossRef]
66. Haseebuddin, M.; Dehdashti, F.; Siegel, B.A.; Liu, J.; Roth, E.B.; Nepple, K.G.; Siegel, C.L.; Fischer, K.C.; Kibel, A.S.; Andriole, G.L.; et al. ^{11}C-acetate PET/CT before radical prostatectomy: Nodal staging and treatment failure prediction. *J. Nucl. Med.* **2013**, *54*, 699–706. [CrossRef] [PubMed]
67. Daouacher, G.; von Below, C.; Gestblom, C.; Ahlström, H.; Grzegorek, R.; Wassberg, C.; Sörensen, J.; Waldén, M. Laparoscopic extended pelvic lymph node (LN) dissection as validation of the performance of [(11)C]-acetate positron emission tomography/computer tomography in the detection of LN metastasis in intermediate- and high-risk prostate cancer. *BJU Int.* **2016**, *118*, 77–83. [CrossRef] [PubMed]
68. Strandberg, S.; Karlsson, C.T.; Sundström, T.; Ögren, M.; Ögren, M.; Axelsson, J.; Riklund, K. (11)C-acetate PET/CT in pre-therapeutic lymph node staging in high-risk prostate cancer patients and its influence on disease management: A retrospective study. *EJNMMI Res.* **2014**, *4*, 55. [CrossRef] [PubMed]
69. Schumacher, M.C.; Radecka, E.; Hellström, M.; Jacobsson, H.; Sundin, A. [^{11}C]-acetate positron emission tomography–computed tomography imaging of prostate cancer lymph-node metastases correlated with histopathological findings after extended lymphadenectomy. *Scand. J. Urol.* **2015**, *49*, 35–42. [CrossRef]
70. Leisser, A.; Pruscha, K.; Ubl, P.; Wadsak, W.; Mayerhöfer, M.; Mitterhauser, M.; Hacker, M.; Kramer, G.; Shariat, S.; Karanikas, G.; et al. Evaluation of fatty acid synthase in prostate cancer recurrence: SUV of [(11)C]-acetate PET as a prognostic marker. *Prostate* **2015**, *75*, 1760–1767. [CrossRef]
71. Spick, C.; Polanec, S.H.; Mitterhauser, M.; Wadsak, W.; Anner, P.; Reiterits, B.; Haug, A.R.; Hacker, M.; Beheshti, M.; Karanikas, G. Detection of bone metastases using ^{11}C-acetate PET in patients with prostate cancer with biochemical recurrence. *Anticancer Res.* **2015**, *35*, 6787–6791.
72. Bahce, I.; Yaqub, M.; Errami, H.; Schuit, R.C.; Schober, P.; Thunnissen, E.; Windhorst, A.D.; Lammertsma, A.A.; Smit, E.F.; Hendrikse, N.H. Effects of erlotinib therapy on [(11)C]erlotinib uptake in EGFR mutated, advanced NSCLC. *EJNMMI Res.* **2016**, *6*, 10. [CrossRef]
73. Petrulli, J.R.; Zheng, M.; Huang, Y.; Nabulsi, N.B.; Goldberg, S.B.; Contessa, J.N.; Morris, E.D. Evaluation of quantitative modeling methods in whole-body, dynamic [^{11}C]-erlotinib PET. *Am. J. Nucl. Med. Mol. Imaging* **2021**, *11*, 143–153.
74. Yaqub, M.; Bahce, I.; Voorhoeve, C.; Schuit, R.C.; Windhorst, A.D.; Hoekstra, O.S.; Boellaard, R.; Hendrikse, N.H.; Smit, E.F.; Lammertsma, A.A. Quantitative and simplified analysis of 11C-erlotinib studies. *J. Nucl. Med.* **2016**, *57*, 861–866. [CrossRef]
75. Kumar, K.; Ghosh, A. Radiochemistry, Production Processes, Labeling Methods, and ImmunoPET Imaging Pharmaceuticals of Iodine-124. *Molecules* **2021**, *26*, 414. [CrossRef]
76. Salodkin, S.S.; Golovkov, V.M. Cyclotron Production of Iodine-124. *Russ. Phys. J.* **2020**, *62*, 2347–2353. [CrossRef]
77. Dubost, E.; McErlain, H.; Babin, V.; Sutherland, A.; Cailly, T. Recent Advances in Synthetic Methods for Radioiodination. *J. Org. Chem.* **2020**, *85*, 8300–8310. [CrossRef] [PubMed]
78. Ogawa, K.; Takeda, T.; Yokokawa, M.; Yu, J.; Makino, A.; Kiyono, Y.; Shiba, K.; Kinuya, S.; Odani, A. Comparison of Radioiodine-or Radiobromine-labeled RGD Peptides between Direct and Indirect Labeling Methods. *Chem. Pharm. Bull.* **2018**, *66*, 651–659. [CrossRef] [PubMed]
79. Rangger, C.; Haubner, R. Radiolabelled Peptides for Positron Emission Tomography and Endoradiotherapy in Oncology. *Pharmaceuticals* **2020**, *13*, 22. [CrossRef] [PubMed]
80. Wright, B.D.; Lapi, S.E. Designing the Magic Bullet? The Advancement of Immuno-PET into Clinical Use. *J. Nucl. Med.* **2013**, *54*, 1171–1174. [CrossRef] [PubMed]
81. Samnick, S.; Al-Momani, E.; Schmid, J.S.; Mottok, A.; Buck, A.K.; Lapa, C. Initial Clinical Investigation of [^{18}F]Tetrafluoroborate PET/CT in Comparison to [^{124}I]iodine PET/CT for Imaging Thyroid Cancer. *Clin. Nucl. Med.* **2018**, *43*, 162–167. [CrossRef] [PubMed]
82. Seo, Y.; Gustafson, W.C.; Dannoon, S.F.; Nekritz, E.A.; Lee, C.L.; Murphy, S.T.; VanBrocklin, H.F.; Hernandez-Pampaloni, M.; Haas-Kogan, D.A.; Weiss, W.A.; et al. Tumor dosimetry using [^{124}I]m-iodobenzylguanidine microPET/CT for [^{131}I]m-iodobenzylguanidine treatment of neuroblastoma in a murine xenograft model. *Mol. Imaging Biol.* **2012**, *14*, 735–742. [CrossRef] [PubMed]
83. Silberstein, E.B. Radioiodine: The classic theranostic agent. *Semin. Nucl. Med.* **2012**, *42*, 164–170. [CrossRef]
84. Cascini, G.L.; Niccoli Asabella, A.; Notaristefano, A.; Restuccia, A.; Ferrari, C.; Rubini, D.; Altini, C.; Rubini, G. 124 Iodine: A Longer-Life Positron Emitter Isotope—New Opportunities in Molecular Imaging. *Biomed. Res. Int.* **2014**, *2014*, 672094. [CrossRef]
85. Guo, X.; Zhou, N.; Chen, Z.; Liu, T.; Xu, X.; Lei, X.; Shen, L.; Gao, J.; Yang, Z.; Zhu, H. Construction of ^{124}I-trastuzumab for noninvasive PET imaging of HER2 expression: From patient-derived xenograft models to gastric cancer patients. *Gastric Cancer* **2020**, *23*, 614–626. [CrossRef]
86. Zettlitz, K.A.; Tavaré, R.; Knowles, S.M.; Steward, K.K.; Timmerman, J.M.; Wu, A.M. ImmunoPET of Malignant and Normal B Cells with ^{89}Zr- and ^{124}I-Labeled Obinutuzumab Antibody Fragments Reveals Differential CD20 Internalization In Vivo. *Clin. Cancer Res.* **2017**, *23*, 7242–7252. [CrossRef] [PubMed]

MIM Software Inc. v. Progenics Pharmaceuticals, Inc.
IPR2025-00630
Progenics EX2017

87. Huang, H.F.; Zhu, H.; Li, G.H.; Xie, Q.; Yang, X.T.; Xu, X.X.; Tian, X.B.; Wan, Y.K.; Yang, Z. Construction of Anti-hPD-L1 HCAb Nb6 and in Situ ^{124}I Labeling for Noninvasive Detection of PD-L1 Expression in Human Bone Sarcoma. *Bioconj. Chem.* **2019**, *30*, 2614–2623. [CrossRef] [PubMed]
88. Huang, H.; Zhu, H.; Xie, Q.; Tian, X.; Yang, X.; Feng, F.; Jiang, Q.; Sheng, X.; Yang, Z. Evaluation of ^{124}I-JS001 for hPD1 immuno-PET imaging using sarcoma cell homografts in humanized mice. *Acta Pharm. Sin. B* **2020**, *10*, 1321–1330. [CrossRef] [PubMed]
89. Escorcia, F.E.; Steckler, J.M.; Abdel-Atti, D.; Price, E.W.; Carlin, S.D.; Scholz, W.W.; Lewis, J.S.; Houghton, J.L. Tumor-Specific Zr-89 Immuno-PET Imaging in a Human Bladder Cancer Model. *Mol. Imaging Biol.* **2018**, *20*, 808–815. [CrossRef]
90. Houghton, J.L.; Abdel-Atti, D.; Scholz, W.W.; Lewis, J.S. Preloading with Unlabeled CA19.9 Targeted Human Monoclonal Antibody Leads to Improved PET Imaging with ^{89}Zr-5B1. *Mol. Pharm.* **2017**, *14*, 908–915. [CrossRef]
91. Lohrmann, C.; O'Reilly, E.M.; O'Donoghue, J.A.; Pandit-Taskar, N.; Carrasquillo, J.A.; Lyashchenko, S.K.; Ruan, S.; Teng, R.; Scholz, W.; Maffuid, P.W.; et al. Retooling a Blood-Based Biomarker: Phase I Assessment of the High-Affinity CA19-9 Antibody HuMab-5B1 for Immuno-PET Imaging of Pancreatic Cancer. *Clin. Cancer Res.* **2019**, *25*, 7014–7023. [CrossRef]
92. Zanzonico, P.; Carrasquillo, J.A.; Pandit-Taskar, N.; O'Donoghue, J.A.; Humm, J.L.; Smith-Jones, P.; Ruan, S.; Divgi, C.; Scott, A.M.; Kemeny, N.E.; et al. PET-based compartmental modeling of (124)I-A33 antibody: Quantitative characterization of patient-specific tumor targeting in colorectal cancer. *Eur. J. Nucl. Med. Mol. Imaging* **2015**, *42*, 1700–1706. [CrossRef]
93. Stillebroer, A.B.; Franssen, G.M.; Mulders, P.F.; Oyen, W.J.; van Dongen, G.A.; Laverman, P.; Oosterwijk, E.; Boerman, O.C. ImmunoPET Imaging of Renal Cell Carcinoma with (124)I- and (89)Zr-Labeled Anti-CAIX Monoclonal Antibody cG250 in Mice. *Cancer Biother. Radiopharm.* **2013**, *28*, 510–515. [CrossRef]
94. Cheal, S.M.; Punzalan, B.; Doran, M.G.; Evans, M.J.; Osborne, J.R.; Lewis, J.S.; Zanzonico, P.; Larson, S.M. Pairwise comparison of 89Zr- and 124I-labeled cG250 based on positron emission tomography imaging and nonlinear immunokinetic modeling: In vivo carbonic anhydrase IX receptor binding and internalization in mouse xenografts of clear-cell renal cell carcinoma. *Eur. J. Nucl. Med. Mol. Imaging* **2014**, *41*, 985–994. [CrossRef]
95. Divgi, C.R.; Uzzo, R.G.; Gatsonis, C.; Bartz, R.; Treutner, S.; Yu, J.Q.; Chen, D.; Carrasquillo, J.A.; Larson, S.M.; Bevan, P.; et al. Positron Emission Tomography/Computed Tomography Identification of Clear Cell Renal Cell Carcinoma: Results from the REDECT Trial. *J. Clin. Oncol.* **2013**, *31*, 187–194. [CrossRef]
96. Povoski, S.P.; Hall, N.C.; Murrey, D.A., Jr.; Sharp, D.S.; Hitchcock, C.L.; Mojzisik, C.M.; Bahnson, E.E.; Knopp, M.V.; Martin, E.W., Jr.; Bahnson, R.R. Multimodal Imaging and Detection Strategy With 124I-Labeled Chimeric Monoclonal Antibody cG250 for Accurate Localization and Confirmation of Extent of Disease During Laparoscopic and Open Surgical Resection of Clear Cell Renal Cell Carcinoma. *Surg. Innov.* **2013**, *20*, 59–69. [CrossRef] [PubMed]
97. Smaldone, M.C.; Chen, D.Y.T.; Yu, J.Q.; Pilmack, E.R. Potential role of (124)I-girentuximab in the presurgical diagnosis of clear-cell renal cell cancer. *Biologics* **2012**, *6*, 395–407. [CrossRef] [PubMed]
98. Lau, J.; Lin, K.S.; Benard, F. Past, Present, and Future: Development of Theranostic Agents Targeting Carbonic Anhydrase IX. *Theranostics* **2017**, *7*, 4322–4339. [CrossRef] [PubMed]
99. Maurer, T.; Eiber, M.; Schwaiger, M.; Gschwend, J.E. Current use of PSMA-PET in prostate cancer management. *Nat. Rev. Urol.* **2016**, *13*, 226–235. [CrossRef] [PubMed]
100. Tolmachev, V.; Malmberg, J.; Estrada, S.; Eriksson, O.; Orlova, A. Development of a 124I-labeled version of the anti-PSMA monoclonal antibody capromab for immunoPET staging of prostate cancer: Aspects of labeling chemistry and biodistribution. *Int. J. Oncol.* **2014**, *44*, 1998–2008. [CrossRef]
101. Frigerio, B.; Morlino, S.; Luison, E.; Seregni, E.; Lorenzoni, A.; Satta, A.; Valdagni, R.; Bogni, A.; Chiesa, C. Anti-PSMA ^{124}I-scFvD2B as a new immuno-PET tool for prostate cancer: Preclinical proof of principle. *J. Exp. Clin. Cancer Res.* **2019**, *38*, 326–334. [CrossRef]
102. Tagawa, S.T.; Milowsky, M.I.; Morris, M.; Vallabhajosula, S.; Christos, P.; Akhtar, N.H.; Osborne, J.; Goldsmith, S.J.; Larson, S.; Taskar, N.P.; et al. Phase II Study of Lutetium-177-Labeled Anti-Prostate-Specific Membrane Antigen Monoclonal Antibody J591 for Metastatic Castration-Resistant Prostate Cancer. *Clin. Cancer Res.* **2013**, *19*, 5182–5191. [CrossRef]
103. Pandit-Taskar, N.; O'Donoghue, J.A.; Beylergil, V.; Lyashchenko, S.; Ruan, S.; Solomon, S.B.; Durack, J.C.; Carrasquillo, J.A.; Lefkowitz, R.A.; Gonen, M.; et al. ^{89}Zr-huJ591 Immuno-PET imaging in patients with advanced metastatic prostate cancer. *Eur. J. Nucl. Med. Mol. Imaging* **2014**, *41*, 2093–2105. [CrossRef]
104. Pandit-Taskar, N.; O'Donoghue, J.A.; Durack, J.C.; Lyashchenko, S.K.; Cheal, S.M.; Beylergil, V.; Lefkowitz, R.A.; Carrasquillo, J.A.; Martinez, D.F.; Fung, A.M.; et al. A Phase I/II Study for Analytic Validation of 89Zr-J591 ImmunoPET as a Molecular Imaging Agent for Metastatic Prostate Cancer. *Clin. Cancer Res.* **2015**, *21*, 5277–5285. [CrossRef]
105. Pandit-Taskar, N.; O'Donoghue, J.A.; Divgi, C.R.; Wills, E.A.; Schwartz, L.; Gönen, M.; Smith-Jones, P.; Bander, N.H.; Scher, H.I.; Larson, S.M.; et al. Indium 111-labeled J591 anti-PSMA antibody for vascular targeted imaging in progressive solid tumors. *EJNMMI Res.* **2015**, *5*, 28. [CrossRef]
106. Fung, E.K.; Cheal, S.M.; Fareedy, S.B.; Punzalan, B.; Beylergil, V.; Amir, J.; Chalasani, S.; Weber, W.A.; Spratt, D.E.; Veach, D.R.; et al. Targeting of radiolabeled J591 antibody to PSMA-expressing tumors: Optimization of imaging and therapy based on non-linear compartmental modeling. *EJNMMI Res.* **2016**, *6*, 7. [CrossRef] [PubMed]

MIM Software Inc. v. Progenics Pharmaceuticals, Inc.
IPR2025-00630
Progenics EX2017

107. Knowles, S.M.; Zettlitz, K.J.; Tavare, R.; Rochefortl, M.M.; Salazar, F.B.; Stout, D.B.; Yazaki, P.J.; Reiter, R.E.; Wu, A.M. Quantitative ImmunoPET of Prostate Cancer Xenografts with 89 Zr- and 124 I-Labeled Anti-PSCA A11 Minibody. *J. Nucl. Med.* **2014**, *55*, 452–459. [CrossRef] [PubMed]
108. Knowles, S.M.; Tavare, R.; Zettlitz, K.J.; Rochefortl, M.M.; Salazar, F.B.; Jiang, Z.K.; Reiter, R.E.; Wu, A.M. Applications of ImmunoPET: Using 124 I-Anti-PSCA A11 Minibody for Imaging Disease Progression and Response to Therapy in Mouse Xenograft Models of Prostate Cancer. *Clin. Cancer Res.* **2014**, *20*, 6367–6378. [CrossRef]
109. Tsai, W.K.; Zettlitz, K.A.; Tavare, R.; Kobayashi, N.; Reiter, R.E.; Wy, A.M. Dual-Modality ImmunoPET/Fluorescence Imaging of Prostate Cancer with an Anti-PSCA Cys-Minibody. *Theranostics* **2018**, *8*, 5903–5914. [CrossRef] [PubMed]
110. Zettlitz, K.A.; Wen-Ting, K.T.; Knowles, S.M.; Kobayashi, N.; Donahue, T.R.; Reiter, R.E.; Wu, A.M. Dual-Modality Immuno-PET and Near-Infrared Fluorescence Imaging of Pancreatic Cancer Using an Anti–Prostate Stem Cell Antigen Cys-Diabody. *J. Nucl. Med.* **2018**, *59*, 1398–1406. [CrossRef] [PubMed]
111. Carrasquillo, J.A.; O'Donoghue, J.A.; Beylergil, V.; Ruan, S.; Pandit-Taskar, N.; Larson, S.M.; Smith-Jones, P.M.; Lyashchenko, S.K.; Ohishi, N.; Ohtomo, T.; et al. I-124 codrituzumab imaging and biodistribution in patients with hepatocellular carcinoma. *EJNMMI Res.* **2018**, *8*, 20. [CrossRef] [PubMed]
112. Mikulová, M.B.; Mikuš, P. Advances in Development of Radiometal Labeled Amino Acid-Based Compounds for Cancer Imaging and Diagnostics. *Pharmaceuticals* **2021**, *14*, 167. [CrossRef]
113. Yoon, J.K.; Park, B.N.; Ryu, E.K.; An, Y.S.; Lee, S.J. Current Perspectives on 89Zr-PET Imaging. *Int. J. Mol. Sci.* **2020**, *21*, 4309. [CrossRef]
114. Brandt, M.; Cardinale, J.; Aulsebrook, M.L.; Gasser, G.; Mindt, T.L. An Overview of PET Radiochemistry, Part 2: Radiometals. *J. Nucl. Med.* **2018**, *59*, 1500–1506. [CrossRef]
115. Laforest, R.; Lapi, S.E.; Oyama, R.; Bose, R.; Tabchy, A.; Marquez-Nostra, B.V.; Burkemper, J.; Wright, B.D.; Frye, J.; Frye, S.; et al. [^{89}Zr]Trastuzumab: Evaluation of Radiation Dosimetry, Safety, and Optimal Imaging Parameters in Women with HER2-Positive Breast Cancer. *Mol. Imaging Biol.* **2016**, *18*, 952–959. [CrossRef]
116. Ulaner, G.A.; Hyman, D.M.; Ross, D.S.; Corben, A.; Chandarlapaty, S.; Goldfarb, S.; McArthur, H.; Erinjeri, J.P.; Solomon, S.B.; Kolb, H.; et al. Detection of HER2-Positive Metastases in Patients with HER2-Negative Primary Breast Cancer Using 89Zr-Trastuzumab PET/CT. *J. Nucl. Med.* **2016**, *57*, 1523–1528. [CrossRef] [PubMed]
117. Janjigian, Y.Y.; Viola-Villegas, N.; Holland, J.P.; Divilov, V.; Carlin, S.D.; Gomes-DaGama, E.M.; Chiosis, G.; Carbonetti, G.; de Stanchina, E.; Lewis, J.S. Monitoring afatinib treatment in HER2-positive gastric cancer with 18F-FDG and 89Zr-trastuzumab PET. *J. Nucl. Med.* **2013**, *54*, 936–943. [CrossRef]
118. Gaykema, S.B.; Brouwers, A.H.; Lub-de Hooge, M.N.; Pleijhuis, R.G.; Timmer-Bosscha, H.; Pot, L.; van Dam, G.M.; van der Meulen, S.B.; de Jong, J.R.; Bart, J.; et al. 89Zr-bevacizumab PET imaging in primary breast cancer. *J. Nucl. Med.* **2013**, *54*, 1014–1018. [CrossRef] [PubMed]
119. Van Asselt, S.J.; Oosting, S.F.; Brouwers, A.H.; Bongaerts, A.H.; de Jong, J.R.; Lub-de Hooge, M.N.; Oude Munnink, T.H.; Fiebrich, H.B.; Sluiter, W.J.; Links, T.P.; et al. Everolimus reduces (89)Zr-bevacizumab tumor uptake in patients with neuroendocrine tumors. *J. Nucl. Med.* **2014**, *55*, 1087–1092. [CrossRef]
120. Oosting, S.F.; Brouwers, A.H.; van Es, S.C.; Nagengast, W.B.; Oude Munnink, T.H.; Lub-de Hooge, M.N.; Hollema, H.; de Jong, J.R.; de Jong, I.J.; de Haas, S.; et al. 89Zr-Bevacizumab PET Visualizes Heterogeneous Tracer Accumulation in Tumor Lesions of Renal Cell Carcinoma Patients and Differential Effects of Antiangiogenic Treatment. *J. Nucl. Med.* **2015**, *56*, 63–69. [CrossRef]
121. Bahce, I.; Huisman, M.C.; Verwer, E.E.; Ooijevaar, R.; Boutkourt, F.; Vugts, D.J.; van Dongen, G.A.; Boellaard, R.; Smit, E.F. Pilot study of (89)Zr-bevacizumab positron emission tomography in patients with advanced non-small cell lung cancer. *EJNMMI Res.* **2014**, *4*, 35–42. [CrossRef]
122. Jansen, M.H.; Veldhuijzen van Zanten, S.E.M.; van Vuurden, D.G.; Huisman, M.C.; Vugts, D.J.; Hoekstra, O.S.; van Dongen, G.A.; Kaspers, G.L. Molecular Drug Imaging: ^{89}Zr-bevacizumab PET in Children with Diffuse Intrinsic Pontine Glioma. *J. Nucl. Med.* **2017**, *58*, 711–716. [CrossRef] [PubMed]
123. Veldhuijzen van Zanten, S.E.M.; Sewing, A.C.P.; van Lingen, A.; Hoekstra, O.S.; Wesseling, P.; Meel, M.H.; van Vuurden, D.G.; Kaspers, G.J.L.; Hulleman, E.; Bugiani, M. Multiregional tumor drug-uptake imaging by PET and microvascular morphology in end-stage diffuse intrinsic pontine glioma. *J. Nucl. Med.* **2018**, *59*, 612–615. [CrossRef] [PubMed]
124. Oosting, S.F.; van Asselt, S.J.; Brouwers, A.H.; Bongaerts, A.H.; Steinberg, J.D.; de Jong, J.R.; Lub-de Hooge, M.N.; van der Horst-Schrivers, A.N.; Walenkamp, A.M.; Hoving, E.W.; et al. 89Zr-Bevacizumab PET Visualizes Disease Manifestations in Patients with von Hippel-Lindau Disease. *J. Nucl. Med.* **2016**, *57*, 1244–1250. [CrossRef]
125. Golestani, R.; Zeebregts, C.J.; Terwisscha van Scheltinga, A.G.; Lub-de Hooge, M.N.; van Dam, G.M.; Glaudemans, A.W.; Dierckx, R.A.; Tio, R.A.; Suurmeijer, A.J.; Boersma, H.H.; et al. Feasibility of vascular endothelial growth factor imaging in human atherosclerotic plaque using (89)Zr-bevacizumab positron emission tomography. *Mol. Imaging* **2013**, *12*, 235–243. [CrossRef]
126. Even, A.J.; Hamming-Vrieze, O.; van Elmpt, W.; Winnepenninckx, V.J.; Heukelom, J.; Tesselaar, M.E.; Vogel, W.V.; Hoeben, A.; Zegers, C.M.; Vugts, D.J.; et al. Quantitative assessment of Zirconium-89 labeled cetuximab using PET/CT imaging in patients with advanced head and neck cancer: A theragnostic approach. *Oncotarget* **2017**, *8*, 3870–3880. [CrossRef]
127. Menke-van der Houven van Oordt, C.W.; Gootjes, E.C.; Huisman, M.C.; Vugts, D.J.; Roth, C.; Luik, A.M.; Mulder, E.R.; Schuit, R.C.; Boellaard, R.; Hoekstra, O.S.; et al. 89Zr-cetuximab PET imaging in patients with advanced colorectal cancer. *Oncotarget* **2015**, *6*, 30384–30393. [CrossRef] [PubMed]

MIM Software Inc. v. Progenics Pharmaceuticals, Inc.
IPR2025-00630
Progenics EX2017

128. Makris, N.E.; Boellaard, R.; van Lingen, A.; Lammertsma, A.A.; van Dongen, G.A.; Verheul, H.M.; Menke, C.W.; Huisman, M.C. PET/CT-derived whole-body and bone marrow dosimetry of 89Zr-cetuximab. *J. Nucl. Med.* **2015**, *56*, 249–254. [CrossRef] [PubMed]
129. Jauw, Y.W.; Zijlstra, J.M.; de Jong, D.; Vugts, D.J.; Zweegman, S.; Hoekstra, O.S.; van Dongen, G.A.; Huisman, M.C. Performance of 89Zr-Labeled-Rituximab-PET as an Imaging Biomarker to Assess CD_{20} Targeting: A Pilot Study in Patients with Relapsed/Refractory Diffuse Large B Cell Lymphoma. *PLoS ONE* **2017**, *12*, e0169828. [CrossRef] [PubMed]
130. Bruijnen, S.; Tsang, A.S.M.; Raterman, H.; Ramwadhdoebe, T.; Vugts, D.; van Dongen, G.; Huisman, M.; Hoekstra, O.; Tak, P.P.; Voskuyl, A.; et al. B-cell imaging with zirconium-89 labeled rituximab PET-CT at baseline is associated with therapeutic response 24 weeks after initiation of rituximab treatment in rheumatoid arthritis patients. *Arthritis Res. Ther.* **2016**, *18*, 266. [CrossRef]
131. Carrasquillo, J.A.; Fine, B.M.; Pandit-Taskar, N.; Larson, S.M.; Fleming, S.E.; Fox, J.J.; Cheal, S.M.; O'Donoghue, J.A.; Ruan, S.; Ragupathi, G.; et al. Imaging patients with metastatic castration-resistant prostate cancer using ^{89}Zr-DFO-MSTP2109A anti-STEAP1 antibody. *J. Nucl. Med.* **2019**, *60*, 1517–1523. [CrossRef]
132. U.S. National Library of Medicine. ClinicalTrials. Phase 1 Imaging Study of 89Zr-DFO-HuMab-5B1 with HuMab-5B1—Full Text View. 2016. Available online: https://clinicaltrials.gov/ct2/show/NCT02687230 (accessed on 7 February 2022).
133. Lamberts, L.E.; Menke-van der Houven van Oordt, C.W.; ter Weele, E.J.; Bensch, F.; Smeenk, M.M.; Voortman, J.; Hoekstra, O.S.; Williams, S.P.; Fine, B.M.; Maslyar, D.; et al. ImmunoPET with anti-mesothelin antibody in patients with pancreatic and ovarian cancer before anti-mesothelin antibody-drug conjugate treatment. *Clin. Cancer Res.* **2016**, *22*, 1642–1652. [CrossRef]
134. Bensch, F.; van der Veen, E.L.; Lub-de Hooge, M.N.; Jorritsma-Smit, A.; Boellaard, R.; Kok, I.C.; Oosting, S.F.; Schröder, C.P.; Hiltermann, T.; van der Wekken, A.J.; et al. ^{89}Zr-atezolizumab imaging as a non-invasive approach to assess clinical response to PD-L1 blockade in cancer. *Nat. Med.* **2018**, *24*, 1852–1858. [CrossRef]
135. O'Donoghue, J.A.; Lewis, J.S.; Pandit-Taskar, N.; Fleming, S.E.; Schöder, H.; Larson, S.M.; Beylergil, V.; Ruan, S.; Lyashchenko, S.K.; Zanzonico, P.B.; et al. Pharmacokinetics, biodistribution, and radiation dosimetry for (89)zr-trastuzumab in patients with esophagogastric cancer. *J. Nucl. Med.* **2018**, *59*, 161–166. [CrossRef]
136. Sanchez-Vega, F.; Hechtman, J.F.; Castel, P.; Ku, G.Y.; Tuvy, Y.; Won, H.; Fong, C.J.; Bouvier, N.; Nanjangud, G.J.; Soong, J.; et al. *EGFR* and *MET* amplifications determine response to HER_2 inhibition in $ERBB_2$-amplified esophagogastric cancer. *Cancer Discov.* **2019**, *9*, 199–209. [CrossRef]
137. Moek, K.L.; Waaijer, S.; Kok, I.C.; Suurs, F.V.; Brouwers, A.H.; Menke-van der Houven van Oordt, C.W.; Wind, T.T.; Gietema, J.A.; Schröder, C.P.; Mahesh, S.; et al. ^{89}Zr-labeled bi-specific T-cell engager AMG 211 PET shows AMG 211 accumulation in CD3-rich tissues and clear, heterogeneous tumor uptake. *Clin. Cancer Res.* **2019**, *25*, 3517–3527. [CrossRef] [PubMed]
138. Lindenberg, L.; Adler, S.; Turkbey, I.B.; Mertan, F.; Ton, A.; Do, K.; Kummar, S.; Gonzalez, E.M.; Bhattacharyya, S.; Jacobs, P.M.; et al. Dosimetry and first human experience with ^{89}Zr-panitumumab. *Am. J. Nucl. Med. Mol. Imaging* **2017**, *7*, 195–203. [PubMed]
139. van Helden, E.J.; Elias, S.G.; Gerritse, S.L.; van Es, S.C.; Boon, E.; Huisman, M.C.; van Grieken, N.; Dekker, H.; van Dongen, G.; Vugts, D.J.; et al. [^{89}Zr]Zr-cetuximab PET/CT as biomarker for cetuximab mono- therapy in patients with RAS wild-type advanced colorectal cancer. *Eur. J. Nucl. Med. Mol. Imaging* **2020**, *47*, 2481. [CrossRef] [PubMed]
140. Hekman, M.C.H.; Rijpkema, M.; Aarntzen, E.H.; Mulder, S.F.; Langenhuijsen, J.F.; Oosterwijk, E.; Boerman, O.C.; Oyen, W.J.G.; Mulders, P.F.A. Positron Emission Tomography/Computed Tomography with ^{89}Zr-girentuximab Can Aid in Diagnostic Dilemmas of Clear Cell Renal Cell Carcinoma Suspicion. *Eur. Urol.* **2018**, *74*, 257–260. [CrossRef]
141. Joraku, A.; Hatano, K.; Kawai, K.; Kandori, S.; Kojima, T.; Fukumitsu, N.; Isobe, T.; Mori, Y.; Sakata, M.; Hara, T.; et al. Phase I/IIa PET imaging study with ^{89}zirconium labeled anti-PSMA minibody for urological malignancies. *Ann. Nucl. Med.* **2019**, *33*, 119–127. [CrossRef]
142. van Es, S.C.; Brouwers, A.H.; Mahesh, S.; Leliveld-Kors, A.M.; de Jong, I.J.; Lub-de Hooge, M.N.; de Vries, E.; Gietema, J.A.; Oosting, S.F. ^{89}Zr-Bevacizumab PET: Potential early indicator of everolimus efficacy in patients with metastatic renal cell carcinoma. *J. Nucl. Med.* **2017**, *58*, 905–910. [CrossRef]
143. Verhoeff, S.R.; van Es, S.C.; Boon, E.; van Helden, E.; Angus, L.; Elias, S.G.; Oosting, S.F.; Aarntzen, E.H.; Brouwers, A.H.; Kwee, T.C.; et al. Lesion detection by [^{89}Zr]Zr-DFO-girentuximab and [^{18}F]FDG-PET/CT in patients with newly diagnosed metastatic renal cell carcinoma. *Eur. J. Nucl. Med. Mol. Imaging* **2019**, *46*, 1931–1939. [CrossRef]
144. Gaykema, S.B.; Schröder, C.P.; Vitfell-Rasmussen, J.; Chua, S.; Oude Munnink, T.H.; Brouwers, A.H.; Bongaerts, A.H.; Akimov, M.; Fernandez-Ibarra, C.; Lub-de Hooge, M.N.; et al. 89Zr-trastuzumab and 89Zr-bevacizumab PET to evaluate the effect of the HSP90 inhibitor NVP-AUY922 in metastatic breast cancer patients. *Clin. Cancer Res.* **2014**, *20*, 3945–3954. [CrossRef]
145. Menke-van der Houven van Oordt, C.W.; McGeoch, A.; Bergstrom, M.; McSherry, I.; Smith, D.A.; Cleveland, M.; Al-Azzam, W.; Chen, L.; Verheul, H.; Hoekstra, O.S.; et al. Immuno-PET imaging to assess target engagement: Experience from ^{89}Zr-anti-HER3 mAb (GSK2849330) in patients with solid tumors. *J. Nucl. Med.* **2019**, *60*, 902–909. [CrossRef]
146. Bensch, F.; Lamberts, L.E.; Smeenk, M.M.; Jorritsma-Smit, A.; Lub-de Hooge, M.N.; Terwisscha van Scheltinga, A.; de Jong, J.R.; Gietema, J.A.; Schröder, C.P.; Thomas, M.; et al. ^{89}Zr-lumretuzumab PET imaging before and during HER3 antibody lumretuzumab treatment in patients with solid tumors. *Clin. Cancer Res.* **2017**, *23*, 6128–6137. [CrossRef]
147. Verhoeff, S.R.; van den Heuvel, M.M.; van Herpen, C.M.L.; Piet, B.; Aarntzen, E.H.J.G.; Heskamp, S. Programmed Cell Death-1/Ligand-1 PET Imaging: A Novel Tool to Optimize Immunotherapy? *PET Clin.* **2020**, *15*, 35–43. [CrossRef] [PubMed]

MIM Software Inc. v. Progenics Pharmaceuticals, Inc.
IPR2025-00630
Progenics EX2017

148. Niemeijer, A.N.; Leung, D.; Huisman, M.C.; Bahce, I.; Hoekstra, O.S.; van Dongen, G.A.M.S.; Boellaard, R.; Du, S.; Hayes, W.; Smith, R.; et al. Whole body PD-1 and PD-L1 positron emission tomography in patients with non-small-cell lung cancer. *Nat. Commun.* **2018**, *9*, 4664. [CrossRef] [PubMed]
149. Osborne, J.R.; Green, D.A.; Spratt, D.E.; Lyashchenko, S.; Fareedy, S.B.; Robinson, B.D.; Beattie, B.J.; Jain, M.; Lewis, J.S.; Christos, P.; et al. A prospective pilot study of (89)Zr-J591/prostate specific membrane antigen positron emission tomography in men with localized prostate cancer undergoing radical prostatectomy. *J. Urol.* **2014**, *191*, 1439–1445. [CrossRef]
150. Pandit-Taskar, N.; O'Donoghue, J.A.; Ruan, S.; Lyashchenko, S.K.; Carrasquillo, J.A.; Heller, G.; Martinez, D.F.; Cheal, S.M.; Lewis, J.S.; Fleisher, M.; et al. First-in-human imaging with 89Zr-Df-IAB2M anti-PSMA minibody in patients with metastatic prostate cancer: Pharmacokinetics, biodistribution, dosimetry, and lesion uptake. *J. Nucl. Med.* **2016**, *57*, 1858–1864. [CrossRef] [PubMed]
151. Pandit-Taskar, N.; Postow, M.A.; Hellmann, M.D.; Harding, J.J.; Barker, C.A.; O'Donoghue, J.A.; Ziolkowska, M.; Ruan, S.; Lyashchenko, S.K.; Tsai, F.; et al. First-in-humans imaging with ^{89}Zr-Df-IAB22M2C anti-CD8 minibody in patients with solid malignancies: Preliminary pharmacokinetics, biodistribution, and lesion targeting. *J. Nucl. Med.* **2020**, *61*, 512–519. [CrossRef] [PubMed]
152. O'Donoghue, J.A.; Danila, D.C.; Pandit-Taskar, N.; Beylergil, V.; Cheal, S.M.; Fleming, S.E.; Fox, J.J.; Ruan, S.; Zanzonico, P.B.; Ragupathi, G.; et al. Pharmacokinetics and biodistribution of a [^{89}Zr]Zr-DFO-MSTP2109A Anti-STEAP1 antibody in metastatic castration-resistant prostate cancer patients. *Mol. Pharm.* **2019**, *16*, 3083–3090. [CrossRef] [PubMed]
153. Bensch, F.; Brouwers, A.H.; Lub-de Hooge, M.N.; de Jong, J.R.; van der Vegt, B.; Sleijfer, S.; de Vries, E.; Schröder, C.P. ^{89}Zr-trastuzumab PET supports clinical decision making in breast cancer patients, when HER2 status cannot be determined by standard work up. *Eur. J. Nucl. Med. Mol. Imaging* **2018**, *45*, 2300–2306. [CrossRef]
154. Dehdashti, F.; Wu, N.; Bose, R.; Naughton, M.J.; Ma, C.X.; Marquez-Nostra, B.V.; Diebolder, P.; Mpoy, C.; Rogers, B.E.; Lapi, S.E.; et al. Evaluation of [^{89}Zr]trastuzumab-PET/CT in differentiating HER2-positive from HER2-negative breast cancer. *Breast Cancer Res. Treat.* **2018**, *169*, 523–530. [CrossRef]
155. Gebhart, G.; Lamberts, L.E.; Wimana, Z.; Garcia, C.; Emonts, P.; Ameye, L.; Stroobants, S.; Huizing, M.; Aftimos, P.; Tol, J.; et al. Molecular imaging as a tool to investigate heterogeneity of advanced HER2-positive breast cancer and to predict patient outcome under trastuzumab emtansine (T-DM1): The ZEPHIR trial. *Ann. Oncol. Off. J. Eur. Soc. Med. Oncol.* **2016**, *27*, 619–624. [CrossRef]
156. Ulaner, G.A.; Carrasquillo, J.A.; Riedl, C.C.; Yeh, R.; Hatzoglou, V.; Ross, D.S.; Jhaveri, K.; Chandarlapaty, S.; Hyman, D.M.; Zeglis, B.M.; et al. Identification of HER2-positive metastases in patients with HER2-negative primary breast cancer by using HER2-targeted ^{89}Zr-pertuzumab PET/CT. *Radiology* **2020**, *296*, 370–378. [CrossRef]
157. Ulaner, G.A.; Hyman, D.M.; Lyashchenko, S.K.; Lewis, J.S.; Carrasquillo, J.A. ^{89}Zr-trastuzumab PET/CT for detection of human epidermal growth factor receptor 2-positive metastases in patients with human epidermal growth factor receptor 2-negative primary breast cancer. *Clin. Nucl. Med.* **2017**, *42*, 912–917. [CrossRef] [PubMed]
158. Ulaner, G.A.; Lyashchenko, S.K.; Riedl, C.; Ruan, S.; Zanzonico, P.B.; Lake, D.; Jhaveri, K.; Zeglis, B.; Lewis, J.S.; O'Donoghue, J.A. First-in-human human epidermal growth factor receptor 2-targeted imaging using ^{89}Zr-pertuzumab PET/CT: Dosimetry and clinical application in patients with breast cancer. *J. Nucl. Med.* **2018**, *59*, 900–906. [CrossRef]
159. Heukelom, J.; Hamming, O.; Bartelink, H.; Hoebers, F.; Giralt, J.; Herlestam, T.; Verheij, M.; van den Brekel, M.; Vogel, W.; Slevin, N.; et al. Adaptive and innovative Radiation Treatment FOR improving Cancer treatment outcomE (ARTFORCE); a randomized controlled phase II trial for individualized treatment of head and neck cancer. *BMC Cancer* **2013**, *13*, 84. [CrossRef] [PubMed]
160. De Feo, M.S.; Pontico, M.; Frantellizzi, V.; Corica, F.; De Cristofaro, F.; De Vincentis, G. 89Zr-PET imaging in humans: A systematic review. *Clin. Transl. Imaging* **2022**, *10*, 23–36. [CrossRef]
161. van Loon, J.; Even, A.; Aerts, H.; Öllers, M.; Hoebers, F.; van Elmpt, W.; Dubois, L.; Dingemans, A.C.; Lalisang, R.I.; Kempers, P.; et al. PET imaging of zirconium-89 labeled cetuximab: A phase I trial in patients with head and neck and lung cancer. *Radiother. Oncol.* **2017**, *122*, 267–273. [CrossRef] [PubMed]
162. van Brummelen, E.; Huisman, M.C.; de Wit-van der Veen, L.J.; Nayak, T.K.; Stokkel, M.; Mulder, E.R.; Hoekstra, O.S.; Vugts, D.J.; Van Dongen, G.; Verheul, H.M.; et al. ^{89}Zr-labeled CEA-targeted IL-2 variant immunocytokine in patients with solid tumors: CEA-mediated tumor accumulation and role of IL-2 receptor-binding. *Oncotarget* **2018**, *9*, 24737–24749. [CrossRef] [PubMed]
163. Jalilian, A.R.; Osso, J., Jr. The current status and future of theranostic Copper-64 radiopharmaceuticals. *Iran. J. Nucl. Med.* **2017**, *25*, 1–10.
164. Pyo, A.; Yun, M.; Kim, H.S.; Kim, T.Y.; Lee, J.J.; Kim, J.Y.; Lee, S.; Kwon, S.Y.; Bom, H.S.; Kim, H.S.; et al. ^{64}Cu-Labeled Repebody Molecules for Imaging of Epidermal Growth Factor Receptor-Expressing Tumors. *J. Nucl. Med.* **2018**, *59*, 340–346. [CrossRef] [PubMed]
165. Zhou, Y.; Li, J.; Xu, X.; Zhao, M.; Zhang, B.; Deng, S.; Wu, Y. ^{64}Cu-based Radiopharmaceuticals in Molecular Imaging. *Technol. Cancer Res. Treat.* **2019**, *18*, 1533033819830758. [CrossRef]
166. Mccall, K.C.; Humm, J.L.; Bartlett, R.; Reese, M.; Carlin, S. Copper-64-diacetyl-bis (N(4)- methylthiosemicarbazone) pharmacokinetics in FaDu xenograft tumors and correlation with microscopic markers of hypoxia. *Int. J. Radiat. Oncol. Biol. Phys.* **2012**, *84*, e393–e399. [CrossRef]
167. Lopci, E.; Grassi, I.; Rubello, D.; Colletti, P.M.; Cambioli, S.; Gamboni, A.; Salvi, F.; Cicoria, G.; Lodi, F.; Dazzi, C.; et al. Prognostic evaluation of disease outcome in solid tumors investigated with 64Cu-ATSM PET/CT. *Clin. Nucl. Med.* **2016**, *41*, e87–e92. [CrossRef] [PubMed]

MIM Software Inc. v. Progenics Pharmaceuticals, Inc.
IPR2025-00630
Progenics EX2017

168. Grassi, I.; Nanni, C.; Cicoria, G.; Blasi, C.; Bunkheila, F.; Lopci, E.; Colletti, P.M.; Rubello, D.; Fanti, S. Usefulness of 64Cu-ATSM in head and neck cancer: A preliminary prospective study. *Clin. Nucl. Med.* **2014**, *39*, e59–e63. [CrossRef] [PubMed]
169. Lopci, E.; Grassi, I.; Chiti, A.; Nanni, C.; Cicoria, G.; Toschi, L.; Fonti, C.; Lodi, F.; Mattioli, S.; Fanti, S. PET radiopharmaceuticals for imaging of tumor hypoxia: A review of the evidence. *Am. J. Nucl. Med. Mol. Imaging* **2014**, *4*, 365–384.
170. Vázquez, M.C.; Martínez, P.; Alvarez, A.R.; González, M.; Zanlungo, S. Increased copper levels in in vitro and in vivo models of Niemann-Pick, C. disease. *Biometals* **2012**, *25*, 777–786. [CrossRef] [PubMed]
171. Smpokou, P.; Samanta, M.; Berry, G.T.; Hecht, L.; Engle, E.C.; Lichter-Konecki, U. Menkes disease in affected females: The clinical disease spectrum. *Am. J. Med. Genet. A* **2015**, *167A*, 417–420. [CrossRef] [PubMed]
172. Yoshii, Y.; Yoshimoto, M.; Matsumoto, H.; Furukawa, T.; Zhang, M.R.; Inubushi, M.; Tsuji, A.B.; Fujibayashi, Y.; Higashi, T.; Saga, T. ^{64}Cu-ATSM internal radiotherapy to treat tumors with bevacizumab-induced vascular decrease and hypoxia in human colon carcinoma xenografts. *Oncotarget* **2017**, *8*, 88815–88826. [CrossRef] [PubMed]
173. Yoshii, Y.; Furukawa, T.; Matsumoto, H.; Yoshimoto, M.; Kiyono, Y.; Zhang, M.R.; Fujibayashi, Y.; Saga, T. (64)Cu-ATSM therapy targets regions with activated DNA repair and enrichment of CD133 (+) cells in an HT-29 tumor model: Sensitization with a nucleic acid antimetabolite. *Cancer Lett.* **2016**, *376*, 74–82. [CrossRef]
174. Yoshii, Y.; Furukawa, T.; Kiyono, Y.; Watanabe, R.; Mori, T.; Yoshii, H.; Asai, T.; Okazawa, H.; Welch, M.J.; Fujibayashi, Y. Internal radiotherapy with copper-64-diacetyl-bis(N4 -methylthiosemicarbazone) reduces CD133+ highly tumorigenic cells and metastatic ability of mouse colon carcinoma. *Nucl. Med. Biol.* **2012**, *38*, 151–157. [CrossRef]
175. Meisenheimer, M.; Saenko, Y.; Eppard, E. Gallium-68: Radiolabeling of Radiopharmaceuticals for PET Imaging—A Lot to Consider. In *Medical Isotopes*; Naqvi, S.A.R., Imrani, M.B., Eds.; IntechOpen: London, UK, 2019. Available online: https://www.intechopen.com/chapters/70578 (accessed on 7 February 2022).
176. Jalilian, A.R. An overview on Ga-68 radiopharmaceuticals for positron emission tomography applications. *Iran. J. Nucl. Med.* **2016**, *24*, 1–10.
177. Lenzo, N.P.; Meyrick, D.; Turner, J.H. Review of Gallium-68 PSMA PET/CT imaging in the management of prostate cancer. *Diagnostics* **2018**, *8*, 16. [CrossRef]
178. Raj, N.; Reidy-Lagunes, D. The role of 68Ga-DOTATATE positron emission tomography/computed tomography in well-differentiated neuroendocrine tumors: A case-based approach illustrates potential benefits and challenges. *Pancreas* **2018**, *47*, 1–5. [CrossRef] [PubMed]
179. Jansen, T.; van Lith, S.; Boss, M.; Brom, M.; Joosten, L.; Béhé, M.; Buitinga, M.; Gotthardt, M. Exendin-4 analogs in insulinoma theranostics. *J. Label. Comp. Radiopharm.* **2019**, *62*, 656–672. [CrossRef] [PubMed]
180. Zhang, J.; Mao, F.; Niu, G.; Peng, L.; Lang, L.; Li, F.; Ying, H.; Wu, H.; Pan, B.; Zhu, Z.; et al. ^{68}Ga-BBN-RGD PET/CT for GRPR and integrin $\alpha_v\beta_3$ imaging in patients with breast cancer. *Theranostics* **2018**, *8*, 1121–1130. [CrossRef] [PubMed]
181. Zhang, J.; Li, D.; Lang, L.; Zhu, Z.; Wang, L.; Wu, P.; Niu, G.; Li, F.; Chen, X. 68Ga-NOTA-Aca-BBN(7-14) PET/CT in Healthy Volunteers and Glioma Patients. *J. Nucl. Med.* **2016**, *57*, 9–14. [CrossRef] [PubMed]
182. Velikyan, I.; Schweighöfer, P.; Feldwisch, J.; Seemann, J.; Frejd, F.Y.; Lindman, H.; Sörensen, J. Diagnostic HER2-binding radiopharmaceutical, [^{68}Ga]Ga-ABY-025, for routine clinical use in breast cancer patients. *Am. J. Nucl. Med. Mol. Imaging* **2019**, *9*, 12–23.
183. Djekidel, M.; Das, J.M. Nuclear Medicine Neuro PET Assessment, Protocols, and Interpretation. In *StatPearls*; StatPearls Publishing: Treasure Island, FL, USA, 2022. Available online: https://www.ncbi.nlm.nih.gov/books/NBK570591 (accessed on 28 March 2022).
184. Cybulska, K.; Perk, L.; Booij, J.; Laverman, P.; Rijpkema, M. Huntington's Disease: A Review of the Known PET Imaging Biomarkers and Targeting Radiotracers. *Molecules* **2020**, *25*, 482. [CrossRef]
185. Delva, A.; Van Weehaeghe, D.; Koole, M.; Van Laere, K.; Vandenberghe, W. Loss of presynaptic terminal integrity in the substantia nigra in early parkinson's disease. *Mov. Disord.* **2020**, *35*, 1977–1986. [CrossRef]
186. Xiong, M.; Roshanbin, S.; Rokka, J.; Schlein, E.; Ingelsson, M.; Sehlin, D.; Eriksson, J.; Syvänen, S. In vivo imaging of synaptic density with [^{11}C]UCB-J PET in two mouse models of neurodegenerative disease. *Neuroimage* **2021**, *239*, 118302. [CrossRef]
187. Borja, A.J.; Hancin, E.C.; Raynor, W.Y.; Ayubcha, C.; Detchou, D.K.; Werner, T.J.; Revheim, M.E.; Alavi, A. A Critical Review of PET Tracers Used for Brain Tumor Imaging. *PET Clin.* **2021**, *16*, 219–231. [CrossRef]
188. Minoshima, S.; Mosci, K.; Cross, D.; Thientunyakit, T. Brain [F-18]FDG PET for Clinical Dementia Workup: Differential Diagnosis of Alzheimer's Disease and Other Types of Dementing Disorders. *Semin. Nucl. Med.* **2021**, *51*, 230–240. [CrossRef]
189. Chételat, G.; Arbizu, J.; Barthel, H.; Garibotto, V.; Law, I.; Morbelli, S.; van de Giessen, E.; Agosta, F.; Barkhof, F.; Brooks, D.J.; et al. Amyloid-PET and 18F-FDG-PET in the diagnostic investigation of Alzheimer's disease and other dementias. *Lancet Neurol.* **2020**, *19*, 951–962. [CrossRef]
190. Blazhenets, G.; Frings, L.; Ma, Y.; Sörensen, A.; Eidelberg, D.; Wiltfang, J.; Meyer, P.T. Alzheimer's Disease Neuroimaging Initiative. Validation of the Alzheimer Disease Dementia Conversion-Related Pattern as an ATN Biomarker of Neurodegeneration. *Neurology* **2021**, *96*, e1358–e1368. [CrossRef] [PubMed]
191. Minoshima, S.; Drzezga, A.E.; Barthel, H.; Bohnen, N.; Djekidel, M.; Lewis, D.H.; Mathis, C.A.; McConathy, J.; Nordberg, A.; Sabri, O.; et al. SNMMI Procedure Standard/EANM Practice Guideline for Amyloid PET Imaging of the Brain 1.0. *J. Nucl. Med.* **2016**, *57*, 1316–1322. [CrossRef] [PubMed]

MIM Software Inc. v. Progenics Pharmaceuticals, Inc.
IPR2025-00630
Progenics EX2017

192. Yap, S.Y.; Frias, B.; Wren, M.C.; Schöll, M.; Fox, N.C.; Årstad, E.; Lashley, T.; Sander, K. Discriminatory ability of next-generation tau PET tracers for Alzheimer's disease. *Brain* **2021**, *144*, 2284–2290. [CrossRef] [PubMed]
193. Leuzy, A.; Chiotis, K.; Lemoine, L.; Gillberg, P.G.; Almkvist, O.; Rodriguez-Vieitez, E.; Nordberg, A. Tau PET imaging in neurodegenerative tauopathies-still a challenge. *Mol. Psychiatry* **2019**, *24*, 1112–1134. [CrossRef]
194. Rabinovici, G.D.; Gatsonis, C.; Apgar, C.; Chaudhary, K.; Gareen, I.; Hanna, L.; Hendrix, J.; Hillner, B.E.; Olson, C.; Lesman-Segev, O.H.; et al. Association of Amyloid Positron Emission Tomography with Subsequent Change in Clinical Management Among Medicare Beneficiaries with Mild Cognitive Impairment or Dementia. *JAMA* **2019**, *321*, 1286–1294. [CrossRef]
195. Sood, A.; Shukla, J.; Shree, R.; Vatsa, R.; Modi, M.; Mittal, B.R. Comparative Performance of 99mTc-TRODAT-1 SPECT/CT and 18F-FDOPA PET/CT Imaging in Patients with Parkinson's Disease, Parkinson-Plus Syndrome, and Essential Tremor. *Clin. Nucl. Med.* **2021**, *46*, 95–102. [CrossRef]
196. Ni, R.; Nitsch, R.M. Recent Developments in Positron Emission Tomography Tracers for Proteinopathies Imaging in Dementia. *Front. Aging Neurosci.* **2022**, *13*, 751897. [CrossRef]
197. Pietroboni, A.M.; Colombi, A.; Carandini, T.; Sacchi, L.; Fenoglio, C.; Marotta, G.; Arighi, A.; De Riz, M.A.; Fumagalli, G.G.; Castellani, M.; et al. Amyloid PET imaging and dementias: Potential applications in detecting and quantifying early white matter damage. *Alzheimers Res. Ther.* **2022**, *14*, 33. [CrossRef]
198. Cselényi, Z.; Jönhagen, M.E.; Forsberg, A.; Halldin, C.; Julin, P.; Schou, M.; Johnström, P.; Varnäs, K.; Svensson, S.; Farde, L. Clinical validation of 18F-AZD4694, an amyloid-β-specific PET radioligand. *J. Nucl. Med.* **2012**, *53*, 415–424. [CrossRef]
199. Rodriguez-Vieitez, E.; Ni, R.; Gulyas, B.; Toth, M.; Haggkvist, J.; Halldin, C.; Voytenko, L.; Marutle, A.; Nordberg, A. Astrocytosis precedes amyloid plaque deposition in Alzheimer APPswe transgenic mouse brain: A correlative positron emission tomography and in vitro imaging study. *Eur. J. Nucl. Med. Mol. Imaging* **2015**, *42*, 1119–1132. [CrossRef] [PubMed]
200. Sehlin, D.; Fang, X.T.; Cato, L.; Antoni, G.; Lannfelt, L.; Syvanen, S. Antibody-based PET imaging of amyloid beta in mouse models of Alzheimer's disease. *Nat. Commun.* **2016**, *7*, 10759. [CrossRef] [PubMed]
201. Grimmer, T.; Shi, K.; Diehl-Schmid, J.; Natale, B.; Drzezga, A.; Förster, S.; Förstl, H.; Schwaiger, M.; Yakushev, I.; Wester, H.J.; et al. ^{18}F-FIBT may expand PET for β-amyloid imaging in neurodegenerative diseases. *Mol. Psychiatry* **2020**, *25*, 2608–2619. [CrossRef] [PubMed]
202. Meier, S.R.; Sehlin, D.; Roshanbin, S.; Falk, V.L.; Saito, T.; Saido, T.C.; Neumann, U.; Rokka, J.; Eriksson, J.; Syvänen, S. ^{11}C-PIB and ^{124}I-antibody PET provide differing estimates of brain amyloid-beta after therapeutic intervention. *J. Nucl. Med.* **2021**, *63*, 302–309. [CrossRef]
203. Ni, R. Positron emission tomography in animal models of Alzheimer's disease amyloidosis: Translational implications. *Pharmaceuticals* **2021**, *14*, 1179. [CrossRef] [PubMed]
204. Curtis, C.; Gamez, J.E.; Singh, U.; Sadowsky, C.H.; Villena, T.; Sabbagh, M.N.; Beach, T.G.; Duara, R.; Fleisher, A.S.; Frey, K.A.; et al. Phase 3 trial of flutemetamol labeled with radioactive fluorine 18 imaging and neuritic plaque density. *JAMA Neurol.* **2015**, *72*, 287–294. [CrossRef] [PubMed]
205. Sabri, O.; Sabbagh, M.N.; Seibyl, J.; Barthel, H.; Akatsu, H.; Ouchi, Y.; Senda, K.; Murayama, S.; Ishii, K.; Takao, M.; et al. Florbetaben PET imaging to detect amyloid beta plaques in Alzheimer's disease: Phase 3 study. *Alzheimers Dement.* **2015**, *11*, 964–974. [CrossRef]
206. Jack, C.R., Jr.; Bennett, D.A.; Blennow, K.; Carrillo, M.C.; Dunn, B.; Haeberlein, S.B.; Holtzman, D.M.; Jagust, W.; Jessen, F.; Karlawish, J.; et al. NIA-AA Research Framework: Toward a biological definition of Alzheimer's disease. *Alzheimers Dement.* **2018**, *14*, 535–562. [CrossRef]
207. Wolk, D.A.; Sadowsky, C.; Safirstein, B.; Rinne, J.O.; Duara, R.; Perry, R.; Agronin, M.; Gamez, J.; Shi, J.; Ivanoiu, A.; et al. Use of flutemetamol F 18-labeled positron emission tomography and other biomarkers to assess risk of clinical progression in patients with amnestic mild cognitive impairment. *JAMA Neurol.* **2018**, *75*, 1114–1123. [CrossRef]
208. Cotta Ramusino, M.; Perini, G.; Altomare, D.; Barbarino, P.; Weidner, W.; Salvini Porro, G.; Barkhof, F.; Rabinovici, G.D.; van der Flier, W.M.; Frisoni, G.B.; et al. Outcomes of clinical utility in amyloid-PET studies: State of art and future perspectives. *Eur. J. Nucl. Med. Mol. Imaging* **2021**, *48*, 2157–2168. [CrossRef]
209. Ito, H.; Shinotoh, H.; Shimada, H.; Miyoshi, M.; Yanai, K.; Okamura, N.; Takano, H.; Takahashi, H.; Arakawa, R.; Kodaka, F.; et al. Imaging of amyloid deposition in human brain using positron emission tomography and [^{18}F]FACT: Comparison with [^{11}C]PIB. *Eur. J. Nucl. Med. Mol. Imaging* **2014**, *41*, 745–754. [CrossRef] [PubMed]
210. Xiao, H.; Choi, S.R.; Zhao, R.; Ploessl, K.; Alexoff, D.; Zhu, L.; Zha, Z.; Kung, H.F. A new highly deuterated [^{18}F]AV-45, [^{18}F]D15FSP, for imaging β-Amyloid plaques in the brain. *ACS Med. Chem. Lett.* **2021**, *12*, 1086–1092. [CrossRef] [PubMed]
211. Sundaram, G.S.; Dhavale, D.D.; Prior, J.L.; Yan, P.; Cirrito, J.; Rath, N.P.; Laforest, R.; Cairns, N.J.; Lee, J.M.; Kotzbauer, P.T.; et al. Fluselenamyl: A novel benzoselenazole derivative for PET detection of amyloid plaques (Aβ) in Alzheimer's disease. *Sci. Rep.* **2016**, *6*, 35636. [CrossRef]
212. Hooker, J.M.; Carson, R.E. Human Positron Emission Tomography Neuroimaging. *Annu. Rev. Biomed. Eng.* **2019**, *21*, 551–581. [CrossRef] [PubMed]
213. Parker, C.A.; Gunn, R.N.; Rabiner, E.A.; Slifstein, M.; Comley, R.; Salinas, C.; Johnson, C.N.; Jakobsen, S.; Houle, S.; Laruelle, M.; et al. Radiosynthesis and characterization of 11C-GSK215083 as a PET radioligand for the 5-HT 6 receptor. *J. Nucl. Med.* **2012**, *53*, 295–303. [CrossRef] [PubMed]

MIM Software Inc. v. Progenics Pharmaceuticals, Inc.
IPR2025-00630
Progenics EX2017

214. Parker, C.A.; Rabiner, E.A.; Gunn, R.N.; Searle, G.; Martarello, L.; Comley, R.A.; Davy, M.; Wilson, A.A.; Houle, S.; Mizrahi, R.; et al. Human kinetic modeling of the 5HT6 PET radioligand 11C-GSK215083 and its utility for determining occupancy at both 5HT6 and 5HT2A receptors by SB742457 as a potential therapeutic mechanism of action in Alzheimer disease. *J. Nucl. Med.* **2015**, *56*, 1901–1909. [CrossRef]
215. Quiroz, Y.T.; Sperling, R.A.; Norton, D.J.; Baena, A.; Arboleda-Velasquez, J.F.; Cosio, D.; Schultz, A.; Lapoint, M.; Guzman-Velez, E.; Miller, J.B.; et al. Association between amyloid and tau accumulation in young adults with autosomal dominant Alzheimer disease. *JAMA Neurol.* **2018**, *75*, 548–556. [CrossRef]
216. Harada, R.; Okamura, N.; Furumoto, S.; Yanai, K. Imaging Protein Misfolding in the Brain Using β-Sheet Ligands. *Front. Neurosci.* **2018**, *12*, 585. [CrossRef]
217. Saint-Aubert, L.; Lemoine, L.; Chiotis, K.; Leuzy, A.; Rodriguez-Vieitez, E.; Nordberg, A. Tau PET imaging: Present and future directions. *Mol. Neurodegener.* **2017**, *12*, 19. [CrossRef]
218. Chien, D.T.; Szardenings, A.K.; Bahri, S.; Walsh, J.C.; Mu, F.; Xia, C.; Shankle, W.R.; Lerner, A.J.; Su, M.Y.; Elizarov, A.; et al. Early clinical PET imaging results with the novel PHF-tau radioligand [F-18]-T807. *J. Alzheimers Dis.* **2013**, *34*, 457–468. [CrossRef]
219. Hostetler, E.D.; Walji, A.M.; Zeng, Z.; Miller, P.; Bennacef, I.; Salinas, C.; Connolly, B.; Gantert, L.; Haley, H.; Holahan, M.; et al. Preclinical characterization of 18F-MK-6240, a promising PET tracer for in vivo quantification of human neurofibrillary tangles. *J. Nucl. Med.* **2016**, *57*, 1599–1606. [CrossRef]
220. Devous, M.D., Sr.; Joshi, A.D.; Navitsky, M.; Southekal, S.; Pontecorvo, M.J.; Shen, H.; Lu, M.; Shankle, W.R.; Seibyl, J.P.; Marek, K.; et al. Test-retest reproducibility for the tau PET imaging agent flortaucipir F 18. *J. Nucl. Med.* **2017**, *59*, 937–943. [CrossRef] [PubMed]
221. Wooten, D.W.; Guehl, N.J.; Verwer, E.E.; Shoup, T.M.; Yokell, D.L.; Zubcevik, N.; Vasdev, N.; Zafonte, R.D.; Johnson, K.A.; El Fakhri, G.; et al. Pharmacokinetic evaluation of the tau PET radiotracer ^{18}F-T807 (^{18}F-AV-1451) in human subjects. *J. Nucl. Med.* **2017**, *58*, 484–491. [CrossRef] [PubMed]
222. Johnson, K.A.; Schultz, A.; Betensky, R.A.; Becker, J.A.; Sepulcre, J.; Rentz, D.; Mormino, E.; Chhatwal, J.; Amariglio, R.; Papp, K.; et al. Tau positron emission tomographic imaging in aging and early Alzheimer disease. *Ann. Neurol.* **2016**, *79*, 110–119. [CrossRef] [PubMed]
223. Zhang, W.; Arteaga, J.; Cashion, D.K.; Chen, G.; Gangadharmath, U.; Gomez, L.F.; Kasi, D.; Lam, C.; Liang, Q.; Liu, C.; et al. A highly selective and specific PET tracer for imaging of tau pathologies. *J. Alzheimers Dis.* **2012**, *31*, 601–612. [CrossRef]
224. Schonhaut, D.R.; McMillan, C.T.; Spina, S.; Dickerson, B.C.; Siderowf, A.; Devous, M.D., Sr.; Tsai, R.; Winer, J.; Russell, D.S.; Litvan, I.; et al. ^{18}F-flortaucipir tau positron emission tomography distinguishes established progressive supranuclear palsy from controls and Parkinson disease: A multicenter study. *Ann. Neurol.* **2017**, *82*, 622–634. [CrossRef]
225. Smith, R.; Schöll, M.; Londos, E.; Ohlsson, T.; Hansson, O. ^{18}F-AV-1451 in Parkinson's disease with and without dementia and in dementia with Lewy bodies. *Sci. Rep.* **2018**, *8*, 4717. [CrossRef]
226. Schöll, M.; Lockhart, S.N.; Schonhaut, D.R.; O'Neil, J.P.; Janabi, M.; Ossenkoppele, R.; Baker, S.L.; Vogel, J.W.; Faria, J.; Schwimmer, H.D.; et al. PET imaging of tau deposition in the aging human brain. *Neuron* **2016**, *89*, 971–982. [CrossRef]
227. Ossenkoppele, R.; Schonhaut, D.R.; Schöll, M.; Lockhart, S.N.; Ayakta, N.; Baker, S.L.; O'Neil, J.P.; Janabi, M.; Lazaris, A.; Cantwell, A.; et al. Tau PET patterns mirror clinical and neuroanatomical variability in Alzheimer's disease. *Brain* **2016**, *139*, 1551–1567. [CrossRef]
228. Cho, H.; Choi, J.Y.; Hwang, M.S.; Lee, J.H.; Kim, Y.J.; Lee, H.M.; Lyoo, C.H.; Ryu, Y.H.; Lee, M.S. Tau PET in Alzheimer disease and mild cognitive impairment. *Neurology* **2016**, *87*, 375–383. [CrossRef]
229. Bejanin, A.; Schonhaut, D.R.; La Joie, R.; Kramer, J.H.; Baker, S.L.; Sosa, N.; Ayakta, N.; Cantwell, A.; Janabi, M.; Lauriola, M.; et al. Tau pathology and neurodegeneration contribute to cognitive impairment in Alzheimer's disease. *Brain* **2017**, *140*, 3286–3300. [CrossRef] [PubMed]
230. Marquié, M.; Normandin, M.D.; Meltzer, A.C.; Siao Tick Chong, M.; Andrea, N.V.; Antón-Fernández, A.; Klunk, W.E.; Mathis, C.A.; Ikonomovic, M.D.; Debnath, M.; et al. Pathological correlations of [F-18]-AV-1451 imaging in non-alzheimer tauopathies. *Ann. Neurol.* **2017**, *81*, 117–128. [CrossRef] [PubMed]
231. Choi, J.Y.; Cho, H.; Ahn, S.J.; Lee, J.H.; Ryu, Y.H.; Lee, M.S.; Lyoo, C.H. Off-target ^{18}F-AV-1451 binding in the basal ganglia correlates with age-related iron accumulation. *J. Nucl. Med.* **2018**, *59*, 117–120. [CrossRef]
232. Vermeiren, C.; Motte, P.; Viot, D.; Mairet-Coello, G.; Courade, J.P.; Citron, M.; Mercier, J.; Hannestad, J.; Gillard, M. The tau positron-emission tomography tracer AV-1451 binds with similar affinities to tau fibrils and monoamine oxidases. *Mov. Disord.* **2018**, *33*, 273–281. [CrossRef] [PubMed]
233. Smith, R.; Schöll, M.; Honer, M.; Nilsson, C.F.; Englund, E.; Hansson, O. Tau neuropathology correlates with FDG-PET, but not AV-1451-PET, in progressive supranuclear palsy. *Acta Neuropathol.* **2017**, *133*, 149–151. [CrossRef] [PubMed]
234. Lowe, V.J.; Curran, G.; Fang, P.; Liesinger, A.M.; Josephs, K.A.; Parisi, J.E.; Kantarci, K.; Boeve, B.F.; Pandey, M.K.; Bruinsma, T.; et al. An autoradiographic evaluation of AV-1451 Tau PET in dementia. *Acta Neuropathol. Commun.* **2016**, *4*, 58. [CrossRef]
235. Sander, K.; Lashley, T.; Gami, P.; Gendron, T.; Lythgoe, M.F.; Rohrer, J.D.; Schott, J.M.; Revesz, T.; Fox, N.C.; Årstad, E. Characterization of tau positron emission tomography tracer [^{18}F]AV-1451 binding to postmortem tissue in Alzheimer's disease, primary tauopathies, and other dementias. *Alzheimers Dement.* **2016**, *12*, 1116–1124. [CrossRef]

MIM Software Inc. v. Progenics Pharmaceuticals, Inc.
IPR2025-00630
Progenics EX2017

236. Villemagne, V.L.; Furumoto, S.; Fodero-Tavoletti, M.T.; Mulligan, R.S.; Hodges, J.; Harada, R.; Yates, P.; Piguet, O.; Pejoska, S.; Doré, V.; et al. In vivo evaluation of a novel tau imaging tracer for Alzheimer's disease. *Eur. J. Nucl. Med. Mol. Imaging* **2014**, *41*, 816–826. [CrossRef]
237. Li, Y.; Tsui, W.; Rusinek, H.; Butler, T.; Mosconi, L.; Pirraglia, E.; Mozley, D.; Vallabhajosula, S.; Harada, R.; Furumoto, S.; et al. Cortical laminar binding of PET amyloid and tau tracers in Alzheimer disease. *J. Nucl. Med.* **2015**, *56*, 270–273. [CrossRef]
238. Jonasson, M.; Wall, A.; Chiotis, K.; Saint-Aubert, L.; Wilking, H.; Sprycha, M.; Borg, B.; Thibblin, A.; Eriksson, J.; Sörensen, J.; et al. Tracer kinetic analysis of (S)-^{18}F-THK5117 as a PET tracer for assessing tau pathology. *J. Nucl. Med.* **2016**, *57*, 574–581. [CrossRef]
239. Harada, R.; Okamura, N.; Furumoto, S.; Furukawa, K.; Ishiki, A.; Tomita, N.; Tago, T.; Hiraoka, K.; Watanuki, S.; Shidahara, M.; et al. 18F-THK5351: A novel PET radiotracer for imaging neurofibrillary pathology in Alzheimer disease. *J. Nucl. Med.* **2016**, *57*, 208–214. [CrossRef] [PubMed]
240. Ishiki, A.; Okamura, N.; Furukawa, K.; Furumoto, S.; Harada, R.; Tomita, N.; Hiraoka, K.; Watanuki, S.; Ishikawa, Y.; Tago, T.; et al. Longitudinal assessment of tau pathology in patients with Alzheimer's disease using [^{18}F]THK-5117 positron emission tomography. *PLoS ONE* **2015**, *10*, e0140311. [CrossRef] [PubMed]
241. Chiotis, K.; Saint-Aubert, L.; Savitcheva, I.; Jelic, V.; Andersen, P.; Jonasson, M.; Eriksson, J.; Lubberink, M.; Almkvist, O.; Wall, A.; et al. Imaging in-vivo tau pathology in Alzheimer's disease with THK5317 PET in a multimodal paradigm. *Eur. J. Nucl. Med. Mol. Imaging* **2016**, *43*, 1686–1699. [CrossRef]
242. Sone, D.; Imabayashi, E.; Maikusa, N.; Okamura, N.; Furumoto, S.; Kudo, Y.; Ogawa, M.; Takano, H.; Yokoi, Y.; Sakata, M.; et al. Regional tau deposition and subregion atrophy of medial temporal structures in early Alzheimer's disease: A combined positron emission tomography/magnetic resonance imaging study. *Alzheimer's Dement.* **2017**, *9*, 35–40. [CrossRef]
243. Okamura, N.; Furumoto, S.; Harada, R.; Tago, T.; Yoshikawa, T.; Fodero-Tavoletti, M.; Mulligan, R.S.; Villemagne, V.L.; Akatsu, H.; Yamamoto, T.; et al. Novel 18F-labeled arylquinoline derivatives for noninvasive imaging of tau pathology in Alzheimer disease. *J. Nucl. Med.* **2013**, *54*, 1420–1427. [CrossRef] [PubMed]
244. Honer, M.; Gobbi, L.; Knust, H.; Kuwabara, H.; Muri, D.; Koerner, M.; Valentine, H.; Dannals, R.F.; Wong, D.F.; Borroni, E. Preclinical evaluation of ^{18}F-RO6958948, ^{11}C-RO6931643, and ^{11}C-RO6924963 as novel PET radiotracers for imaging tau aggregates in Alzheimer disease. *J. Nucl. Med.* **2018**, *59*, 675–681. [CrossRef] [PubMed]
245. Harada, R.; Ishiki, A.; Kai, H.; Sato, N.; Furukawa, K.; Furumoto, S.; Tago, T.; Tomita, N.; Watanuki, S.; Hiraoka, K.; et al. Correlations of ^{18}F-THK5351 PET with post-mortem burden of tau and astrogliosis in Alzheimer's disease. *J. Nucl. Med.* **2017**, *59*, 671–674. [CrossRef]
246. Wong, D.F.; Comley, R.A.; Kuwabara, H.; Rosenberg, P.B.; Resnick, S.M.; Ostrowitzki, S.; Vozzi, C.; Boess, F.; Oh, E.; Lyketsos, C.G.; et al. First in-human PET study of 3 novel tau radiopharmaceuticals: [^{11}C]RO6924963, [^{11}C]RO6931643, and [^{18}F]RO6958948. *J. Nucl. Med.* **2018**, *59*, 1869–1876. [CrossRef]
247. Xia, C.F.; Arteaga, J.; Chen, G.; Gangadharmath, U.; Gomez, L.F.; Kasi, D.; Lam, C.; Liang, Q.; Liu, C.; Mocharla, V.P.; et al. [(18F)]T807, a novel tau positron emission tomography imaging agent for Alzheimer's disease. *Alzheimers Dement.* **2013**, *9*, 666–676. [CrossRef]
248. Betthauser, T.J.; Lao, P.J.; Murali, D.; Barnhart, T.E.; Furumoto, S.; Okamura, N.; Stone, C.K.; Johnson, S.C.; Christian, B.T. In vivo comparison of tau radioligands ^{18}F-THK-5351 and ^{18}F-THK-5317. *J Nucl. Med.* **2017**, *58*, 996–1002. [CrossRef]
249. Dupont, A.C.; Largeau, B.; Guilloteau, D.; Santiago Ribeiro, M.J.; Arlicot, N. The Place of PET to assess new therapeutic effectiveness in neurodegenerative diseases. *Contrast Media Mol. Imaging* **2018**, *2018*, 7043578. [CrossRef] [PubMed]
250. Roy, R.; Niccolini, F.; Pagano, G.; Politis, M. Cholinergic imaging in dementia spectrum disorders. *Eur. J. Nucl. Med. Mol. Imaging* **2016**, *43*, 1376–1386. [CrossRef] [PubMed]
251. Mueller, A.; Kroth, H.; Berndt, M.; Capotosti, F.; Molette, J.; Schieferstein, H.; Oden, F.; Juergens, T.; Darmency, V.; Schmitt-Willich, H.; et al. Characterization of the novel PET tracer PI-2620 for the assessment of Tau pathology in Alzheimer's disease and other tauopathies. *J. Nucl. Med.* **2017**, *58*, 847.
252. Li, C.; Götz, J. Tau-based therapies in neurodegeneration: Opportunities and challenges. *Nat. Rev. Drug Discov.* **2017**, *16*, 863–883. [CrossRef] [PubMed]
253. Müller, M.L.T.M.; Bohnen, N.I. Cholinergic dysfunction in Parkinson's disease. *Curr. Neurol. Neurosci. Rep.* **2013**, *13*, 377. [CrossRef]
254. Schmitz, T.W.; Spreng, R.N. Alzheimer's Disease Neuroimaging Initiative. Basal forebrain degeneration precedes and predicts the cortical spread of Alzheimer's pathology. *Nat. Commun.* **2016**, *7*, 13249. [CrossRef]
255. Butler, T.; Harvey, P.; Deshpande, A.; Tanzi, E.; Li, Y.; Tsui, W.; Silver, C.; Fischer, E.; Wang, X.; Chen, J.; et al. Basal forebrain septal nuclei are enlarged in healthy subjects prior to the development of Alzheimer's disease. *Neurobiol. Aging* **2018**, *65*, 201–205. [CrossRef]
256. Bohnen, N.I.; Grothe, M.J.; Ray, N.J.; Müller, M.; Teipel, S.J. Recent advances in cholinergic imaging and cognitive decline—Revisiting the cholinergic hypothesis of dementia. *Curr. Geriatr. Rep.* **2018**, *7*, 1–11. [CrossRef]
257. Mazère, J.; Lamare, F.; Allard, M.; Fernandez, P.; Mayo, W. 123I-Iodobenzovesamicol SPECT imaging of cholinergic systems in dementia with Lewy bodies. *J. Nucl. Med.* **2017**, *58*, 123–128. [CrossRef]
258. Horti, A.G. Development of [(18)F]ASEM, a specific radiotracer for quantification of the α7-nAChR with positron-emission tomography. *Biochem. Pharmacol.* **2015**, *97*, 566–575. [CrossRef]

MIM Software Inc. v. Progenics Pharmaceuticals, Inc.
IPR2025-00630
Progenics EX2017

259. Horti, A.G.; Gao, Y.; Kuwabara, H.; Wang, Y.; Abazyan, S.; Yasuda, R.P.; Tran, T.; Xiao, Y.; Sahibzada, N.; Holt, D.P.; et al. 18F-ASEM, a radiolabeled antagonist for imaging the 7-nicotinic acetylcholine receptor with PET. *J. Nucl. Med.* **2014**, *55*, 672–677. [CrossRef] [PubMed]
260. Petrou, M.; Frey, K.A.; Kilbourn, M.R.; Scott, P.J.; Raffel, D.M.; Bohnen, N.I.; Müller, M.L.; Albin, R.L.; Koeppe, R.A. In vivo imaging of human cholinergic nerve terminals with (-)-5-(18)F-fluoroethoxybenzovesamicol: Biodistribution, dosimetry, and tracer kinetic analyses. *J. Nucl. Med.* **2014**, *55*, 396–404. [CrossRef]
261. Hillmer, A.T.; Li, S.; Zheng, M.Q.; Scheunemann, M.; Lin, S.F.; Nabulsi, N.; Holden, D.; Pracitto, R.; Labaree, D.; Ropchan, J.; et al. PET imaging of α_7 nicotinic acetylcholine receptors: A comparative study of [^{18}F]ASEM and [^{18}F]DBT-10 in nonhuman primates, and further evaluation of [^{18}F]ASEM in humans. *Eur. J. Nucl. Med. Mol. Imaging* **2017**, *44*, 1042–1050. [CrossRef] [PubMed]
262. Gao, Y.; Kellar, K.J.; Yasuda, R.P.; Tran, T.; Xiao, Y.; Dannals, R.F.; Horti, A.G. Derivatives of dibenzothiophene for positron emission tomography imaging of α7-nicotinic acetylcholine receptors. *J. Med. Chem.* **2013**, *56*, 7574–7589. [CrossRef]
263. Tu, Z.; Zhang, X.; Jin, H.; Yue, X.; Padakanti, P.K.; Yu, L.; Liu, H.; Flores, H.P.; Kaneshige, K.; Parsons, S.M.; et al. Synthesis and biological characterization of a promising F-18 PET tracer for vesicular acetylcholine transporter. *Bioorg. Med. Chem.* **2015**, *23*, 4699–4709. [CrossRef]
264. Jin, H.; Yue, X.; Liu, H.; Han, J.; Flores, H.; Su, Y.; Parsons, S.M.; Perlmutter, J.S.; Tu, Z. Kinetic modeling of [^{18}F]VAT, a novel radioligand for positron emission tomography imaging vesicular acetylcholine transporter in non-human primate brain. *J. Neurochem.* **2018**, *144*, 791–804. [CrossRef] [PubMed]
265. Ogawa, K.; Shiba, K. In vivo and in vitro characteristics of radiolabeled vesamicol analogs as the vesicular acetylcholine transporter imaging agents. *Contrast Media Mol. Imaging* **2018**, *2018*, 4535476. [CrossRef] [PubMed]
266. Aghourian, M.; Legault-Denis, C.; Soucy, J.P.; Rosa-Neto, P.; Gauthier, S.; Kostikov, A.; Gravel, P.; Bédard, M.A. Quantification of brain cholinergic denervation in Alzheimer's disease using PET imaging with [^{18}F]-FEOBV. *Mol. Psychiatry* **2017**, *22*, 1531–1538. [CrossRef]
267. Wong, D.F.; Kuwabara, H.; Horti, A.G.; Roberts, J.M.; Nandi, A.; Cascella, N.; Brasic, J.; Weerts, E.M.; Kitzmiller, K.; Phan, J.A.; et al. Brain PET imaging of α7-nAChR with [^{18}F]ASEM:reproducibility, occupancy, receptor density, and changes in schizophrenia. *Int. J. Neuropsychopharmacol.* **2018**, *21*, 656–667. [CrossRef]
268. Van Waarde, A.; Dierckx, R.; Zhou, X.; Khanapur, S.; Tsukada, H.; Ishiwata, K.; Luurtsema, G.; de Vries, E.; Elsinga, P.H. Potential therapeutic applications of adenosine A_{2A} receptor ligands and opportunities for A_{2A} receptor imaging. *Med. Res. Rev.* **2018**, *38*, 5–56. [CrossRef]
269. Takata, K.; Kato, H.; Shimosegawa, E.; Okuno, T.; Koda, T.; Sugimoto, T.; Mochizuki, H.; Hatazawa, J.; Nakatsuji, Y. 11C-Acetate PET Imaging in Patients with Multiple Sclerosis. *PLoS ONE* **2014**, *9*, e111598. [CrossRef] [PubMed]
270. McCluskey, S.P.; Plisson, C.; Rabiner, E.A.; Howes, O. Advances in CNS PET: The state-of-the-art for new imaging targets for pathophysiology and drug development. *Eur. J. Nucl. Med. Mol. Imaging* **2020**, *47*, 451–489. [CrossRef] [PubMed]
271. Barret, O.; Hannestad, J.; Vala, C.; Alagille, D.; Tavares, A.; Laruelle, M.; Jennings, D.; Marek, K.; Russell, D.; Seibyl, J.; et al. Characterization in humans of 18F-MNI-444, a PET radiotracer for brain adenosine 2A receptors. *J. Nucl. Med.* **2015**, *56*, 586–591. [CrossRef] [PubMed]
272. Barret, O.; Hannestad, J.; Alagille, D.; Vala, C.; Tavares, A.; Papin, C.; Morley, T.; Fowles, K.; Lee, H.; Seibyl, J.; et al. Adenosine 2A receptor occupancy by tozadenant and preladenant in rhesus monkeys. *J. Nucl. Med.* **2014**, *55*, 1712–1718. [CrossRef]
273. Radhakrishnan, R.; Skosnik, P.D.; Ranganathan, M.; Naganawa, M.; Toyonaga, T.; Finnema, S.; Hillmer, A.T.; Esterlis, I.; Huang, Y.; Nabulsi, N.; et al. In vivo evidence of lower synaptic vesicle density in schizophrenia. *Mol. Psychiatry* **2021**, *26*, 7690–7698. [CrossRef]
274. Mercier, J.; Archen, L.; Bollu, V.; Carré, S.; Evrard, Y.; Jnoff, E.; Kenda, B.; Lallemand, B.; Michel, P.; Montel, F.; et al. Discovery of heterocyclic nonacetamide synaptic vesicle protein 2A (SV2A) ligands with single-digit nanomolar potency: Opening avenues towards the first SV2A positron emission tomography (PET) ligands. *ChemMedChem* **2014**, *9*, 693–698. [CrossRef]
275. Koole, M.; van Aalst, J.; Devrome, M.; Mertens, N.; Serdons, K.; Lacroix, B.; Mercier, J.; Sciberras, D.; Maguire, P.; Van Laere, K. Quantifying SV2A density and drug occupancy in the human brain using [^{11}C]UCB-J PET imaging and subcortical white matter as reference tissue. *Eur. J. Nucl. Med. Mol. Imaging* **2018**, *46*, 396–406. [CrossRef]
276. Mercier, J.; Provins, L.; Valade, A. Discovery and development of SV2A PET tracers: Potential for imaging synaptic density and clinical applications. *Drug Discov. Today Technol.* **2017**, *25*, 45–52. [CrossRef]
277. Finnema, S.J.; Nabulsi, N.B.; Eid, T.; Detyniecki, K.; Lin, S.F.; Chen, M.K.; Dhaher, R.; Matuskey, D.; Baum, E.; Holden, D.; et al. Imaging synaptic density in the living human brain. *Sci. Transl. Med.* **2016**, *8*, 348ra96. [CrossRef]
278. Finnema, S.J.; Nabulsi, N.B.; Mercier, J.; Lin, S.F.; Chen, M.K.; Matuskey, D.; Gallezot, J.D.; Henry, S.; Hannestad, J.; Huang, Y.; et al. Kinetic evaluation and test–retest reproducibility of [^{11}C]UCB-J, a novel radioligand for positron emission tomography imaging of synaptic vesicle glycoprotein 2A in humans. *J. Cereb. Blood Flow Metab.* **2017**, *38*, 2041–2052. [CrossRef]
279. Kawamura, K.; Shimoda, Y.; Yui, J.; Zhang, Y.; Yamasaki, T.; Wakizaka, H.; Hatori, A.; Xie, L.; Kumata, K.; Fujinaga, M.; et al. A useful PET probe [^{11}C]BU99008 with ultra-high specific radioactivity for small animal PET imaging of I_2-imidazoline receptors in the hypothalamus. *Nucl. Med. Biol.* **2017**, *45*, 1–7. [CrossRef] [PubMed]
280. Tyacke, R.J.; Myers, J.; Venkataraman, A.; Mick, I.; Turton, S.; Passchier, J.; Husbands, S.M.; Rabiner, E.A.; Gunn, R.N.; Murphy, P.S.; et al. Evaluation of ^{11}C-BU99008, a positron emission tomography ligand for the Imidazoline 2 binding site in human brain. *J. Nucl. Med.* **2018**, *59*, 1597–1602. [CrossRef] [PubMed]

MIM Software Inc. v. Progenics Pharmaceuticals, Inc.
IPR2025-00630
Progenics EX2017

281. Tyacke, R.J.; Fisher, A.; Robinson, E.S.; Grundt, P.; Turner, E.M.; Husbands, S.M.; Hudson, A.L.; Parker, C.A.; Nutt, D.J. Evaluation and initial in vitro and ex vivo characterization of the potential positron emission tomography ligand, BU99008 (2-(4,5-Dihydro-1H-imidazol-2-yl)-1-methyl-1H-indole), for the imidazoline2 binding site. *Synapse* **2012**, *66*, 542–551. [CrossRef] [PubMed]
282. Parker, C.A.; Nabulsi, N.; Holden, D.; Lin, S.F.; Cass, T.; Labaree, D.; Kealey, S.; Gee, A.D.; Husbands, S.M.; Quelch, D.; et al. Evaluation of 11C-BU99008, a PET ligand for the imidazoline2 binding sites in rhesus brain. *J. Nucl. Med.* **2014**, *55*, 838–844. [CrossRef]
283. Pillai, R.L.I.; Tipre, D.N. Metabotropic glutamate receptor 5—A promising target in drug development and neuroimaging. *Eur. J. Nucl. Med. Mol. Imaging* **2016**, *43*, 1151–1170. [CrossRef]
284. Yamasaki, T.; Fujinaga, M.; Yui, J.; Wakizaka, H.; Ohya, T.; Nengaki, N.; Ogawa, M.; Ikoma, Y.; Hatori, A.; Xie, L.; et al. Improved visualization and specific binding for metabotropic glutamate receptor subtype 1 (mGluR1) using [^{11}C]ITMM with ultra-high specific activity in small-animal PET. *PLoS ONE* **2015**, *10*, e0130006. [CrossRef]
285. Fujinaga, M.; Yamasaki, T.; Yui, J.; Hatori, A.; Xie, L.; Kawamura, K.; Asagawa, C.; Kumata, K.; Yoshida, Y.; Ogawa, M.; et al. Synthesis and evaluation of novel radioligands for positron emission tomography imaging of metabotropic glutamate receptor subtype 1 (mGluR1) in rodent brain. *J. Med. Chem.* **2012**, *55*, 2342–2352. [CrossRef]
286. Ishibashi, K.; Miura, Y.; Ishikawa, K.; Ishii, K.; Ishiwata, K. Decreased metabotropic glutamate receptor type 1 availability in a patient with spinocerebellar ataxia type 6: A 11C-ITMM PET study. *J. Neurol. Sci.* **2015**, *355*, 202–205. [CrossRef]
287. Sakata, M.; Toyohara, J.; Ishibashi, K.; Wagatsuma, K.; Ishii, K.; Zhang, M.R.; Ishiwata, K. Age and gender effects of ^{11}C-ITMM binding to metabotropic glutamate receptor type 1 in healthy human participants. *Neurobiol. Aging* **2017**, *55*, 72–77. [CrossRef]
288. Ishibashi, K.; Miura, Y.; Toyohara, J.; Ishii, K.; Ishiwata, K. Comparison of imaging using 11C-ITMM and 18F-FDG for the detection of cerebellar ataxia. *J. Neurol. Sci.* **2017**, *375*, 97–102. [CrossRef]
289. Toyohara, J.; Sakata, M.; Oda, K.; Ishii, K.; Ito, K.; Hiura, M.; Fujinaga, M.; Yamasaki, T.; Zhang, M.R.; Ishiwata, K. Initial human PET studies of metabotropic glutamate receptor type 1 ligand 11C-ITMM. *J. Nucl. Med.* **2013**, *54*, 1302–1307. [CrossRef] [PubMed]
290. Ghitza, U.E. Human brain imaging of opioid receptors. In *Imaging of the Human Brain Health and Disease*; Academic Press: Cambridge, MA, USA, 2014; pp. 81–98. [CrossRef]
291. Lohith, T.G.; Zoghbi, S.S.; Morse, C.L.; Araneta, M.F.; Barth, V.N.; Goebl, N.A.; Tauscher, J.T.; Pike, V.W.; Innis, R.B.; Fujita, M. Brain and whole-body imaging of nociceptin/orphanin FQ peptide receptor in humans using the PET ligand 11C-NOP-1A. *J. Nucl. Med.* **2012**, *53*, 385–392. [CrossRef] [PubMed]
292. Cai, Z.; Li, S.; Pracitto, R.; Navarro, A.; Shirali, A.; Ropchan, J.; Huang, Y. Fluorine-18-labeled antagonist for PET imaging of kappa opioid receptors. *ACS Chem. Neurosci.* **2017**, *8*, 12–16. [CrossRef] [PubMed]
293. Hazari, P.P.; Pandey, A.; Chaturvedi, S.; Mishra, A.K. New trends and current status of positron-emission tomography and single-photon-emission computerized tomography radioligands for neuronal serotonin receptors and serotonin transporter. *Bioconjug. Chem.* **2017**, *28*, 2647–2672. [CrossRef] [PubMed]
294. Yang, K.C.; Stepanov, V.; Martinsson, S.; Ettrup, A.; Takano, A.; Knudsen, G.M.; Halldin, C.; Farde, L.; Finnema, S.J. Fenfluramine reduces [^{11}C]Cimbi-36 binding to the 5-HT2A receptor in the nonhuman primate brain. *Int. J. Neuropsychopharmacol.* **2017**, *20*, 683–691. [CrossRef] [PubMed]
295. Paterson, L.M.; Kornum, B.R.; Nutt, D.J.; Pike, V.W.; Knudsen, G.M. 5-HT radioligands for human brain imaging with PET and SPECT. *Med. Res. Rev.* **2013**, *33*, 54–111. [CrossRef]
296. Finnema, S.J.; Stepanov, V.; Ettrup, A.; Nakao, R.; Amini, N.; Svedberg, M.; Lehmann, C.; Hansen, M.; Knudsen, G.M.; Halldin, C. Characterization of [(11)C]Cimbi-36 as an agonist PET radioligand for the 5-HT2A and 5-HT2C receptors in the nonhuman primate brain. *Neuroimage* **2014**, *84*, 342–353. [CrossRef]
297. Henry, K.; Kim, M.J.; Shrestha, S.; Cortes, M.; Singh, P.; Morse, C.; Liow, J.S.; Gladding, R.; Brower, C.; Gallager, E.; et al. S173. Evaluation of a potent and selective PET radioligand to image COX-1 in human and nonhuman primates. *Biol. Psychiatry* **2018**, *83*, S415. [CrossRef]
298. Singh, P.; Shrestha, S.; Cortes-Salva, M.Y.; Jenko, K.J.; Zoghbi, S.S.; Morse, C.L.; Innis, R.B.; Pike, V.W. 3-Substituted 1,5-Diaryl-1 H -1,2,4-triazoles as prospective PET radioligands for imaging brain COX-1 in monkey. Part 1: Synthesis and pharmacology. *ACS Chem. Neurosci.* **2018**, *9*, 2610–2619. [CrossRef]
299. Mansur, A.; Comley, R.; Lewis, Y.; Middleton, L.; Huiban, M.; Guo, Q.; Passchier, J.; Tsukada, H.; Gunn, R.; Rabiner, E. Imaging of mitochondrial complex 1 with 18F-BCPP-EF in the healthy human brain. *J. Nucl. Med.* **2018**, *59*, 1709.
300. Tsukada, H.; Nishiyama, S.; Fukumoto, D.; Kanazawa, M.; Harada, N. Novel PET probes 18F-BCPP-EF and 18F-BCPP-BF for mitochondrial complex I: A PET study in comparison with 18F-BMS-747158-02 in rat brain. *J. Nucl. Med.* **2014**, *55*, 473–480. [CrossRef] [PubMed]
301. Tsukada, H.; Ohba, H.; Kanazawa, M.; Kakiuchi, T.; Harada, N. Evaluation of 18F-BCPP-EF for mitochondrial complex 1 imaging in the brain of conscious monkeys using PET. *Eur. J. Nucl. Med. Mol. Imaging* **2014**, *41*, 755–763. [CrossRef] [PubMed]
302. Harada, N.; Nishiyama, S.; Kanazawa, M.; Tsukada, H. Development of novel PET probes, [^{18}F]BCPP-EF, [^{18}F]BCPP-BF, and [^{11}C]BCPP-EM for mitochondrial complex 1 imaging in the living brain. *J. Label. Compd. Radiopharm.* **2013**, *56*, 553–561. [CrossRef] [PubMed]

MIM Software Inc. v. Progenics Pharmaceuticals, Inc.
IPR2025-00630
Progenics EX2017

303. Fukuta, T.; Asai, T.; Ishii, T.; Koide, H.; Kiyokawa, C.; Hashimoto, M.; Kikuchi, T.; Shimizu, K.; Harada, N.; Tsukada, H.; et al. Non-invasive evaluation of neuroprotective drug candidates for cerebral infarction by PET imaging of mitochondrial complex-I activity. *Sci. Rep.* **2016**, *6*, 30127. [CrossRef]
304. Hideo, T.; Shingo, N.; Hiroyuki, O.; Masakatsu, K.; Takeharu, K.; Norihiro, H. Comparing amyloid-β deposition, neuroinflammation, glucose metabolism, and mitochondrial complex I activity in brain: A PET study in aged monkeys. *Eur. J. Nucl. Med. Mol. Imaging* **2014**, *41*, 2127–2136. [CrossRef]
305. Tsukada, H.; Kanazawa, M.; Ohba, H.; Nishiyama, S.; Harada, N.; Kakiuchi, T. PET imaging of mitochondrial complex I with 18F-BCPP-EF in the brains of MPTP-treated monkeys. *J. Nucl. Med.* **2016**, *57*, 950–953. [CrossRef]
306. Wey, H.Y.; Gilbert, T.M.; Zürcher, N.R.; She, A.; Bhanot, A.; Taillon, B.D.; Schroeder, F.A.; Wang, C.; Haggarty, S.J.; Hooker, J.M. Insights into neuroepigenetics through human histone deacetylase PET imaging. *Sci. Transl. Med.* **2016**, *8*, 351ra106. [CrossRef]
307. Wang, C.; Schroeder, F.A.; Wey, H.Y.; Borra, R.; Wagner, F.F.; Reis, S.; Kim, S.W.; Holson, E.B.; Haggarty, S.J.; Hooker, J.M. In vivo imaging of histone deacetylases (HDACs) in the central nervous system and major peripheral organs. *J. Med. Chem.* **2014**, *57*, 7999–8009. [CrossRef]
308. Wey, H.Y.; Wang, C.; Schroeder, F.A.; Logan, J.; Price, J.C.; Hooker, J.M. Kinetic analysis and quantification of [^{11}C]Martinostat for in vivo HDAC imaging of the brain. *ACS Chem. Neurosci.* **2015**, *6*, 708–715. [CrossRef]
309. Barret, O.; Thomae, D.; Tavares, A.; Alagille, D.; Papin, C.; Waterhouse, R.; McCarthy, T.; Jennings, D.; Marek, K.; Russell, D.; et al. In vivo assessment and dosimetry of 2 novel PDE10A PET radiotracers in humans: 18F-MNI-659 and 18F-MNI-654. *J. Nucl. Med.* **2014**, *55*, 1297–1304. [CrossRef]
310. Postnov, A.; Schmidt, M.E.; Pemberton, D.J.; de Hoon, J.; van Hecken, A.; van den Boer, M.; Zannikos, P.; van der Ark, P.; Palmer, J.A.; Rassnick, S.; et al. Fatty acid amide hydrolase inhibition by JNJ-42165279: A multiple-ascending dose and a positron emission tomography study in healthy volunteers. *Clin. Transl. Sci.* **2018**, *11*, 397–404. [CrossRef] [PubMed]
311. Liu, P.; Hamill, T.G.; Chioda, M.; Chobanian, H.; Fung, S.; Guo, Y.; Chang, L.; Bakshi, R.; Hong, Q.; Dellureficio, J.; et al. Discovery of MK-3168: A PET tracer for imaging brain fatty acid amide hydrolase. *ACS Med. Chem. Lett.* **2013**, *4*, 509–513. [CrossRef] [PubMed]
312. Joshi, A.; Li, W.; Sanabria, S.; Holahan, M.; Purcell, M.; Declercq, R.; Depre, M.; Bormans, G.; van Laere, K.; Hamill, T. Translational studies with [^{11}C]MK-3168, a PET tracer for fatty acid amide hydrolase (FAAH). *J. Nucl. Med.* **2012**, *53*, 397.
313. Lu, S.; Haskali, M.B.; Ruley, K.M.; Dreyfus, N.J.; DuBois, S.L.; Paul, S.; Liow, J.S.; Morse, C.L.; Kowalski, A.; Gladding, R.L.; et al. PET ligands [^{18}F]LSN3316612 and [^{11}C]LSN3316612 quantify O-linked-β- N-acetyl-glucosamine hydrolase in the brain. *Sci. Transl. Med.* **2020**, *12*, eaau2939. [CrossRef]
314. Lee, J.H.; Liow, J.S.; Paul, S.; Morse, C.L.; Haskali, M.B.; Manly, L.; Shcherbinin, S.; Ruble, J.C.; Kant, N.; Collins, E.C.; et al. PET quantification of brain O-GlcNAcase with [^{18}F]LSN3316612 in healthy human volunteers. *EJNMMI Res.* **2020**, *10*, 20. [CrossRef]
315. Lindberg, A.; Nag, S.; Schou, M.; Arakawa, R.; Nogami, T.; Moein, M.M.; Elmore, C.S.; Pike, V.W.; Halldin, C. Development of a ^{18}F-labeled PET radioligand for imaging 5-HT1B receptors: [^{18}F]AZ10419096. *Nucl. Med. Biol.* **2019**, *79*, 11–16. [CrossRef]
316. Koole, M.; Lohith, T.G.; Valentine, J.L.; Bennacef, I.; Declercq, R.; Reynders, T.; Riffel, K.; Celen, S.; Serdons, K.; Bormans, G.; et al. Preclinical safety evaluation and human dosimetry of [^{18}F]MK-6240, a novel pet tracer for imaging neurofibrillary tangles. *Mol. Imaging Biol.* **2020**, *22*, 173–180. [CrossRef]
317. Shrestha, S.; Kim, M.J.; Eldridge, M.; Lehmann, M.L.; Frankland, M.; Liow, J.S.; Yu, Z.X.; Cortes-Salva, M.; Telu, S.; Henter, I.D.; et al. PET measurement of cyclooxygenase-2 using a novel radioligand: Upregulation in primate neuroinflammation and first-in-human study. *J. Neuroinflamm.* **2020**, *17*, 140. [CrossRef]
318. Yan, X.; Telu, S.; Dick, R.M.; Liow, J.S.; Zanotti-Fregonara, P.; Morse, C.L.; Manly, L.S.; Gladding, R.L.; Shrestha, S.; Lerchner, W.; et al. [^{11}C]deschloroclozapine is an improved PET radioligand for quantifying a human muscarinic DREADD expressed in monkey brain. *J. Cereb. Blood. Flow. Metab.* **2021**, *41*, 2571–2582. [CrossRef]
319. Roth, B.L. DREADDs for neuroscientists. *Neuron* **2016**, *89*, 683–694. [CrossRef]
320. Kim, M.J.; Lee, J.H.; Juarez Anaya, F.; Hong, J.; Miller, W.; Telu, S.; Singh, P.; Cortes, M.Y.; Henry, K.; Tye, G.L.; et al. First-in-human evaluation of [^{11}C]PS13, a novel PET radioligand, to quantify cyclooxygenase-1 in the brain. *Eur. J. Nucl. Med. Mol. Imaging* **2020**, *47*, 3143–3151. [CrossRef] [PubMed]
321. Huang, Z.R.; Tsai, C.L.; Huang, Y.Y.; Shiue, C.Y.; Tzen, K.Y.; Yen, R.F.; Hsin, L.W. A novel potential positron emission tomography imaging agent for vesicular monoamine transporter type 2. *PLoS ONE* **2016**, *11*, e0161295. [CrossRef] [PubMed]
322. Sun, A.; Liu, S.; Tang, X.; Pan, Q.; Zhang, Z.; Ma, H.; Nie, D.; Tang, C.; Tang, G. N-(2–^{18}F-fluoropropionyl)-l-glutamate as a potential oncology tracer for PET imaging of glioma. *Appl. Radiat. Isot.* **2021**, *168*, 109530. [CrossRef] [PubMed]
323. Taillefer, R.; Harel, F. Radiopharmaceuticals for cardiac imaging: Current status and future trends. *J. Nucl. Cardiol.* **2018**, *25*, 1242–1246. [CrossRef] [PubMed]
324. Sogbein, O.O.; Pelletier-Galarneau, M.; Schindler, T.H.; Wei, L.; Wells, R.G.; Ruddy, T.D. New SPECT and PET Radiopharmaceuticals for Imaging Cardiovascular Disease. *BioMed. Res. Int.* **2014**, *2014*, 942960. [CrossRef] [PubMed]
325. Dilsizian, V.; Taillefer, R. Journey in evolution of nuclear cardiology. State-of-the-art paper: Will there be another quantum leap with the F-18-labeled myocardial perfusion radiotracers. *JACC Cardiovasc. Imaging* **2012**, *5*, 1269–1284. [CrossRef]

MIM Software Inc. v. Progenics Pharmaceuticals, Inc.
IPR2025-00630
Progenics EX2017

326. Taillefer, R.; Wackers, F.J.T. Kinetics of conventional and new cardiac radiotracers. In *Nuclear Cardiac Imaging: Principles and Applications*, 5th ed.; Iskandrian, A., Garcia, E.V., Eds.; Oxford University Press: New York, NY, USA, 2016; pp. 58–80. Available online: https://oxfordmedicine.com/view/10.1093/med/9780199392094.001.0001/med-9780199392094 (accessed on 28 March 2022).
327. Li, Y.; Zhang, W.; Wu, H.; Liu, G. Advanced Tracers in PET Imaging of Cardiovascular Disease. *BioMed. Res. Int.* **2014**, *2014*, 504532. [CrossRef]
328. Nesterov, S.V.; Deshayes, E.; Sciagrà, R.; Settimo, L.; Declerck, J.M.; Pan, X.B.; Yoshinaga, K.; Katoh, C.; Slomka, P.J.; Germano, G.; et al. Quantification of myocardial blood flow in absolute terms using 82Rb PET imaging: The RUBY-10 Study. *JACC Cardiovasc. Imaging* **2014**, *7*, 1119–1127. [CrossRef]
329. Renaud, J.M.; Yip, K.; Guimond, J.; Trottier, M.; Pibarot, P.; Turcotte, E.; Maguire, C.; Lalonde, L.; Gulenchyn, K.; Farncombe, T.; et al. Characterization of 3-dimensional PET systems for accurate quantification of myocardial blood flow. *J. Nucl. Med.* **2017**, *58*, 103–109. [CrossRef]
330. Guehl, N.J.; Pelletier-Galarneau, M.; Wooten, D.W.; Guerrero, J.L.; Kas, A.; Normandin, M.D.; Fakhri, G.E.; Alpert, N.M. Preclinical validation of a single-scan rest/stress imaging technique for ^{13}N-ammonia positron emission tomography cardiac perfusion studies. *Circ. Cardiovasc. Imaging* **2020**, *13*, e009407. [CrossRef]
331. Juneau, D.; Ruddy, T.D.; Beanlands, R.; deKemp, R.A. False-positive 13N-ammonia positron emission tomography perfusion scan caused by misalignment of adjacent lung activity during attenuation correction. *J. Nucl. Cardiol.* **2018**, *25*, 1056–1058. [CrossRef] [PubMed]
332. Fathala, A.; Aboulkheir, M.; Shoukri, M.M.; Alsergani, H. Diagnostic accuracy of ^{13}N-ammonia myocardial perfusion imaging with PET-CT in the detection of coronary artery disease. *Cardiovasc. Diagn. Ther.* **2019**, *9*, 35–42. [CrossRef] [PubMed]
333. Klein, R.; deKemp, R.A. 82Rb is the best flow tracer for high-volume sites. *Ann. Nucl. Cardiol.* **2019**, *5*, 53–62. [CrossRef]
334. Kaster, T.S.; Dwivedi, G.; Susser, L.; Renaud, J.M.; Beanlands, R.S.; Chow, B.J.; deKemp, R.A. Single low-dose CT scan optimized for rest-stress PET attenuation correction and quantification of coronary artery calcium. *J. Nucl. Cardiol.* **2015**, *22*, 419–428. [CrossRef]
335. Mc Ardle, B.A.; Dowsley, T.F.; deKemp, R.A.; Wells, G.A.; Beanlands, R.S. Does rubidium-82 PET have superior accuracy to SPECT perfusion imaging for the diagnosis of obstructive coronary disease? A systematic review and meta-analysis. *J. Am. Coll. Cardiol.* **2012**, *60*, 1828–1837. [CrossRef]
336. Dorbala, S.; Di Carli, M.F.; Beanlands, R.S.; Merhige, M.E.; Williams, B.A.; Veledar, E.; Chow, B.J.; Min, J.K.; Pencina, M.J.; Berman, D.S.; et al. Prognostic value of stress myocardial perfusion positron emission tomography: Results from a multicenter observational registry. *J. Am. Coll. Cardiol.* **2013**, *61*, 176–184. [CrossRef]
337. Dekemp, R.A.; Declerck, J.; Klein, R.; Pan, X.B.; Nakazato, R.; Tonge, C.; Arumugam, P.; Berman, D.S.; Germano, G.; Beanlands, R.S.; et al. Multisoftware reproducibility study of stress and rest myocardial blood flow assessed with 3D dynamic PET/CT and a 1-tissue-compartment model of 82Rb kinetics. *J. Nucl. Med.* **2013**, *54*, 571–577. [CrossRef]
338. Ziadi, M.C.; Dekemp, R.A.; Williams, K.; Guo, A.; Renaud, J.M.; Chow, B.J.; Klein, R.; Ruddy, T.D.; Aung, M.; Garrard, L.; et al. Does quantification of myocardial flow reserve using rubidium-82 positron emission tomography facilitate detection of multivessel coronary artery disease? *J. Nucl. Cardiol.* **2012**, *19*, 670–680. [CrossRef]
339. Prior, J.O.; Allenbach, G.; Valenta, I.; Kosinski, M.; Burger, C.; Verdun, F.R.; Bischof Delaloye, A.; Kaufmann, P.A. Quantification of myocardial blood flow with Rb-82 positron emission tomography: Clinical validation with O-15 water. *Eur. J. Nucl. Mol. Imaging* **2012**, *39*, 1037–1047. [CrossRef]
340. Maddahi, J.; Czernin, J.; Lazewatsky, J.; Huang, S.C.; Dahlbom, M.; Schelbert, H.; Sparks, R.; Ehlgen, A.; Crane, P.; Zhu, Q.; et al. Phase I, first-human study of BMS747158, a novel 18F-labeled tracer for myocardial perfusion PET: Dosimetry, biodistribution, safety and imaging characteristics after a single injection at rest. *J. Nucl. Med.* **2011**, *52*, 1490–1498. [CrossRef]
341. Berman, D.S.; Maddahi, J.; Tamarappoo, B.K.; Czernin, J.; Taillefer, R.; Udelson, J.E.; Gibson, C.M.; Devine, M.; Lazewatsky, J.; Bhat, G.; et al. Phase II safety and clinical comparison with single-photon emission computed tomography myocardial perfusion imaging for detection of coronary artery disease. *J. Am. Coll. Cardiol.* **2013**, *61*, 469–477. [CrossRef] [PubMed]
342. Manabe, O.; Kikuchi, T.; Scholte, A.; El Mahdiui, M.; Nishii, R.; Zhang, M.R.; Suzuki, E.; Yoshinaga, K. Radiopharmaceutical tracers for cardiac imaging. *J. Nucl. Cardiol.* **2018**, *25*, 1204–1236. [CrossRef] [PubMed]
343. Danad, I.; Uusitalo, V.; Kero, T.; Saraste, A.; Raijmakers, P.G.; Lammertsma, A.A.; Heymans, M.W.; Kajander, S.A.; Pietilä, M.; James, S.; et al. Quantitative assessment of myocardial perfusion in the detection of significant coronary artery disease: Cut-off values and diagnostic accuracy of quantitative [(15)O]H2O PET imaging. *J. Am. Coll. Cardiol.* **2014**, *64*, 1464–1475. [CrossRef] [PubMed]
344. Bateman, T. Current Status of myocardial perfusion PET in the United States. *Ann. Nucl. Cardiol.* **2017**, *3*, 157–162. [CrossRef]
345. Dweck, M.R.; Jones, C.; Joshi, N.V.; Fletcher, A.M.; Richardson, H.; White, A.; Marsden, M.; Pessotto, R.; Clark, J.C.; Wallace, W.A.; et al. Assessment of valvular calcification and inflammation by positron emission tomography in patients with aortic stenosis. *Circulation* **2012**, *125*, 76–86. [CrossRef]
346. Thackeray, J.T.; Bengel, F.M. PET imaging of the autonomic nervous system. *Q. J. Nucl. Med. Mol. Imaging* **2016**, *60*, 362–382.
347. Cuhlmann, S.; Gsell, W.; Van der Heiden, K.; Habib, J.; Tremoleda, J.L.; Khalil, M.; Turkheimer, F.; Meens, M.J.; Kwak, B.R.; Bird, J.; et al. In Vivo Mapping of Vascular Inflammation Using the Translocator Protein Tracer 18F-FEDAA1106. *Mol. Imaging* **2014**, *13*, 1–11. [CrossRef]

MIM Software Inc. v. Progenics Pharmaceuticals, Inc.
IPR2025-00630
Progenics EX2017

348. Guilarte, T.R. TSPO in diverse CNS pathologies and psychiatric disease: A critical review and a way forward. *Pharmacol. Ther.* **2019**, *194*, 44–58. [CrossRef]
349. Vivash, L.; O'Brien, T.J. Imaging Microglial Activation with TSPO PET: Lighting Up Neurologic Diseases? *J. Nucl. Med.* **2016**, *57*, 165–168. [CrossRef]
350. Largeau, B.; Dupont, A.C.; Guilloteau, D.; Santiago-Ribeiro, M.J.; Arlicot, N. TSPO PET Imaging: From Microglial Activation to Peripheral Sterile Inflammatory Diseases? *Contrast Media Mol. Imaging* **2017**, *2017*, 6592139. [CrossRef]
351. Hatori, A.; Yui, J.; Xie, L.; Yamasaki, T.; Kumata, K.; Fujinaga, M.; Wakizaka, H.; Ogawa, M.; Nengaki, N.; Kawamura, K.; et al. Visualization of acute liver damage induced by cycloheximide in rats using PET with [^{18}F]FEDAC, a radiotracer for translocator protein (18 kDa). *PLoS ONE* **2014**, *9*, e86625. [CrossRef]
352. Gaemperli, O.; Shalhoub, J.; Owen, D.R.; Lamare, F.; Johansson, S.; Fouladi, N.; Davies, A.H.; Rimoldi, O.E.; Camici, P.G. Imaging intraplaque inflammation in carotid atherosclerosis with ^{11}C-PK11195 positron emission tomography/computed tomography. *Eur. Heart J.* **2012**, *33*, 1902–1910. [CrossRef] [PubMed]
353. Hellberg, S.; Silvola, J.; Kiugel, M.; Liljenbäck, H.; Savisto, N.; Li, X.G.; Thiele, A.; Lehmann, L.; Heinrich, T.; Vollmer, S.; et al. 18-kDa translocator protein ligand ^{18}F-FEMPA: Biodistribution and uptake into atherosclerotic plaques in mice. *J. Nucl. Cardiol.* **2017**, *24*, 862–871. [CrossRef] [PubMed]
354. Thackeray, J.T.; Hupe, H.C.; Wang, Y.; Bankstahl, J.P.; Berding, G.; Ross, T.L.; Bauersachs, J.; Wollert, K.C.; Bengel, F.M. Myocardial Inflammation Predicts Remodeling and Neuroinflammation After Myocardial Infarction. *J. Am. Coll. Cardiol.* **2018**, *71*, 263–275. [CrossRef] [PubMed]
355. Pieper, J.; Patel, V.N.; Escolero, S.; Nelson, J.R.; Poitrasson-Rivière, A.; Shreves, C.K.; Freiburger, N.; Hubers, D.; Rothley, J.; Corbett, J.R.; et al. Initial clinical experience of N13-ammonia myocardial perfusion PET/CT using a compact superconducting production system. *J. Nucl. Cardiol.* **2019**, *28*, 295–299. [CrossRef] [PubMed]
356. Leipsic, J.; Raju, R.; Naoum, C.; Knuuti, J.; Mäki, M.; Underwood, R.S.; Min, J.K.; Elmore, K.; Stuijfzand, W.J.; van Royen, N.; et al. Comparison of coronary CT angiography, SPECT, PET, and hybrid imaging for diagnosis of ischemic heart disease determined by fractional flow reserve. *JAMA Cardiol.* **2017**, *2*, 1100–1107. [CrossRef]
357. Driessen, R.S.; Danad, I.; Stuijfzand, W.J.; Schumacher, S.P.; Knuuti, J.; Mäki, M.; Lammertsma, A.A.; van Rossum, A.C.; van Royen, N.; Raijmakers, P.G.; et al. Impact of revascularization on absolute myocardial blood flow as assessed by serial [^{15}O]H_2O positron emission tomography imaging. *Circ. Cardiovasc. Imaging* **2018**, *11*, e007417. [CrossRef]
358. Klein, R.; Celiker-Guler, E.; Rotstein, B.H.; deKemp, R.A. PET and SPECT Tracers for Myocardial Perfusion Imaging. *Semin. Nucl. Med.* **2020**, *50*, 208–218. [CrossRef]
359. Li, J.; Lu, J.; Zhou, Y. Mitochondrial-targeted molecular imaging in cardiac disease. *BioMed. Res. Int.* **2017**, *2017*, 5246853. [CrossRef]
360. Mou, T.; Zhang, X. Research progress on ^{18}F-labeled agents for imaging of myocardial perfusion with positron emission tomography. *Molecules* **2017**, *22*, 562. [CrossRef]
361. Maddahi, J.; Lazewatsky, J.; Udelson, J.E.; Berman, D.S.; Beanlands, R.; Heller, G.V.; Bateman, T.M.; Knuuti, J.; Orlandi, C. Phase-III Clinical Trial of Fluorine-18 Flurpiridaz Positron Emission Tomography for Evaluation of Coronary Artery Disease. *J. Am. Coll Cardiol.* **2020**, *76*, 391–401. [CrossRef] [PubMed]
362. Sherif, H.M.; Nekolla, S.G.; Saraste, A.; Reder, S.; Yu, M.; Robinson, S.; Schwaiger, M. Simplified quantification of myocardial flow reserve with flurpiridaz F 18: Validation with micro-spheres in a pig model. *J. Nucl. Med.* **2011**, *52*, 617–624. [CrossRef] [PubMed]
363. Mou, T.; Zhao, Z.; You, L.; Li, Y.; Wang, Q.; Fang, W.; Lu, J.; Peng, C.; Zhang, X. Synthesis and evaluation of ^{18}F-labeled pyridaben analogues for myocardial perfusion imaging in mice, rats and Chinese mini-swine. *Sci. Rep.* **2016**, *6*, 33450. [CrossRef] [PubMed]
364. Mou, T.; Zhao, Z.; Fang, W.; Peng, C.; Guo, F.; Liu, B.; Ma, Y.; Zhang, X. Synthesis and preliminary evaluation of ^{18}F-labeled pyridaben analogues for myocardial perfusion imaging with PET. *J. Nucl. Med.* **2012**, *53*, 472–479. [CrossRef]
365. Kim, D.Y.; Kim, H.S.; Le, U.N.; Jiang, S.N.; Kim, H.J.; Lee, K.C.; Woo, S.K.; Chung, J.; Kim, H.S.; Bom, H.S.; et al. Evaluation of a mitochondrial voltage sensor, (^{18}F-fluoropentyl)triphenylphosphonium cation, in a rat myocardial infarction model. *J. Nucl. Med.* **2012**, *53*, 1779–1785. [CrossRef]
366. Heo, G.S.; Sultan, D.; Liu, Y. Current and Novel Radiopharmaceuticals for Imaging Cardiovascular Inflammation. *Q. J. Nucl. Med. Mol. Imaging* **2020**, *64*, 4–20. [CrossRef]
367. LaForest, R.; Woodard, P.K.; Gropler, R.J. Cardiovascular PET/MRI: Challenges and Opportunities. *Cardiol. Clin.* **2016**, *34*, 25–35. [CrossRef]
368. Amsallem, M.; Saito, T.; Tada, Y.; Dash, R.; McConnell, M.V. Magnetic Resonance Imaging and Positron Emission Tomography Approaches to Imaging Vascular and Cardiac Inflammation. *Circ. J.* **2016**, *80*, 1269–1277. [CrossRef]
369. Tarkin, J.M.; Joshi, F.R.; Evans, N.R.; Chowdhury, M.M.; Figg, N.L.; Shah, A.V.; Starks, L.T.; Martin-Garrido, A.; Manavaki, R.; Yu, E.; et al. Detection of Atherosclerotic Inflammation by ^{68}Ga-DOTATATE PET Compared to [^{18}F]FDG PET Imaging. *J. Am. Coll. Cardiol.* **2017**, *69*, 1774–1791. [CrossRef]
370. Joseph, P.; Tawakol, A. Imaging atherosclerosis with positron emission tomography. *Eur. Heart J.* **2016**, *37*, 2974–2980. [CrossRef]
371. Van der Vorst, E.P.C.; Peters, L.J.F.; Müller, M.; Gencer, S.; Yan, Y.; Weber, C.; Döring, Y. G-Protein Coupled Receptor Targeting on Myeloid Cells in Atherosclerosis. *Front. Pharmacol.* **2019**, *10*, 531. [CrossRef] [PubMed]

MIM Software Inc. v. Progenics Pharmaceuticals, Inc.
IPR2025-00630
Progenics EX2017

372. Hyafil, F.; Pelisek, J.; Laitinen, I.; Schottelius, M.; Mohring, M.; Döring, Y.; van der Vorst, E.P.; Kallmayer, M.; Steiger, K.; Poschenrieder, A.; et al. Imaging the Cytokine Receptor CXCR4 in Atherosclerotic Plaques with the Radiotracer ^{68}Ga-Pentixafor for PET. *J. Nucl. Med.* **2017**, *58*, 499–506. [CrossRef] [PubMed]
373. Weiberg, D.; Thackeray, J.T.; Daum, G.; Sohns, J.M.; Kropf, S.; Wester, H.J.; Ross, T.L.; Bengel, F.M.; Derlin, T. Clinical Molecular Imaging of Chemokine Receptor CXCR4 Expression in Atherosclerotic Plaque Using ^{68}Ga-Pentixafor PET: Correlation with Cardiovascular Risk Factors and Calcified Plaque Burden. *J. Nucl. Med.* **2018**, *59*, 266–272. [CrossRef] [PubMed]
374. Derlin, T.; Sedding, D.G.; Dutzmann, J.; Haghikia, A.; König, T.; Napp, L.C.; Schütze, C.; Owsianski-Hille, N.; Wester, H.J.; Kropf, S.; et al. Imaging of chemokine receptor CXCR4 expression in culprit and nonculprit coronary atherosclerotic plaque using motion-corrected [^{68}Ga]pentixafor PET/CT. *Eur. J. Nucl. Med. Mol. Imaging* **2018**, *45*, 1934–1944. [CrossRef] [PubMed]
375. Li, X.; Yu, W.; Wollenweber, T.; Lu, X.; Wei, Y.; Beitzke, D.; Wadsak, W.; Kropf, S.; Wester, H.J.; Haug, A.R.; et al. [^{68}Ga]Pentixafor PET/MR imaging of chemokine receptor 4 expression in the human carotid artery. *Eur. J. Nucl. Med. Mol. Imaging* **2019**, *46*, 1616–1625. [CrossRef] [PubMed]
376. Thackeray, J.T.; Derlin, T.; Haghikia, A.; Napp, L.C.; Wang, Y.; Ross, T.L.; Schäfer, A.; Tillmanns, J.; Wester, H.J.; Wollert, K.C.; et al. Molecular Imaging of the Chemokine Receptor CXCR4 After Acute Myocardial Infarction. *JACC Cardiovasc. Imaging* **2015**, *8*, 1417–1426. [CrossRef] [PubMed]
377. Liu, Y.; Li, W.; Luehmann, H.P.; Zhao, Y.; Detering, L.; Sultan, D.H.; Hsiao, H.M.; Krupnick, A.S.; Gelman, A.E.; Combadiere, C.; et al. Noninvasive Imaging of CCR2+ Cells in Ischemia-Reperfusion Injury After Lung Transplantation. *Am. J. Transpl.* **2016**, *16*, 3016–3023. [CrossRef] [PubMed]
378. Liu, Y.; Gunsten, S.P.; Sultan, D.H.; Luehmann, H.P.; Zhao, Y.; Blackwell, T.S.; Bollermann-Nowlis, Z.; Pan, J.H.; Byers, D.E.; Atkinson, J.J.; et al. PET-based Imaging of Chemokine Receptor 2 in Experimental and Disease-related Lung Inflammation. *Radiology* **2017**, *283*, 758–768. [CrossRef]
379. Li, W.; Luehmann, H.P.; Hsiao, H.M.; Tanaka, S.; Higashikubo, R.; Gauthier, J.M.; Sultan, D.; Lavine, K.J.; Brody, S.L.; Gelman, A.E.; et al. Visualization of Monocytic Cells in Regressing Atherosclerotic Plaques by Intravital 2-Photon and Positron Emission Tomography-Based Imaging-Brief Report. *Arter. Thromb. Vasc Biol.* **2018**, *38*, 1030–1036. [CrossRef]
380. Heo, G.S.; Kopecky, B.; Sultan, D.; Ou, M.; Feng, G.; Bajpai, G.; Zhang, X.; Luehmann, H.; Detering, L.; Su, Y.; et al. Molecular Imaging Visualizes Recruitment of Inflammatory Monocytes and Macrophages to the Injured Heart. *Circ. Res.* **2019**, *124*, 881–890. [CrossRef]
381. Luehmann, H.P.; Pressly, E.D.; Detering, L.; Wang, C.; Pierce, R.; Woodard, P.K.; Gropler, R.J.; Hawker, C.J.; Liu, Y. PET/CT Imaging of Chemokine Receptor CCR5 in Vascular Injury Model Using Targeted Nanoparticle. *J. Nucl. Med.* **2014**, *55*, 629–634. [CrossRef] [PubMed]
382. Liu, Y.; Pierce, R.; Luehmann, H.P.; Sharp, T.L.; Welch, M.J. PET Imaging of Chemokine Receptors in Vascular Injury–Accelerated Atherosclerosis. *J. Nucl. Med.* **2013**, *54*, 1135–1341. [CrossRef] [PubMed]
383. Li, X.; Bauer, W.; Kreissl, M.C.; Weirather, J.; Bauer, E.; Israel, I.; Richter, D.; Riehl, G.; Buck, A.; Samnick, S. Specific somatostatin receptor II expression in arterial plaque: ^{68}Ga-DOTATATE autoradiographic, immunohistochemical and flow cytometric studies in apoE-deficient mice. *Atherosclerosis* **2013**, *230*, 33–39. [CrossRef] [PubMed]
384. Rinne, P.; Hellberg, S.; Kiugel, M.; Virta, J.; Li, X.G.; Käkelä, M.; Helariutta, K.; Luoto, P.; Liljenbäck, H.; Hakovirta, H.; et al. Comparison of Somatostatin Receptor 2-Targeting PET Tracers in the Detection of Mouse Atherosclerotic Plaques. *Mol. Imaging Biol.* **2016**, *18*, 99–108. [CrossRef] [PubMed]
385. Mojtahedi, A.; Alavi, A.; Thamake, S.; Amerinia, R.; Ranganathan, D.; Tworowska, I.; Delpassand, E.S. Assessment of vulnerable atherosclerotic and fibrotic plaques in coronary arteries using ^{68}Ga-DOTATATE PET/CT. *Am. J. Nucl. Med. Mol. Imaging* **2014**, *5*, 65–71. [PubMed]
386. Li, X.; Samnick, S.; Lapa, C.; Israel, I.; Buck, A.K.; Kreissl, M.C.; Bauer, W. ^{68}Ga-DOTATATE PET/CT for the detection of inflammation of large arteries: Correlation with ^{18}F-FDG, calcium burden and risk factors. *EJNMMI Res.* **2012**, *2*, 52. [CrossRef]
387. Malmberg, C.; Ripa, R.S.; Johnbeck, C.B.; Knigge, U.; Langer, S.W.; Mortensen, J.; Oturai, P.S.; Loft, A.; Hag, A.M.; Kjær, A. ^{64}Cu-DOTATATE for Noninvasive Assessment of Atherosclerosis in Large Arteries and Its Correlation with Risk Factors: Head-to-Head Comparison with ^{68}Ga-DOTATOC in 60 Patients. *J. Nucl. Med.* **2015**, *56*, 1895–1900. [CrossRef]
388. Pedersen, S.F.; Sandholt, B.V.; Keller, S.H.; Hansen, A.E.; Clemmensen, A.E.; Sillesen, H.; Højgaard, L.; Ripa, R.S.; Kjær, A. ^{64}Cu-DOTATATE PET/MRI for Detection of Activated Macrophages in Carotid Atherosclerotic Plaques. *Arter. Thromb. Vasc. Biol.* **2015**, *35*, 1696–1703. [CrossRef] [PubMed]
389. Schatka, I.; Wollenweber, T.; Haense, C.; Brunz, F.; Gratz, K.F.; Bengel, F.M. Peptide Receptor–Targeted Radionuclide Therapy Alters Inflammation in Atherosclerotic Plaques. *J. Am. Coll. Cardiol.* **2013**, *62*, 2344–2345. [CrossRef]
390. Tahara, N.; Mukherjee, J.; de Haas, H.J.; Petrov, A.D.; Tawakol, A.; Haider, N.; Tahara, A.; Constantinescu, C.C.; Zhou, J.; Boersma, H.H.; et al. 2- deoxy-2-[^{18}F]fluoro-d-mannose positron emission tomography imaging in atherosclerosis. *Nat. Med.* **2014**, *20*, 215–219. [CrossRef]
391. Kim, E.J.; Kim, S.; Seo, H.S.; Lee, Y.J.; Eo, J.S.; Jeong, J.M.; Lee, B.; Kim, J.Y.; Park, Y.M.; Jeong, M. Novel PET Imaging of Atherosclerosis with ^{68}Ga-Labeled NOTA-Neomannosylated Human Serum Albumin. *J. Nucl. Med.* **2016**, *57*, 1792–1797. [CrossRef] [PubMed]

MIM Software Inc. v. Progenics Pharmaceuticals, Inc.
IPR2025-00630
Progenics EX2017

392. Senders, M.L.; Hernot, S.; Carlucci, G.; van de Voort, J.C.; Fay, F.; Calcagno, C.; Tang, J.; Alaarg, A.; Zhao, Y.; Ishino, S.; et al. Nanobody- Facilitated Multiparametric PET/MRI Phenotyping of Atherosclerosis. *JACC Cardiovasc. Imaging* **2018**, *12*, 2015–2026. [CrossRef] [PubMed]
393. Varasteh, Z.; Hyafil, F.; Anizan, N.; Diallo, D.; Aid-Launais, R.; Mohanta, S.; Li, Y.; Braeuer, M.; Steiger, K.; Vigne, J.; et al. Targeting mannose receptor expression on macrophages in atherosclerotic plaques of apolipoprotein E-knockout mice using ^{111}In-tilmanocept. *EJNMMI Res.* **2017**, *7*, 40. [CrossRef] [PubMed]
394. Hellberg, S.; Silvola, J.M.U.; Kiugel, M.; Liljenbäck, H.; Metsälä, O.; Viljanen, T.; Metso, J.; Jautihiainen, M.; Saukko, P.; Nuutila, P.; et al. Type 2 diabetes enhances arterial uptake of choline in atherosclerotic mice: An imaging study with positron emission tomography tracer ^{18}F-fluoromethylcholine. *Cardiovasc. Diabetol.* **2016**, *15*, 26. [CrossRef]
395. Vöö, S.; Kwee, R.M.; Sluimer, J.C.; Schreuder, F.H.; Wierts, R.; Bauwens, M.; Heeneman, S.; Cleutjens, J.P.; van Oostenbrugge, R.J.; Daemen, J.W.; et al. Imaging Intraplaque Inflammation in Carotid Atherosclerosis With ^{18}F-Fluorocholine Positron Emission Tomography-Computed Tomography. *Circ. Cardiovasc. Imaging* **2016**, *9*, e004467. [CrossRef]
396. Ye, Y.X.; Calcagno, C.; Binderup, T.; Courties, G.; Keliher, E.J.; Wojtkiewicz, G.R.; Iwamoto, Y.; Tang, J.; Pérez-Medina, C.; Mani, V.; et al. Imaging Macrophage and Hematopoietic Progenitor Proliferation in Atherosclerosis. *Circ. Res.* **2015**, *117*, 835–845. [CrossRef]
397. Majmudar, M.D.; Yoo, J.; Keliher, E.J.; Truelove, J.J.; Iwamoto, Y.; Sena, B.; Dutta, P.; Borodovsky, A.; Fitzgerald, K.; Di Carli, M.F.; et al. Polymeric Nanoparticle PET/MR Imaging Allows Macrophage Detection in Atherosclerotic Plaques. *Circ. Res.* **2013**, *112*, 755–761. [CrossRef]
398. Keliher, E.J.; Ye, Y.X.; Wojtkiewicz, G.R.; Aguirre, A.D.; Tricot, B.; Senders, M.L.; Groenen, H.; Fay, F.; Perez-Medina, C.; Calcagno, C.; et al. Polyglucose nanoparticles with renal elimination and macrophage avidity facilitate PET imaging in ischemic heart disease. *Nat. Commun.* **2017**, *8*, 14064. [CrossRef]
399. Meester, E.J.; Krenning, B.J.; de Blois, R.H.; Norenberg, J.P.; de Jong, M.; Bernsen, M.R.; Van der Heiden, K. Imaging of atherosclerosis, targeting LFA-1 on inflammatory cells with ^{111}In-DANBIRT. *J. Nucl. Cardiol.* **2018**, *26*, 1697–1704. [CrossRef]
400. Mota, R.; Campen, M.J.; Cuellar, M.E.; Garver, W.S.; Hesterman, J.; Qutaish, M.; Daniels, T.; Nysus, M.; Wagner, C.R.; Norenberg, J.P. ^{111}In-DANBIRT In Vivo Molecular Imaging of Inflammatory Cells in Atherosclerosis. *Contrast Media Mol. Imaging* **2018**, 6508724. [CrossRef]
401. Di Gialleonardo, V.; Signore, A.; Glaudemans, A.W.J.M.; Dierckx, R.A.J.O.; De Vries, E.F.J. N-(4–^{18}F- Fluorobenzoyl)Interleukin-2 for PET of Human-Activated T Lymphocytes. *J. Nucl. Med.* **2012**, *53*, 679–686. [CrossRef]
402. Hermann, S.; Starsichova, A.; Waschkau, B.; Kuhlmann, M.; Wenning, C.; Schober, O.; Schäfers, M. Non-FDG imaging of atherosclerosis: Will imaging of MMPs assess plaque vulnerability? *J. Nucl. Cardiol.* **2012**, *19*, 609–617. [CrossRef] [PubMed]
403. Matusiak, N.; van Waarde, A.; Bischoff, R.; Oltenfreiter, R.; van de Wiele, C.; Dierckx, R.A.; Elsinga, P.H. Probes for Non-invasive Matrix Metalloproteinase-targeted Imaging with PET and SPECT. *Curr. Pharm. Des.* **2013**, *19*, 4647–4672. [CrossRef] [PubMed]
404. Malm, B.J.; Sadeghi, M.M. Multi-modality molecular imaging of aortic aneurysms. *J. Nucl. Cardiol.* **2017**, *24*, 1239–1245. [CrossRef] [PubMed]
405. Toczek, J.; Ye, Y.; Gona, K.; Kim, H.Y.; Han, J.; Razavian, M.; Golestani, R.; Zhang, J.; Wu, T.L.; Jung, J.J.; et al. Preclinical Evaluation of RYM1, a Matrix Metalloproteinase-Targeted Tracer for Imaging Aneurysm. *J. Nucl. Med.* **2017**, *58*, 1318–1323. [CrossRef]
406. Toczek, J.; Bordenave, T.; Gona, K.; Kim, H.Y.; Beau, F.; Georgiadis, D.; Correia, I.; Ye, Y.; Razavian, M.; Jung, J.J.; et al. Novel Matrix Metalloproteinase 12 selective radiotracers for vascular molecular imaging. *J. Med. Chem.* **2019**, *62*, 9743–9752. [CrossRef]
407. Butsch, V.; Börgel, F.; Galla, F.; Schwegmann, K.; Hermann, S.; Schäfers, M.; Riemann, B.; Wünsch, B.; Wagner, S. Design, (Radio)Synthesis, and in Vitro and in Vivo Evaluation of Highly Selective and Potent Matrix Metalloproteinase 12 (MMP-12) Inhibitors as Radiotracers for Positron Emission Tomography. *J. Med. Chem.* **2018**, *61*, 4115–4134. [CrossRef]
408. Hugenberg, V.; Wagner, S.; Kopka, K.; Schäfers, M.; Schuit, R.C.; Windhorst, A.D.; Hermann, S. Radiolabeled Selective Matrix Metalloproteinase 13 (MMP-13) Inhibitors: (Radio)Syntheses and in Vitro and First in Vivo Evaluation. *J. Med. Chem.* **2017**, *60*, 307–321. [CrossRef]
409. Auletta, S.; Varani, M.; Horvat, R.; Galli, F.; Signore, A.; Hess, S. PET Radiopharmaceuticals for Specific Bacteria Imaging: A Systematic Review. *J. Clin. Med.* **2019**, *8*, 197. [CrossRef]
410. Bhatt, J.; Mukherjee, A.; Shinto, A.; Koramadai Karuppusamy, K.; Korde, A.; Kumar, M.; Sarma, H.D.; Repaka, K.; Dash, A. Gallium-68 labeled Ubiquicidin derived octapeptide as a potential infection imaging agent. *Nucl. Med. Biol.* **2018**, *62–63*, 47–53. [CrossRef]
411. Ebenhan, T.; Sathekge, M.M.; Lengana, T.; Koole, M.; Gheysens, O.; Govender, T.; Zeevaart, J.R. ^{68}Ga-NOTA-Functionalized Ubiquicidin: Cytotoxicity, Biodistribution, Radiation Dosimetry, and First-in-Human PET/CT Imaging of Infections. *J. Nucl. Med.* **2018**, *59*, 334–339. [CrossRef] [PubMed]
412. Vilche, M.; Reyes, A.L.; Vasilskis, E.; Oliver, P.; Balter, H.; Engler, H. ^{68}Ga-NOTA-UBI-29-41 as a PET tracer for detection of bacterial infection. *J. Nucl. Med.* **2016**, *57*, 622–627. [CrossRef] [PubMed]
413. Ebenhan, T.; Zeevaart, J.R.; Venter, J.D.; Govender, T.; Kruger, G.H.; Jarvis, N.V.; Sathekge, M.M. Preclinical Evaluation of ^{68}Ga-Labeled 1,4,7-triazacyclononane-1,4,7-triacetic acid-ubiquicidin as a radioligand for PET infection imaging. *J. Nucl. Med.* **2014**, *55*, 308–314. [CrossRef]

MIM Software Inc. v. Progenics Pharmaceuticals, Inc.
IPR2025-00630
Progenics EX2017

414. Zhang, X.M.; Zhang, H.H.; McLeroth, P.; Berkowitz, R.D.; Mont, M.A.; Stabin, M.G.; Siegel, B.A.; Alavi, A.; Barnett, T.M.; Gelb, J.; et al. [^{124}I]FIAU: Human dosimetry and infection imaging in patients with suspected prosthetic joint infection. *Nucl. Med. Biol.* **2016**, *43*, 273–279. [CrossRef] [PubMed]
415. Mills, B.; Awais, R.O.; Luckett, J.; Turton, D.; Williams, P.; Perkins, A.C.; Hill, P.J. [^{18}F]FDG-6-P as a novel in vivo tool for imaging staphylococcal infections. *EJNMMI Res.* **2015**, *5*, 13. [CrossRef] [PubMed]
416. Satpati, D.; Arjun, C.; Krishnamohan, R.; Samuel, G.; Banerjee, S. ^{68}Ga-labeled ciprofloxacin conjugates as radiotracers for targeting bacterial infection. *Chem. Biol. Drug. Des.* **2016**, *87*, 680–686. [CrossRef] [PubMed]
417. Nielsen, K.M.; Jørgensen, N.P.; Kyneb, M.H.; Borghammer, P.; Meyer, R.L.; Thomsen, T.R.; Bender, D.; Jensen, S.B.; Nielsen, O.L.; Alstrup, A. Preclinical evaluation of potential infection-imaging probe [^{68}Ga]Ga-DOTA-K-A9 in sterile and infectious inflammation. *J. Label. Compd. Radiopharm.* **2018**, *61*, 780–795. [CrossRef] [PubMed]
418. Li, J.; Zheng, H.; Fodah, R.; Warawa, J.M.; Ng, C.K. Validation of 2- ^{18}F-Fluorodeoxysorbitol as a potential radiopharmaceutical for imaging bacterial infection in the lung. *J. Nucl. Med.* **2018**, *59*, 134–139. [CrossRef]
419. Yao, S.; Xing, H.; Zhu, W.; Wu, Z.; Zhang, Y.; Ma, Y.; Liu, Y.; Zhu, Z.; Li, Z.; Fang, L. Infection imaging with ^{18}F-FDS and first-in-human evaluation. *Nucl. Med. Biol.* **2016**, *43*, 206–214. [CrossRef]
420. Weinstein, E.A.; Ordonez, A.A.; DeMarco, V.P.; Murawski, A.M.; Pokkali, S.; MacDonald, E.M.; Klunk, M.; Mease, R.C.; Pomper, M.G.; Jain, S.K. Imaging Enterobacteriaceae infection in vivo with ^{18}F-fluorodeoxysorbitol positron emission tomography. *Sci. Transl. Med.* **2014**, *6*, 259ra146. [CrossRef]
421. Ning, X.; Seo, W.; Lee, S.; Takemiya, K.; Rafi, M.; Feng, X.; Weiss, D.; Wang, X.; Williams, L.; Camp, V.M.; et al. Fluorine-18 labeled maltohexaose images bacterial infections by PET. *Angew. Chem. Int. Ed. Engl.* **2014**, *53*, 14096–14101. [CrossRef] [PubMed]
422. Gowrishankar, G.; Namavari, M.; Jouannot, E.B.; Hoehne, A.; Reeves, R.; Hardy, J.; Gambhir, S.S. Investigation of 6-[^{18}F]-fluoromaltose as a novel PET tracer for imaging bacterial infection. *PLoS ONE* **2014**, *9*, e107951. [CrossRef]
423. Sellmyer, M.A.; Lee, I.; Hou, C.; Weng, C.C.; Li, S.; Lieberman, B.P.; Zeng, C.; Mankoff, D.A.; Mach, R.H. Bacterial infection imaging with [^{18}F]fluoropropyl-trimethoprim. *Proc. Natl. Acad. Sci. USA* **2017**, *114*, 8372–8377. [CrossRef]
424. Gowrishankar, G.; Hardy, J.; Wardak, M.; Namavari, M.; Reeves, R.E.; Neofytou, E.; Srinivasan, A.; Wu, J.C.; Contag, C.H.; Gambhir, S.S. Specific imaging of bacterial infection using 6″-^{18}F fluoromaltotriose: A second-generation PET tracer targeting the maltodextrin transporter in bacteria. *J. Nucl. Med.* **2017**, *58*, 1679–1684. [CrossRef]
425. Ordonez, A.A.; Weinstein, E.A.; Bambarger, L.E.; Saini, V.; Chang, Y.S.; DeMarco, V.P.; Klunk, M.H.; Urbanowski, M.E.; Moulton, K.L.; Murawski, A.M.; et al. A systematic approach for developing bacteria-specific imaging tracers. *J. Nucl. Med.* **2017**, *58*, 144–150. [CrossRef] [PubMed]
426. Mokaleng, B.B.; Ebenhan, T.; Ramesh, S.; Govender, T.; Kruger, H.G.; Parboosing, R.; Hazari, P.P.; Mishra, A.K.; Marjanovic-Painter, B.; Zeevaart, J.R.; et al. Synthesis, ^{68}Ga-radiolabeling, and preliminary in vivo assessment of a depsipeptide-derived compound as a potential PET/CT infection imaging agent. *BioMed. Res. Int.* **2015**, *2015*, 284354. [CrossRef] [PubMed]
427. Ebenhan, T.; Mokaleng, B.B.; Venter, J.D.; Kruger, H.G.; Zeevaart, J.R.; Sathekge, M. Preclinical assessment of a ^{68}Ga-DOTA functionalized depsipeptide as a radiodiagnostic infection imaging agent. *Molecules* **2017**, *22*, 1403. [CrossRef]
428. Dunlap, J.B.; Fan, G.; Leeborg, N.; Braziel, R.M. B-Cell Malignancies. In *Molecular Pathology in Clinical*; Leonard, D., Ed.; Springer: Cham, Switzerland, 2016; pp. 579–602. [CrossRef]
429. Wu, F.; Gao, J.; Kang, J.; Wang, X.; Niu, Q.; Liu, J.; Zhang, L. B cells in rheumatoid arthritis: Pathogenic mechanisms and treatment prospects. *Front. Immunol.* **2021**, *12*, 750753. [CrossRef]
430. Wekerle, H. B cells in multiple sclerosis. *Autoimmunity* **2017**, *50*, 57–60. [CrossRef]
431. Sospedra, M. B cells in multiple sclerosis. *Curr. Opin. Neurol.* **2018**, *31*, 256–262. [CrossRef]
432. Cencioni, M.T.; Mattoscio, M.; Magliozzi, R.; Bar-Or, A.; Muraro, P.A. B cells in multiple sclerosis—From targeted depletion to immune reconstitution therapies. *Nat. Rev. Neurol.* **2021**, *17*, 399–414. [CrossRef] [PubMed]
433. DeFuria, J.; Belkina, A.C.; Jagannathan-Bogdan, M.; Snyder-Cappione, J.; Carr, J.D.; Nersesova, Y.R.; Markham, D.; Strissel, K.J.; Watkins, A.A.; Zhu, M.; et al. B cells promote inflammation in obesity and type 2 diabetes through regulation of T-cell function and an inflammatory cytokine profile. *Proc. Natl. Acad. Sci. USA* **2013**, *110*, 5133–5138. [CrossRef] [PubMed]
434. Smith, M.J.; Simmons, K.M.; Cambier, J.C. B cells in type 1 diabetes mellitus and diabetic kidney disease. *Nat. Rev. Nephrol.* **2017**, *13*, 712–720. [CrossRef] [PubMed]
435. McManigle, W.; Youssef, A.; Sarantopoulos, S. B cells in chronic graft-versus-host disease. *Hum. Immunol.* **2019**, *80*, 393–399. [CrossRef]
436. Pal Singh, S.; Dammeijer, F.; Hendriks, R.W. Role of Bruton's tyrosine kinase in B cells and malignancies. *Mol. Cancer* **2018**, *17*, 57. [CrossRef]
437. Wen, T.; Wang, J.; Shi, Y.; Quin, H.; Liu, P. Inhibitors targeting Bruton's tyrosine kinase in cancers: Drug development advances. *Leukemia* **2021**, *35*, 312–332. [CrossRef]
438. Zhang, D.; Gong, H.; Meng, F. Recent Advances in BTK Inhibitors for the Treatment of Inflammatory and Autoimmune Diseases. *Molecules* **2021**, *26*, 4907. [CrossRef]
439. Arneson, L.C.; Carroll, K.J.; Ruderman, E.M. Bruton's Tyrosine Kinase Inhibition for the Treatment of Rheumatoid Arthritis. *Immunotargets Ther.* **2021**, *10*, 333–342. [CrossRef]
440. Contentti, E.C.; Correale, J. Bruton's tyrosine kinase inhibitors: A promising emerging treatment option for multiple sclerosis. *Expert Opin. Emerg. Drugs* **2020**, *25*, 377–381. [CrossRef]

MIM Software Inc. v. Progenics Pharmaceuticals, Inc.
IPR2025-00630
Progenics EX2017

441. Donnelly, D.J.; Preshlock, S.; Kaur, T.; Tran, T.; Wilson, T.C.; Mhanna, K.; Henderson, B.D.; Batalla, D.; Scott, P.J.H.; Shao, X. Synthesis of Radiopharmaceuticals via "In-Loop" ^{11}C-Carbonylation as Exemplified by the Radiolabeling of Inhibitors of Bruton's Tyrosine Kinase. *Front. Nucl. Med.* **2022**, *1*, 820235. [CrossRef]
442. Hatori, A.; Yui, J.; Yamasaki, T.; Xie, L.; Kumata, K.; Fujinaga, M.; Yoshida, Y.; Ogawa, M.; Nengaki, N.; Kawamura, K.; et al. PET imaging of lung inflammation with [^{18}F]FEDAC, a radioligand for translocator protein (18 kDa). *PLoS ONE* **2012**, *7*, e45065. [CrossRef] [PubMed]
443. Hannestad, J.; Gallezot, J.D.; Schafbauer, T.; Lim, K.; Kloczynski, T.; Morris, E.D.; Carson, R.E.; Ding, Y.S.; Cosgrove, K.P. Endotoxin-induced systemic inflammation activates microglia: [^{11}C]PBR28 positron emission tomography in nonhuman primates. *NeuroImage* **2012**, *63*, 232–239. [CrossRef] [PubMed]
444. Ching, A.S.; Kuhnast, B.; Damont, A.; Roeda, D.; Tavitian, B.; Dolle, F. Current paradigm of the 18-kDa translocator protein (TSPO) as a molecular target for PET imaging in neuroinflammation and neurodegenerative diseases. *Insights Imaging* **2012**, *3*, 111–119. [CrossRef] [PubMed]
445. Dedeurwaerdere, S.; Callaghan, P.D.; Pham, T.; Rahardjo, G.L.; Amhaoul, H.; Berghofer, P.; Quinlivan, M.; Mattner, F.; Loc'h, C.; Katsifis, A.; et al. PET imaging of brain inflammation during early epileptogenesis in a rat model of temporal lobe epilepsy. *EJNMMI Res.* **2012**, *2*, 60. [CrossRef] [PubMed]
446. Maecke, H.R.; Reubi, J.C. Somatostatin receptors as targets for nuclear medicine imaging and radionuclide treatment. *J. Nucl. Med.* **2011**, *52*, 841–844. [CrossRef] [PubMed]
447. Di Gialleonardo, V.; Signore, A.; Willemsen, A.T.; Sijbesma, J.W.; Dierckx, R.A.; de Vries, E.F. Pharmacokinetic modeling of N-(4-[^{18}F]fluorobenzoyl)interleukin-2 binding to activated lymphocytes in an xenograft model of inflammation. *Eur. J. Nucl. Med. Mol. Imaging* **2012**, *39*, 1551–1560. [CrossRef] [PubMed]
448. Fotis, L.; Agrogiannis, G.; Vlachos, I.S.; Pantopoulou, A.; Margoni, A.; Kostaki, M.; Verikokos, C.; Tzivras, D.; Mikhailidis, D.P.; Perrea, D. Intercellular adhesion molecule (ICAM)-1 and vascular cell adhesion molecule (VCAM)-1 at the early stages of atherosclerosis in a rat model. *In Vivo* **2012**, *26*, 243–250.
449. Douglas, A.P.; Thursky, K.A.; Worth, L.J.; Drummond, E.; Hogg, A.; Hicks, R.J.; Slavin, M.A. FDG PET/CT imaging in detecting and guiding management of invasive fungal infections: A retrospective comparison to conventional CT imaging. *Eur. J. Nucl. Med. Mol. Imaging* **2019**, *46*, 166–173. [CrossRef]
450. Leroy-Freschini, B.; Treglia, G.; Argemi, X.; Bund, C.; Kessler, R.; Herbrecht, R.; Imperiale, A. 18 F-FDG PET/CT for invasive fungal infection in immunocompromised patients. *QJM Int. J. Med.* **2018**, *111*, 613–622. [CrossRef]
451. Ankrah, O.A.; Span, L.F.R.; Klein, H.C.; de Jong, P.A.; Dierckx, R.A.J.O.; Kwee, T.C.; Sathekge, M.M.; Glaudemans, A.W.J.M. Role of FDG PET/CT in monitoring treatment response in patients with invasive fungal infections. *Eur. J. Nucl. Med. Mol. Imaging* **2019**, *46*, 174–183. [CrossRef]
452. Fuchs, M.; Briel, M.; Daikeler, T.; Walker, U.A.; Rasch, H.; Berg, S.; Ng, Q.K.; Raatz, H.; Jayne, D.; Kötter, I.; et al. The impact of 18 F-FDG PET on the management of patients with suspected large vessel vasculitis. *Eur. J. Nucl. Med. Mol. Imaging* **2012**, *39*, 344–353. [CrossRef] [PubMed]
453. Einspieler, I.; Thürmel, K.; Pyka, T.; Eiber, M.; Wolfram, S.; Moog, P.; Reeps, C.; Essler, M. Imaging large vessel vasculitis with fully integrated PET/MRI: A pilot study. *Eur. J. Nucl. Med. Mol. Imaging* **2015**, *42*, 1012–1024. [CrossRef] [PubMed]
454. Pijl, J.P.; Kwee, T.C.; Slart, R.H.J.A.; Glaudemans, A.W.J.M. PET/CT Imaging for Personalized Management of Infectious Diseases. *J. Pers. Med.* **2021**, *11*, 133. [CrossRef] [PubMed]
455. Bier, G.; Hoffmann, V.; Kloth, C.; Othman, A.E.; Eigentler, T.; Garbe, C.; La Fougère, C.; Pfannenberg, C.; Nikolaou, K.; Klumpp, B. CT imaging of bone and bone marrow infiltration in malignant melanoma—Challenges and limitations for clinical staging in comparison to 18 FDG-PET/CT. *Eur. J. Radiol.* **2016**, *85*, 732–738. [CrossRef]
456. Kong, B.Y.; Menzies, A.M.; Saunders, C.A.; Liniker, E.; Ramanujam, S.; Guminski, A.; Kefford, R.F.; Long, G.V.; Carlino, M.S. Residual FDG-PET metabolic activity in metastatic melanoma patients with prolonged response to anti-PD-1 therapy. *Pigment Cell Melanoma Res.* **2016**, *29*, 572–577. [CrossRef]
457. Hueting, R. Radiocopper for the imaging of copper metabolism. *J. Labelled Comp. Radiopharm.* **2014**, *57*, 231–238. [CrossRef]
458. Werry, E.L.; Bright, F.M.; Piguet, O.; Ittner, L.M.; Halliday, G.M.; Hodges, J.R.; Kiernan, M.C.; Loy, C.T.; Kril, J.J. and Kassiou, M. Recent Developments in TSPO PET Imaging as A Biomarker of Neuroinflammation in Neurodegenerative Disorders. *Int. J. Mol. Sci.* **2019**, *20*, 3161. [CrossRef]
459. Narayanaswami, V.; Dahl, K.; Bernard-Gauthier, V.; Josephson, L.; Cumming, P.; Vasdev, N. Emerging PET Radiotracers and Targets for Imaging of Neuroinflammation in Neurodegenerative Diseases: Outlook Beyond TSPO. *Mol. Imaging* **2018**, *17*, 1536012118792317. [CrossRef]
460. Fujita, M.; Kobayashi, M.; Ikawa, M.; Gunn, R.N.; Rabiner, E.A.; Owen, D.R.; Zoghbi, S.S.; Haskali, M.B.; Telu, S.; Pike, V.W.; et al. Comparison of four 11C-labeled PET ligands to quantify translocator protein 18kDa (TSPO) in human brain: (R)-PK11195, PBR28, DPA-713, and ER176-based on recent publications that measured specific-to-non-displaceable ratios. *EJNMMI Res.* **2017**, *7*, 84. [CrossRef]
461. Boutin, H.; Murray, K.; Pradillo, J.; Maroy, R.; Smigova, A.; Gerhard, A.; Jones, P.A.; Trigg, W. 18F-GE-180: A novel TSPO radiotracer compared to 11C-R-PK11195 in a preclinical model of stroke. *Eur. J. Nucl. Med. Mol. Imaging* **2015**, *42*, 503–511. [CrossRef]

MIM Software Inc. v. Progenics Pharmaceuticals, Inc.
IPR2025-00630
Progenics EX2017

462. Ikawa, M.; Lohith, T.G.; Shrestha, S.; Telu, S.; Zoghbi, S.S.; Castellano, S.; Taliani, S.; Da Settimo, F.; Fujita, M.; Pike, V.W.; et al. 11C-ER176, a Radioligand for 18-kDa Translocator Protein, Has Adequate Sensitivity to Robustly Image All Three Affinity Genotypes in Human Brain. *J. Nucl. Med.* **2017**, *58*, 320–325. [CrossRef] [PubMed]
463. Liu, B.; Le, K.X.; Park, M.A.; Wang, S.; Belanger, A.P.; Dubey, S.; Frost, J.L.; Holton, P.; Reiser, V.; Jones, P.A.; et al. In Vivo Detection of Age- and Disease-Related Increases in Neuroinflammation by 18F-GE180 TSPO MicroPET Imaging in Wild-Type and Alzheimer's Transgenic Mice. *J. Neurosci.* **2015**, *35*, 15716–15730. [CrossRef] [PubMed]
464. Lopez-Picon, F.R.; Snellman, A.; Eskola, O.; Helin, S.; Solin, O.; Haaparanta-Solin, M.; Rinne, J.O. Neuroinflammation Appears Early on PET Imaging and Then Plateaus in a Mouse Model of Alzheimer Disease. *J. Nucl. Med.* **2018**, *59*, 509–515. [CrossRef]
465. Chaney, A.; Cropper, H.C.; Johnson, E.M.; Lechtenberg, K.J.; Peterson, T.C.; Stevens, M.Y.; Buckwalter, M.S.; James, M.L. 11 C-DPA-713 Versus 18F-GE-180: A Preclinical Comparison of Translocator Protein 18 kDa PET Tracers to Visualize Acute and Chronic Neuroinflammation in a Mouse Model of Ischemic Stroke. *J. Nucl. Med.* **2019**, *60*, 122–128. [CrossRef] [PubMed]
466. Unterrainer, M.; Mahler, C.; Vomacka, L.; Lindner, S.; Havla, J.; Brendel, M.; Boning, G.; Ertl-Wagner, B.; Kumpfel, T.; Milenkovic, V.M.; et al. TSPO PET with [^{18}F]GE-180 sensitively detects focal neuroinflammation in patients with relapsing-remitting multiple sclerosis. *Eur. J. Nucl. Med. Mol. Imaging* **2018**, *45*, 1423–1431. [CrossRef] [PubMed]
467. Sridharan, S.; Raffel, J.; Nandoskar, A.; Record, C.; Brooks, D.J.; Owen, D.; Sharp, D.; Muraro, P.A.; Gunn, R.; Nicholas, R. Confirmation of Specific Binding of the 18-kDa Translocator Protein (TSPO) Radioligand [^{18}F]GE-180: A Blocking Study Using XBD173 in Multiple Sclerosis Normal Appearing White and Grey Matter. *Mol. Imaging Biol.* **2019**, *21*, 935–944. [CrossRef] [PubMed]
468. Zanotti-Fregonara, P.; Veronese, M.; Pascual, B.; Rostomily, R.C.; Turkheimer, F.; Masdeu, J.C. The validity of 18F-GE180 as a TSPO imaging agent. *Eur. J. Nucl. Med. Mol. Imaging* **2019**, *46*, 1205–1207. [CrossRef]
469. Tremoleda, J.L.; Thau-Zuchman, O.; Davies, M.; Foster, J.; Khan, I.; Vadivelu, K.C.; Yip, P.K.; Sosabowski, J.; Trigg, W.; Michael-Titus, A.T. In vivo PET imaging of the neuroinflammatory response in rat spinal cord injury using the TSPO tracer [^{18}F]GE-180 and effect of docosahexaenoic acid. *Eur. J. Nucl. Med. Mol. Imaging* **2016**, *43*, 1710–1722. [CrossRef]
470. James, M.L.; Belichenko, N.P.; Shuhendler, A.J.; Hoehne, A.; Andrews, L.E.; Condon, C.; Nguyen, T.V.; Reiser, V.; Jones, P.; Trigg, W.; et al. [^{18}F]GE-180 PET Detects Reduced Microglia Activation After LM11A-31 Therapy in a Mouse Model of Alzheimer's Disease. *Theranostics* **2017**, *7*, 1422–1436. [CrossRef]
471. Sridharan, S.; Lepelletier, F.X.; Trigg, W.; Banister, S.; Reekie, T.; Kassiou, M.; Gerhard, A.; Hinz, R.; Boutin, H. Comparative Evaluation of Three TSPO PET Radiotracers in a LPS-Induced Model of Mild Neuroinflammation in Rats. *Mol. Imaging Biol.* **2017**, *19*, 77–89. [CrossRef]
472. Yoder, K.K.; Nho, K.; Risacher, S.L.; Kim, S.; Shen, L.; Saykin, A.J. Influence of TSPO genotype on 11C-PBR28 standardized uptake values. *J. Nucl. Med.* **2013**, *54*, 1320–1322. [CrossRef] [PubMed]
473. Zurcher, N.R.; Loggia, M.L.; Lawson, R.; Chonde, D.B.; Izquierdo-Garcia, D.; Yasek, J.E.; Akeju, O.; Catana, C.; Rosen, B.R.; Cudkowicz, M.E.; et al. Increased in vivo glial activation in patients with amyotrophic lateral sclerosis: Assessed with [^{11}C]-PBR28. *Neuroimage Clin.* **2015**, *7*, 409–414. [CrossRef] [PubMed]
474. Kreisl, W.C.; Lyoo, C.H.; Liow, J.S.; Wei, M.; Snow, J.; Page, E.; Jenko, K.J.; Morse, C.L.; Zoghbi, S.S.; Pike, V.W.; et al. 11C-PBR28 binding to translocator protein increases with progression of Alzheimer's disease. *Neurobiol. Aging* **2016**, *44*, 53–61. [CrossRef] [PubMed]
475. Datta, G.; Colasanti, A.; Kalk, N.; Owen, D.; Scott, G.; Rabiner, E.A.; Gunn, R.N.; Lingford-Hughes, A.; Malik, O.; Ciccarelli, O.; et al. 11C-PBR28 and 18F-PBR111 Detect White Matter Inflammatory Heterogeneity in Multiple Sclerosis. *J. Nucl. Med.* **2017**, *58*, 1477–1482. [CrossRef] [PubMed]
476. Banati, R.B.; Middleton, R.J.; Chan, R.; Hatty, C.R.; Kam, W.W.; Quin, C.; Graeber, M.B.; Parmar, A.; Zahra, D.; Callaghan, P.; et al. Positron emission tomography and functional characterization of a complete PBR/TSPO knockout. *Nat. Commun.* **2014**, *5*, 5452. [CrossRef]
477. Mirzaei, N.; Tang, S.P.; Ashworth, S.; Coello, C.; Plisson, C.; Passchier, J.; Selvaraj, V.; Tyacke, R.J.; Nutt, D.J.; Sastre, M. In vivo imaging of microglial activation by positron emission tomography with [^{11}C]PBR28 in the 5XFAD model of Alzheimer's disease. *Glia* **2016**, *64*, 993–1006. [CrossRef]
478. Simmons, D.A.; James, M.L.; Belichenko, N.P.; Semaan, S.; Condon, C.; Kuan, J.; Shuhendler, A.J.; Miao, Z.; Chin, F.T.; Longo, F.M. TSPO-PET imaging using [^{18}F]PBR06 is a potential translatable biomarker for treatment response in Huntington's disease: Preclinical evidence with the p75NTR ligand LM11A-31. *Hum. Mol. Genet.* **2018**, *27*, 2893–2912. [CrossRef]
479. Owen, D.R.; Yeo, A.J.; Gunn, R.N.; Song, K.; Wadsworth, G.; Lewis, A.; Rhodes, C.; Pulford, D.J.; Bennacef, I.; Parker, C.A.; et al. An 18-kDa translocator protein (TSPO) polymorphism explains differences in binding affinity of the PET radioligand PBR28. *J. Cereb. Blood Flow Metab.* **2012**, *32*, 1–5. [CrossRef]
480. Guo, Q.; Colasanti, A.; Owen, D.R.; Onega, M.; Kamalakaran, A.; Bennacef, I.; Matthews, P.M.; Rabiner, E.A.; Turkheimer, F.E.; Gunn, R.N. Quantification of the specific translocator protein signal of 18F-PBR111 in healthy humans: A genetic polymorphism effect on in vivo binding. *J. Nucl. Med.* **2013**, *54*, 1915–1923. [CrossRef]
481. Colasanti, A.; Guo, Q.; Muhlert, N.; Giannetti, P.; Onega, M.; Newbould, R.D.; Ciccarelli, O.; Rison, S.; Thomas, C.; Nicholas, R.; et al. In Vivo Assessment of Brain White Matter Inflammation in Multiple Sclerosis with 18 F-PBR111 PET. *J. Nucl. Med.* **2014**, *55*, 1112–1118. [CrossRef]

MIM Software Inc. v. Progenics Pharmaceuticals, Inc.
IPR2025-00630
Progenics EX2017

482. Takano, A.; Piehl, F.; Hillert, J.; Varrone, A.; Nag, S.; Gulyas, B.; Stenkrona, P.; Villemagne, V.L.; Rowe, C.C.; Macdonell, R.; et al. In vivo TSPO imaging in patients with multiple sclerosis: A brain PET study with [^{18}F]FEDAA1106. *EJNMMI Res.* **2013**, *3*, 30. [CrossRef] [PubMed]
483. Varrone, A.; Mattsson, P.; Forsberg, A.; Takano, A.; Nag, S.; Gulyas, B.; Borg, J.; Boellaard, R.; Al-Tawil, N.; Eriksdotter, M.; et al. In vivo imaging of the 18-kDa translocator protein (TSPO) with [^{18}F]FEDAA1106 and PET does not show increased binding in Alzheimer's disease patients. *Eur. J. Nucl. Med. Mol. Imaging* **2013**, *40*, 921–931. [CrossRef] [PubMed]
484. Yasuno, F.; Kosaka, J.; Ota, M.; Higuchi, M.; Ito, H.; Fujimura, Y.; Nozaki, S.; Takahashi, S.; Mizukami, K.; Asada, T.; et al. Increased binding of peripheral benzodiazepine receptor in mild cognitive impairment-dementia converters measured by positron emission tomography with [^{11}C]DAA1106. *Psychiatry Res.* **2012**, *203*, 67–74. [CrossRef] [PubMed]
485. Bernard-Gauthier, V.; Mossine, A.V.; Mahringer, A.; Aliaga, A.; Bailey, J.J.; Shao, X.; Stauff, J.; Arteaga, J.; Sherman, P.; Grand'Maison, M.; et al. Identification of [^{18}F]TRACK, a fluorine-18-labeled tropomyosin receptor kinase (Trk) inhibitor for PET imaging. *J. Med. Chem.* **2018**, *61*, 1737–1743. [CrossRef]
486. Mossine, A.V.; Brooks, A.F.; Makaravage, K.J.; Miller, J.M.; Ichiishi, N.; Sanford, M.S.; Scott, P.J.H. Synthesis of [^{18}F]Arenes via the copper-mediated [^{18}F]Fluorination of boronic acids. *Org. Lett.* **2015**, *17*, 5780–5783. [CrossRef]
487. Sasaki, T.; Hiroki, K.; Yamashita, Y. The role of epidermal growth factor receptor in cancer metastasis and microenvironment. *BioMed. Res. Int.* **2013**, *2013*, 546318. [CrossRef]
488. Song, Y.; Xiao, Z.; Wang, K.; Wang, X.; Zhang, C.; Fang, F.; Sun, X.; Shen, B. Development and evaluation of 18F-IRS for molecular imaging mutant EGF receptors in NSCLC. *Sci. Rep.* **2017**, *7*, 3121. [CrossRef]
489. Su, Z.; Herholz, K.; Gerhard, A.; Roncaroli, F.; Du Plessis, D.; Jackson, A.; Turkheimer, F.; Hinz, R. [^{11}C]-(R)PK11195 tracer kinetics in the brain of glioma patients and a comparison of two referencing approaches. *Eur. J. Nucl. Med. Mol. Imaging* **2013**, *40*, 1406–1419. [CrossRef]
490. Sellmyer, M.A.; Lee, I.; Hou, C.; Lieberman, B.P.; Zeng, C.; Mankoff, D.A.; Mach, R.H. Quantitative PET reporter gene imaging with [^{11}C]Trimethoprim. *Mol. Therapy* **2017**, *25*, 120–126. [CrossRef]
491. Nepal, P.; Rodrigue, P.; Olsavsky, T. 18F-fluciclovine (Axumin) PET/CT detecting occult bone metastasis. *Egypt J. Radiol. Nucl. Med.* **2020**, *51*, 142. [CrossRef]
492. Strebl, M.G.; Wang, C.; Schroeder, F.A.; Placzek, M.S.; Wey, H.-Y.; Van de Bittner, G.C.; Neelamegam, R.; Hooker, J.M. Development of a fluorinated class-I HDAC radiotracer reveals key chemical determinants of brain penetrance. *ACS Chem. Neurosci.* **2016**, *7*, 528–533. [CrossRef] [PubMed]
493. Tegnebratt, T.; Lu, L.; Eksborg, S.; Chireh, A.; Damberg, P.; Nikkhou-Aski, S.; Foukakis, T.; Rundqvist, H.; Holmin, S.; Kuiper, R.V. Treatment response assessment with (R)-[11CPAQ PET in the MMTV-PyMT mouse model of breast cancer. *EJNMMI Res.* **2018**, *8*, 25. [CrossRef] [PubMed]
494. Toyohara, J. Evaluation of DNA synthesis with carbon-11-labeled 4′-thiothymidine. *World. J. Radiol.* **2016**, *8*, 799. [CrossRef] [PubMed]
495. Okochi, Y.; Nihashi, T.; Fujii, M.; Kato, K.; Okada, Y.; Ando, Y.; Maesawa, S.; Takebayashi, S.; Wakabayashi, T.; Naganawa, S. Clinical use of 11C-methionine and 18F-FDG-PET for germinoma in central nervous system. *Ann. Nucl. Med.* **2014**, *28*, 94–102. [CrossRef] [PubMed]
496. Mariani, G.; Bruselli, L.; Kuwert, T.; Kim, E.E.; Flotats, A.; Israel, O.; Dondi, M.; Watanabe, N. A review on the clinical uses of SPECT/CT. *Eur. J. Nucl. Med. Mol. Imaging* **2010**, *37*, 1959–1985. [CrossRef]
497. Papagiannopoulou, D. Technetium-99m radiochemistry for pharmaceutical applications. *J. Labelled Comp. Radiopharm.* **2017**, *60*, 502–520. [CrossRef]
498. Imbert, L.; Poussier, S.; Franken, P.R.; Songy, B.; Verger, A.; Morel, O.; Wolf, D.; Noel, A.; Karcher, G.; Marie, P.-Y. Compared performance of high-sensitivity cameras dedicated to myocardial perfusion SPECT: A comprehensive analysis of phantoms and human images. *J. Nucl. Med.* **2012**, *53*, 1897–1903. [CrossRef]
499. Goshen, E.; Beilin, L.; Stern, E.; Kenig, T.; Goldkorn, R.; Ben-Haim, S. Feasibility study of a novel general purpose CZT-based digital SPECT camera: Initial clinical results. *EJNMMI Phys.* **2018**, *5*, 6. [CrossRef]
500. Hutton, B.F.; Erlandsson, K.; Thielemans, K. Advances in clinical molecular imaging instrumentation. *Clin. Translat. Imaging* **2018**, *6*, 31–45. [CrossRef]
501. Ljungberg, M.; Pretorius, P.H. SPECT/CT: An update on technological developments and clinical applications. *Br. J. Radiol.* **2018**, *91*, 20160402. [CrossRef]
502. Bordonne, M.; Chawki, M.B.; Marie, P.-Y.; Zaragori, T.; Roch, V.; Grignon, R.; Imbert, L. High-quality brain perfusion SPECT images may be achieved with a high-speed recording using CZT camera. *EJNMMI Phys.* **2020**, *7*, 65. [CrossRef] [PubMed]
503. Cantoni, V.; Green, R.; Ricciardi, C.; Assante, R.; Zampella, E.; Nappi, C.; Gaudieri, V.; Mannarino, T.; Genova, A.; De Simini, G.; et al. A machine learning-based approach to directly compare the diagnostic accuracy of myocardial perfusion imaging by conventional and cadmium zinc telluride SPECT. *J. Nucl. Cardiol.* **2022**, *29*, 46–55. [CrossRef] [PubMed]
504. Rezazadeh, F.; Sadeghzadeh, N. Tumor targeting with ^{99m}Tc radiolabeled peptides: Clinical application and recent development. *Chem. Biol. Drug Des.* **2018**, *93*, 205–221. [CrossRef] [PubMed]
505. Fani, M.; Mansi, R.; Nicolas, G.P.; Wild, D. Radiolabeled Somatostatin Analogs—A Continuously Evolving Class of Radiopharmaceuticals. *Cancers* **2022**, *14*, 1172. [CrossRef] [PubMed]

MIM Software Inc. v. Progenics Pharmaceuticals, Inc.
IPR2025-00630
Progenics EX2017

506. Brabander, T.; Kwekkeboom, D.J.; Feelders, R.A.; Brouwers, A.H.; Teunissen, J.A.M. Nuclear Medicine Imaging of Neuroendocrine Tumors. *Front. Horm. Res.* **2015**, *44*, 73–87. [CrossRef] [PubMed]
507. Makris, G.; Radford, L.L.; Kuchuk, M.; Gallazzi, F.; Jurisson, S.S.; Smith, C.J.; Hennkens, H.M. NOTA and NODAGA [^{99m}Tc]Tc- and [^{186}Re]Re-Tricarbonyl Complexes: Radiochemistry and First Example of a [^{99m}Tc]Tc-NODAGA Somatostatin Receptor-Targeting Bioconjugate. *Bioconjug. Chem.* **2018**, *29*, 4040–4049. [CrossRef] [PubMed]
508. Makris, G.; Kuchuk, M.; Gallazzi, F.; Jurisson, S.S.; Smith, C.J.; Hennkens, H.M. Somatostatin receptor targeting with hydrophilic [^{99m}Tc/^{186}Re]Tc/Re-tricarbonyl NODAGA and NOTA complexes. *Nucl. Med. Biol.* **2019**, *71*, 39–46. [CrossRef]
509. Abiraj, K.; Ursillo, S.; Tamma, M.L.; Rylova, S.N.; Waser, B.; Constable, E.C.; Fani, M.; Nicolas, G.P.; Reubi, J.C.; Maecke, H.R. The tetraamine chelator outperforms HYNIC in a new technetium HYNIC in a new technetium-99m-labelled somatostatin receptor 2 antagonist. *EJNMMI Res.* **2018**, *8*, 75. [CrossRef]
510. Fani, M.; Weingaertner, V.; Peitl, P.K.; Mansi, R.; Gaonkar, R.H.; Garnuszek, P.; Mikolajczak, R.; Novak, D.; Simoncic, U.; Hubalewska-Dydejczyk, A.; et al. Selection of the First ^{99m}Tc-Labelled Somatostatin Receptor Subtype 2 Antagonist for Clinical Translation—Preclinical Assessment of Two Optimized Candidates. *Pharmaceuticals* **2021**, *14*, 19. [CrossRef]
511. Gaonkar, R.H.; Wiesmann, F.; Del Pozzo, L.; Mcdougall, L.; Zanger, S.; Mikolajczak, R.; Mansi, R.; Fani, M. SPECT Imaging of SST2-Expressing Tumors with ^{99m}Tc-Based Somatostatin Receptor Antagonists: The Role of Tetraamine, HYNIC, and Spacers. *Pharmaceuticals* **2021**, *14*, 300. [CrossRef]
512. Afshar-Oromieh, A.; Babich, J.W.; Kratochwil, C.; Giesel, F.L.; Eisenhut, M.; Kopka, K.; Haberkorn, U. The Rise of PSMA Ligands for Diagnosis and Therapy of Prostate Cancer. *J. Nucl. Med.* **2016**, *57*, 79S–89S. [CrossRef] [PubMed]
513. Wester, H.J.; Schottelius, M. PSMA-Targeted Radiopharmaceuticals for Imaging and Therapy. *Semin. Nucl. Med.* **2019**, *49*, 302–312. [CrossRef] [PubMed]
514. Barret, J.A.; Coleman, E.; Goldsmith, S.J.; Vallabhajosula, S.; Petry, N.A.; Cho, S.; Armor, T.; Stubbs, J.B.; Maresca, K.P.; Stabin, M.G.; et al. First-in-Man Evaluation of 2 High-Affinity PSMA-Avid Small Molecules for Imaging Prostate Cancer. *J. Nucl. Med.* **2013**, *54*, 380–387. [CrossRef] [PubMed]
515. Zechmann, C.M.; Afshar-Oromieh, A.; Armor, T.; Stubbs, J.B.; Mier, W.; Hadaschik, B.; Joyal, J.; Kopka, K.; Debus, J.; Babich, J.W.; et al. Radiation dosimetry and first therapy results with a ^{124}I/^{131}I-labeled small molecule (MIP-1095) targeting PSMA for prostate cancer therapy. *Eur. J. Nucl. Med. Mol. Imaging* **2014**, *41*, 1280–1292. [CrossRef]
516. Afshar-Oromieh, A.; Haberkorn, U.; Zechmann, C.; Armor, T.; Mier, W.; Spohn, F.; Debus, N.; Holland-Letz, T.; Babich, J.; Kratochwill, C. Repeated PSMA-targeting radioligand therapy of metastatic prostate cancer with ^{131}I-MIP-1095. *Eur. J. Nucl. Med. Mol. Imaging* **2017**, *44*, 950–959. [CrossRef]
517. Hillier, S.M.; Maresca, K.P.; Lu, G.; Merkin, R.D.; Marquis, J.C.; Zimmerman, C.N.; Eckelman, W.C.; Joyal, J.L.; Babich, J.W. ^{99m}Tc-Labeled Small-Molecule Inhibitors of Prostate-Specific Membrane Antigen for Molecular Imaging of Prostate Cancer. *J. Nucl. Med.* **2013**, *54*, 1369–1376. [CrossRef]
518. Lu, G.; Maresca, K.P.; Hillier, S.H.; Zimmerman, C.N.; Eckelman, W.C.; Joyal, J.J.; Babich, J.W. Synthesis and SAR of ^{99m}Tc/Re-labeled small molecule prostate specific membrane antigen inhibitors with novel polar chelates. *Bioorg. Med. Chem. Lett.* **2013**, *23*, 1557–1563. [CrossRef]
519. Xu, X.; Zhang, J.; Hu, S.; He, S.; Bao, X.; Ma, G.; Luo, J.; Cheng, J.; Zhang, Y. ^{99m}Tc-labeling and evaluation of a HYNIC modified small-molecular inhibitor of prostate specific membrane antigen. *Nucl. Med. Biol.* **2017**, *48*, 69–75. [CrossRef]
520. Ferro-Flores, G.; Luna-Gutiérrez, M.; Ocampo-García, B.; Santos-Cueves, C.; Azorín-Vega, E.; Jiménez-Mancilla, N.; Orocio-Rodríguez, E.; Davanzo, J.; García-Pérez, F.O. Clinical translation of a PSMA inhibitor for ^{99m}Tc-based SPECT. *Nucl. Med. Biol.* **2017**, *48*, 36–44. [CrossRef]
521. Santos-Cuevas, C.; Davazo, J.; Ferro-Flores, G.; García-Pérez, F.O.; Ocampo-García, B.; Ignacio-Alvarez, E.; Gómez-Argumosa, E.; Pedraza-López, M. ^{99m}Tc-labeled PSMA inhibitor: Biokinetics and radiation dosimetry in healthy subjects and imaging of prostate cancer tumors in patients. *Nucl. Med. Biol.* **2017**, *52*, 1–6. [CrossRef]
522. García-Pérez, F.O.; Davazo, J.; López-Buenrostro, S.; Santos-Cuevas, C.; Ferro-Flores, G.; Jímenez-Ríos, A.; Scavuzzo, A.; Santana-Ríos, Z.; Medina-Ornelas, S. Head to head comparison of performance of 99m Tc-EDDA/HYNICiPSMA SPECT/CT and 68 Ga-PSMA-11 PET/CT a prospective study in biochemical recurrence prostate cancer patients. *Am. J. Nucl. Med. Mol. Imaging* **2018**, *8*, 332–340. [PubMed]
523. Lawal, I.O.; Ankrah, A.O.; Mokgoro, N.; Vorster, M.; Maes, A.; Satheke, M.M. Diagnostic sensitivity of Tc-99m HYNIC PSMA SPECT/CT in prostate carcinoma: A comparative analysis with Ga-68 PSMA PET/CT. *Prostate* **2017**, *77*, 1205–1212. [CrossRef] [PubMed]
524. Robu, S.; Schottelius, M.; Eiber, M.; Maurer, T.; Gschwend, M.; Wester, H.-J. Preclinical Evaluation and First Patient Application of ^{99m}Tc-PSMA-I&S for SPECT Imaging and Radioguided Surgery in Prostate Cancer. *J. Nucl. Med.* **2017**, *58*, 235–242. [CrossRef] [PubMed]
525. Knipper, S.; Tilki, D.; Mansholt, J.; Berliner, C.; Bernreuther, C.; Steuber, T.; Maurer, T.; Graefen, M. Metastases-yield and Prostate-specific Antigen Kinetics Following Salvage Lymph Node Dissection for Prostate Cancer: A Comparison between Conventional Surgical Approach and Prostate-specific Membrane Antigen-radioguided Surgery. *Eur. Urol. Focus* **2019**, *5*, 50–53. [CrossRef]

MIM Software Inc. v. Progenics Pharmaceuticals, Inc.
IPR2025-00630
Progenics EX2017

526. Cimadamore, A.; Cheng, M.; Santoni, M.; Lopez-Beltran, A.; Battelli, N.; Massari, F.; Galosi, A.B.; Scarpelli, M.; Montironi, R. New Prostate Cancer Targets for Diagnosis, Imaging, and Therapy: Focus on Prostate-Specific Membrane Antigen. *Front. Oncol.* **2018**, *8*, 653. [CrossRef]
527. Evazalipour, M.; D'Huyvetter, M.; Tehrani, B.S.; Abolhassani, M.; Omidfar, K.; Abdoli, S.; Arezumand, R.; Morovvati, H.; Lahoutte, T.; Muyldermans, S.; et al. Generation and characterization of nanobodies targeting PSMA for molecular imaging of prostate cancer. *Contrast Media Mol. Imaging* **2014**, *9*, 211–220. [CrossRef]
528. Cook, G.J.R.; Azad, G.K.; Taylor, B.P.; Lee, E.; Morrison, M.S.; Hughes, S.; Morris, S.; Rudman, S.; Chowdhury, S.; Goh, V. Imaging $\alpha_v\beta_3$ integrin expression in skeletal metastases with ^{99m}Tc-maraciclatide single-photon emission computed tomography: Detection and therapy response assessment. *Eur. J. Nucl. Med. Mol. Imaging* **2018**, *45*, 898–903. [CrossRef]
529. Zhu, Z.; Miao, W.; Li, Q.; Dai, H.; Ma, Q.; Wang, F.; Yang, A.; Jia, B.; Jing, X.; Liu, S.; et al. ^{99m}Tc-3PRGD$_2$ for integrin receptor imaging of lung cancer: A multicenter study. *J. Nucl. Med.* **2012**, *53*, 716–722. [CrossRef]
530. Ma, Q.; Chen, B.; Gao, S.; Ji, T.; Wen, Q.; Song, Y.; Zhu, L.; Xu, Z.; Liu, L. ^{99m}Tc-3P$_4$-RGD$_2$ Scintimammography in the Assessment of Breast Lesions: Comparative Study with ^{99m}Tc-MIBI. *PLoS ONE* **2014**, *9*, e108349. [CrossRef]
531. Liu, L.; Song, Y.; Gao, S. ^{99m}Tc-3PRGD$_2$ Scintimammography in Palpable and Non-palpable Breast Lesions. *Mol. Imaging* **2014**, *13*, 5. [CrossRef]
532. Zhao, D.; Jin, X.; Li, F.; Liang, J.; Lin, Y. Integrin $\alpha_v\beta_3$ Imaging of Radioactive Iodine-Refractory Thyroid Cancer Using ^{99m}Tc-3PRGD2. *J. Nucl. Med.* **2012**, *53*, 1872–1877. [CrossRef] [PubMed]
533. Miao, W.; Zheng, S.; Dai, H.; Wang, F.; Jin, X.; Zhu, Z.; Jia, B. Comparison of 99mTc-3prgd2 integrin receptor imaging with 99mTc-MDP bone scan in diagnosis of bone metastasis in patients with lung cancer: A multicenter study. *PLoS ONE* **2014**, *22*, e111221. [CrossRef] [PubMed]
534. Chen, Z.; Fu, F.; Li, F.; Zhu, Z.; Yang, Y.; Chen, X.; Jia, B.; Zheng, S.; Huang, C.; Miao, W. Comparison of [^{99m}Tc]3PRGD$_2$ Imaging and [^{18}F]FDG PET/CT in Breast Cancer and Expression of Integrin $\alpha_v\beta_3$ in Breast cancer Vascular Endothelial Cells. *Mol. Imaging Biol.* **2018**, *20*, 846–856. [CrossRef] [PubMed]
535. Zheng, S.; Chen, Z.; Huang, C.; Chen, Y.; Miao, W. [^{99m}Tc]3PRGD$_2$ for integrin receptor imaging of esophageal cancer: A comparative study with [^{18}F]FDG PET/CT. *Ann. Nucl. Med.* **2019**, *33*, 135–143. [CrossRef] [PubMed]
536. Watson, D.D.; Glover, D.K. Chapter—1 Overview of Tracer Kinetics and Cellular Mechanism of Uptake. In *Clinical Nuclear Cardiology*, 4th ed.; Elsevier: Amsterdam, The Netherlands, 2010; pp. 3–13. ISBN 9780323057967.
537. Crișan, G.; Macea, A.M.; Andrieș, G.; Chiș, V. Experimental and computational Raman spectroscopies applied to 2-methoxy-2-methylpropylisonitrile (MIBI) ligand of the 99mTc-sestamibi radiopharmaceutical. *J. Mol. Struct.* **2021**, *1246*, 131159. [CrossRef]
538. Duvall, W.L.; Case, J.; Lundbye, J.; Cerqueira, M. Efficiency of tetrofosmin versus sestamibi achieved through shorter injection-to-imaging times: A systematic review of literature. *J. Nucl. Cardiol.* **2021**, *28*, 1381–1394. [CrossRef]
539. Boschi, A.; Uccelli, L.; Marvelli, L.; Cittanti, C.; Giganti, M.; Martini, P. Technetium-99m Radiopharmaceuticals for Ideal Myocardial Perfusion Imaging: Lost and Found Opportunities. *Molecules* **2022**, *27*, 1188. [CrossRef]
540. Bolzati, C.; Dolmella, A. Nitrido Technetium-99m Core in Radiopharmaceutical Applications: Four Decades of Research. *Inorganics* **2020**, *8*, 3. [CrossRef]
541. Gao, S.; Zhao, G.; Wen, Q.; Bai, L.; Chen, B.; Ji, T.; Ji, B.; Ma, Q. Pharmacokinetics and Biodistribution of 99mTc N-MPO in Healthy Human Volunteers. *Clin. Nucl. Med.* **2014**, *39*, e14–e19. [CrossRef]
542. Salvarese, N.; Carta, D.; Mazano, C.; Gerardi, G.; Melendez-Alafort, L.; Bolzati, C. [^{99m}Tc][Tc(N)(DASD)(PNPn)]+ (DASD=1,4-Dioxa-8-azaspiro[4,5]decandithiocarbamate, PNPn=Bisphosphioamine) for Myocadial Imaging: Synthesis, Pharmacological and Pharmacokinetic Studies. *J. Med. Chem.* **2018**, *61*, 1114–11126. [CrossRef]
543. Johnson, L.L.; Seldin, D.W. Clinical experience with technetium-99m teboroxime, a neutral, lipophilic myocardial perfusion imaging agent. *Am. J. Cardiol.* **1990**, *66*, E63–E67. [CrossRef]
544. Beanlands, R.S.; DeKemp, R.A.; Harmsen, E.; Veinot, J.P.; Hartman, N.G.; Ruddy, T.D. Myocardial kinetics of technetium-99m teboroxime in the presence of post-ischemic injury, necrosis and low flow re-perfusion. *J. Am. Coll. Cardiol.* **1996**, *28*, 487–494. [CrossRef]
545. Okada, D.R.; Johnson, G.; Okada, R.D. Myocardial clearance of technetium-99m-teboroxime in re-perfused injured canine myocardium. *EJNMMI Res.* **2014**, *4*, 42. [CrossRef] [PubMed]
546. Liu, M.; Fang, W.; Liu, S. Novel ^{99m}Tc(III) Complexes [^{99m}TcCl9CDO)(CDOH)$_2$B-R] (CDOH$_2$= Cyclohexadinone Dioxime) Useful as Radiotracers for Heart Imaging. *Bioconjug. Chem.* **2016**, *27*, 2770–2779. [CrossRef]
547. Liu, M.; Liu, S. ^{99m}Tc-3Cboroxime: A novel ^{99m}Tc(III) complex [^{99m}TcCl(CDO)(CDOH$_2$)B-3C] (CDOH$_2$ = cyclohexanedione dioxime; 3C-B(OH)$_2$ = 3-(carbamoylphenyl)boronic acid) with high heart uptake and long myocardial retention. *Dalton Trans.* **2017**, *46*, 14509–14518. [CrossRef]
548. Zhao, Z.Q.; Liu, M.; Fang, W.; Liu, S. Sulfonyl-Containing Boronate Caps for Optimization of Biological Properties of ^{99m}Tc(III) Radiotracers [^{99m}TcCl(CDO)(CDOH$_2$)B-R] (CDOH$_2$ = Cyclohexanedione Dioxime). *J. Med. Chem.* **2018**, *68*, 319–328. [CrossRef] [PubMed]
549. Xi, X.Y.; Wang, L.; Hsu, B.; Zhao, Z.-Q.; Liu, S.; Fang, W. ^{99m}Tc-3SPboroxime: A neutral ^{99m}Tc(III) radiotracer with high heart uptake and long myocardial retention. *J. Nucl. Cardiol.* **2021**, *28*, 2687–2696. [CrossRef] [PubMed]
550. Adak, S.; Bhalla, R.; Vijaya Raj, K.K.; Mandal, S.; Pickett, R.; Luthra, S.K. Radiotracers for SPECT imaging: Current scenario and future prospects. *Radiochim. Acta* **2012**, *100*, 95–107. [CrossRef]

MIM Software Inc. v. Progenics Pharmaceuticals, Inc.
IPR2025-00630
Progenics EX2017

551. Valotassiou, V.; Malamitsi, J.; Papatrintafyllou, J.; Dardiotis, E.; Tsougos, I.; Psimadas, D.; Alexiou, S.; Hadjigeorgiou, G.; Georgoulias, P. SPECT and PET imaging in Alzheimer's disease. *Ann. Nucl. Med.* **2018**, *32*, 583–593. [CrossRef]
552. Chen, C.-J.; Bando, K.; Ashino, H.; Taguchi, K.; Shiraishi, H.; Shima, K.; Fujimoto, O.; Kitamura, C.; Matsushima, S.; Uchida, K.; et al. In Vivo SPECT Imaging of Amyloid-β Deposition with Radioiodinated Imidazo[1,2-*a*]Pyridine Derivative DRM106 in a Mouse Model of Alzheimer's Disease. *J. Nucl. Med.* **2015**, *56*, 120–126. [CrossRef]
553. Maya, Y.; Okumura, Y.; Kobayashi, R.; Onishi, T.; Shoyama, Y.; Barret, O.; Alagille, D.; Jennings, D.; Marek, K.; Seibyl, O.; et al. Preclinical properties and human in vivo assessment of $_{123}$I-ABC577 as a novel SPECT agent for imaging amyloid-β. *Brain* **2016**, *139*, 193–203. [CrossRef] [PubMed]
554. Fletcher, S.P.; Noor, A.; Hickey, J.L.; McLean, C.A.; White, J.M.; Donnelly, P.S. Rhenium and technetium complexes of thioamide derivatives of pyridylhydrazine that bind to amyloid-β plaques. *J. Biol. Inorg. Chem.* **2018**, *23*, 1139–1151. [CrossRef] [PubMed]
555. Sagnou, M.; Mavroidi, B.; Shegani, A.; Paravatou-Petsotas, M.; Raptopoulou, C.; Psycharis, V.; Pirmettis, I.; Papadopoulos, M.S.; Pelecanou, M. Remarkable Brain Penetration of Cyclopentadienyl $M(CO)_3^+$ (M = ^{99m}Tc, Re) Derivatives of Benzothiazole and Benzimidazole Paves the Way for Their Application as Diagnostic, with Single-Photon-Emission Computed Tomography (SPECT), and Therapeutic Agents for Alzheimer's Disease. *J. Med. Chem.* **2019**, *62*, 2638–2650. [CrossRef] [PubMed]

MIM Software Inc. v. Progenics Pharmaceuticals, Inc.
IPR2025-00630
Progenics EX2017